

**THÈSE DE DOCTORAT
DE SORBONNE UNIVERSITÉ**

Spécialité : Physique

École doctorale n°564: Physique en Île-de-France

réalisée sous la direction de Alberto BRAMATI

au Laboratoire Kastler Brossel



présentée par

Kevin FALQUE

Sujet de la thèse :

Full optical control of quantum fluids of light in hot atomic vapors

soutenue le 2 octobre 2023

devant le jury composé de :

| | | | |
|-------------------------------------|-------------|----------------------------|--------------------|
| M. LEYRONAS Xavier, | Professeur, | SU / ENS Paris, | Examinateur |
| M. DAVID Clément, | MCF, | Institut d'Optique, | Examinateur |
| M ^{me} BOUCHOULE Isabelle, | DR, | Institut d'Optique, | Rapporteur |
| M. DUDLEY John, | PR, | Univ. de Franche-Comté, | Examinateur |
| M. GLORIEUX Quentin, | MCF, | SU, | Directeur de thèse |
| M. ALBERT Mathias, | MCF, | Univ. de Nice Côte d'Azur, | Rapporteur |
| M. BABOUX Florent, | MCF, | Univ. de Paris Cité, | Invité |

Contents

| | |
|-------------------------------------------------------------------------------|------------|
| Contents | iii |
| Remerciements | v |
| I Theory of Microcavity Exciton Polaritons | 1 |
| 1 Microcavity Exciton Polaritons | 3 |
| 1.1 Microcavity Photons | 4 |
| 1.2 Excitons in Semiconductors | 7 |
| 1.2.1 Band theory in brief | 7 |
| 1.2.2 Band structure of semiconductors | 8 |
| 1.2.3 Exciton phenomenological approach | 8 |
| 1.2.4 Electron-hole interactions and exciton formation | 10 |
| 1.2.5 Exciton-photon interaction in bulk semiconductor: | 17 |
| 1.2.6 Exciton in 2D quantum well | 18 |
| 1.2.7 Exciton-exciton interaction | 21 |
| 1.3 Excitons-polaritons | 23 |
| 1.3.1 Polariton interactions | 29 |
| 1.4 Polariton dynamics | 31 |
| 1.4.1 Mean field approximation | 32 |
| 1.4.2 Driven dissipative Gross-Pitaevskii Equation. | 33 |
| 1.4.3 Excitation scheme | 35 |
| 2 Optical generation and spectroscopy of arbitrary acoustic horizons | 43 |
| 2.1 Optical generation of arbitrary fluid velocity field | 44 |
| 2.1.1 Waterfall configuration | 44 |
| 2.1.2 Target velocity profile | 44 |
| 2.1.3 Effective 1D fluid | 46 |
| 2.2 Experimental spectroscopy of the collective excitation spectrum | 48 |
| 2.2.1 High resolution pump-probe spectroscopy method | 49 |
| 2.3 Experimental setup | 50 |
| 2.4 Experimental results | 51 |
| 2.4.1 Homogeneous fluid | 51 |
| 2.4.2 Smooth transition geometry | 56 |
| 2.4.3 Steep horizon geometry | 61 |

| | | |
|---------------------|-------------------------------------------|-----------|
| 2.4.4 | Quasi-normal mode configuration | 64 |
| 2.5 | Conclusion | 65 |
| 2.5.1 | Outlook | 65 |
| | | |
| Appendices | | 67 |
| | | |
| A | Mean field shaping and monitoring | 69 |
| A.1 | Phase printing | 69 |
| A.1.1 | Spatial light modulator. | 69 |
| A.1.2 | Phase measurement | 70 |
| A.1.3 | Off axis interferometry | 70 |
| A.1.4 | Controlling the local intensity | 70 |
| | | |
| Bibliography | | 73 |

Remerciements

Merci à tous

Part I

Theory of Microcavity Exciton Polaritons

Chapter 1

Microcavity Exciton Polaritons

Photons are massless particles, yet when confined within an optical cavity, they obtain an effective mass and exhibit a parabolic dispersion relation. However, two photons in the cavity do not interact with each other in the sense that they do not attract or repel each other as massive particles would do.

Whenever an electromagnetic field is shined on a material, the dipoles of the medium oscillate and change the refractive index seen by the field. At high intensity, the change in the refractive index can depend on the square of the electric field, which is then called the Kerr effect. Since a local variation of the refractive index deflects light, a high-intensity region in the material can modify the trajectory of an incoming beam. From this point of view, one can see how photon-photon interaction can arise in a nonlinear medium.

If the medium is chosen such that the resonance frequency of the dipoles matches the resonance of the optical microcavity, the light can be trapped in the sample and experience effective interaction through the medium. When the coupling of the light with the medium is strong enough to exceed the losses of the whole system, one can achieve the strong coupling regime. In this regime, the new eigenstates of the system are the so-called polaritons, which are a superposition of the photon and the dipole excitation of the medium. This hybrid state of matter inherits properties from both photons and matter excitations and forms the constitutive particles of the quantum fluid considered later.

In the present case, the strong coupling regime is achieved in a semiconductor microcavity by inserting two-dimensional quantum wells at the antinode of the electromagnetic field of a high-quality factor optical microcavity. In such devices, polaritons arise from the coupling between the cavity photons and the excitons of the quantum wells.

This chapter is dedicated to describing photons and excitons separately before showing how they couple in the sample to form polaritons. Then, from a microscopic description, one will derive the macroscopic equations of motion of the fluid and find that polaritons can be described in the usual Quantum Fluid framework with a driven dissipative Gross-Pitaevskii equation.

1.1 Microcavity Photons

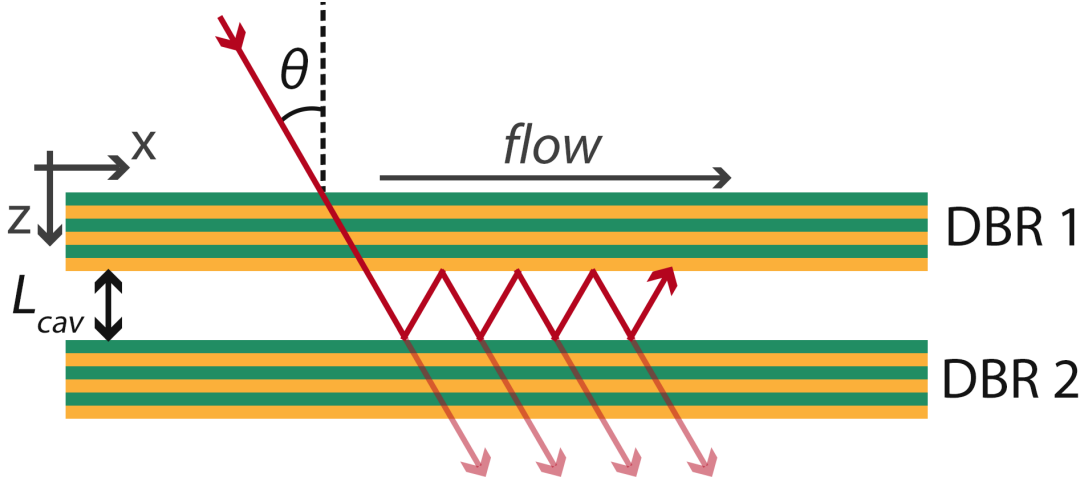


Fig. 1.1 Photon in a planar microcavity

Planar microcavity parameters: First, let us consider an electromagnetic field incident at an angle θ on a planar microcavity made with two mirrors with reflectivities R_1 and R_2 , separated by a distance L . The z-axis is normal to the mirrors as shown in Figure 1.1. The phase shift acquired during a single round trip in the cavity is $\Delta\phi(\theta) = 2nk_0L \cos(\theta)$, with n the refractive index of the medium and $k_0 = 2\pi/\lambda$ the wave vector of the field in vacuum. The interference between the multiple reflections sets the resonance condition of the cavity, and the transmission of the field can be written as:

$$T(\theta) = \frac{R_1 R_2}{1 + R_1 R_2 - \sqrt{R_1 R_2} \cos(\Delta\phi(\theta)/2)} \quad (1.1)$$

From this, one can define the decay rate of the field oscillation known as the quality factor:

$$Q = \frac{\omega_\gamma}{\Delta\omega_\gamma} \quad (1.2)$$

with ω_γ the resonance frequency of the cavity and $\Delta\omega_\gamma$ the linewidth of the resonance, which sets the lifetime of the photon in the cavity through $\tau_\gamma = 1/\Delta\omega_\gamma$ and depends on the mirrors' reflectivities. Another important parameter describing the cavity is its frequency resolution, which is encoded in the cavity finesse through:

$$\mathcal{F} = \pi \frac{\Delta\omega_\gamma}{\delta\omega_\gamma} = \pi \frac{\sqrt{R_1 R_2}}{1 - R_1 R_2} \quad (1.3)$$

where $\Delta\omega_\gamma$ is the Free Spectral Range (FSR) representing the frequency difference between two successive longitudinal modes of the cavity. To achieve strong coupling with the nonlinear medium, the photon needs to stay trapped in the cavity long enough to interact with the

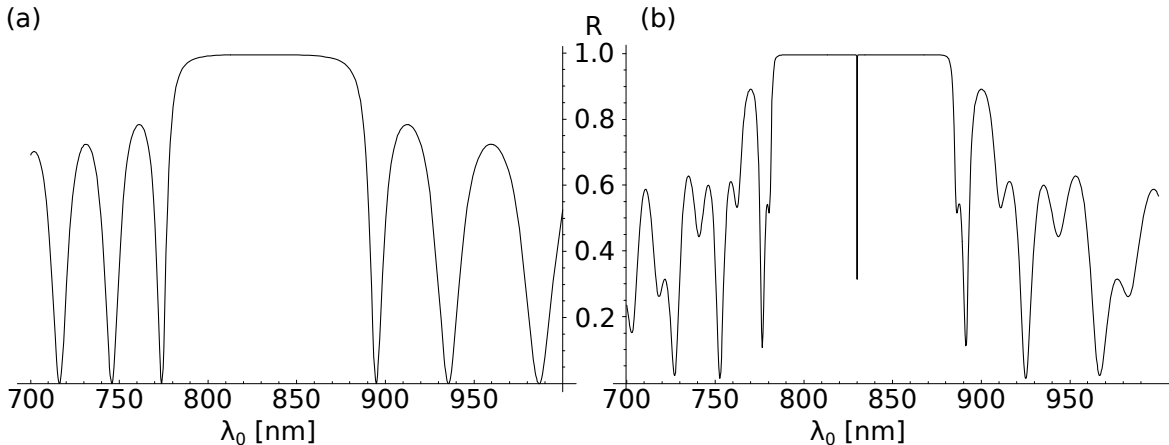


Fig. 1.2 **DBR and Fabry-Perot cavity reflectivity.** (a) Reflectivity R of a Bragg mirror of 20 pairs of $\text{Ga}_{0.9}\text{Al}_{0.1}\text{As}/\text{AlAs}$, illuminated at normal incidence for different wavelengths λ . The DBR has a reflectivity close to 1 over a large range of wavelengths called the stop-band, centered on $\lambda_0 = 836$ nm by tuning the thickness of each of the mirror layers. (b) Corresponding reflectivity of the optical cavity built from the facing of two DBR mirrors identical to that in (a) and separated by a distance $L_{\text{cav}} = 2\lambda_0/n_{\text{cav}}$, leading to the appearance of a very narrow resonance at λ_0 . Adapted from ??.

medium. In other words, the quality factor of the cavity must be very high, which means using mirrors with high reflectivities. This can be achieved with Distributed Bragg Reflectors (DBR) mirrors.

Distributed Bragg Reflectors. These reflectors consist of a series of N alternating layers composed of two materials with different refractive indices $n_1 < n_2$. This configuration causes partial reflection of the electromagnetic field at each of the N interfaces, resulting in a very high overall reflection coefficient, R , which is expressed as follows:

$$R = \left[\frac{(n_2/n_1)^{2N} - n_f/n_0}{(n_2/n_1)^{2N} + n_f/n_0} \right]^2, \quad (1.4)$$

with n_0 and n_f representing the refractive indices of the media before and after the mirrors. Figure 1.2 illustrates the evolution of R in relation to the wavelength of the electromagnetic field for one DBR mirror used in our system. This mirror is constructed with 20 pairs of $\text{Ga}_{0.9}\text{Al}_{0.1}\text{As}/\text{AlAs}$ layers, having refractive indices $n_2 = 3.48$ and $n_1 = 2.95$ respectively. The reflection coefficient R is 0.9985 across a broad wavelength range, known as the stop-band, centered around a wavelength of $\lambda_0 = 836$ nm. This central wavelength is achieved by setting the thickness of the layers to $d_{1,2} = \lambda_0/4n_{1,2}$. The microcavity used in the experiments is built by facing two of those DBR mirrors separated by a distance $L_{\text{cav}} = 3\lambda_0/2n_{\text{cav}}$, giving rise to a very narrow resonance at λ_0 with three field antinodes within the cavity. The parameters of the cavity are summarized in Equation 1.1.

| Fabry-Perot cavity parameters | | | | | |
|-------------------------------|--------|-------|-------|------------------|------------------|
| R_1 | R_2 | n_1 | n_2 | n_{cav} | λ_0 (nm) |
| 0.9992 | 0.9985 | 2.95 | 3.48 | 3.54 | 836 |
| | | | | | |

With the above-described DBR, the cavity has a finesse $\mathcal{F} = 2850$ from which we can infer the photon lifetime:

$$\delta\omega_\gamma = \frac{\Delta\omega_\gamma}{\mathcal{F}} = \frac{c}{n_{\text{cav}}L_{\text{eff}}} \frac{1-R}{\sqrt{R}}, \quad (1.5)$$

where $L_{\text{eff}} = L_{\text{cav}} + L_{\text{bragg}}$ is the effective length of the sample taking into account the penetration of the field in the mirrors.

$$L_{\text{Bragg}} = \frac{\lambda_0}{2} \frac{n_1 n_2}{n_{\text{cav}}(n_2 - n_1)} \quad (1.6)$$

which gives $\tau_\gamma = \frac{1}{\delta\omega_\gamma} = 5$ ps.

Transverse dynamics of the photon. The energy of the photon within the sample can be written as:

$$E_\gamma = \frac{\hbar c}{n_{\text{cav}}} \sqrt{k_x^2 + k_y^2 + k_z^2}. \quad (1.7)$$

The resonance condition of the cavity fixes the photon wavevector along the z component.

$$k_z = \frac{2\pi n_{\text{cav}}}{\lambda_0}. \quad (1.8)$$

In the paraxial approximation $k_x, k_y \ll k_z$, one can expand (1.7) in terms of $\frac{\|\mathbf{k}_\parallel\|}{\|\mathbf{k}_z\|}$ as:

$$E_\gamma = \frac{\hbar c}{n_{\text{cav}}} \sqrt{k_z^2 + k_\parallel^2} = E_0 \left(1 + (\hbar k_\parallel)^2 \frac{c^2}{2(n_{\text{cav}} E_0)^2} \right). \quad (1.9)$$

where $\mathbf{k}_\parallel = \mathbf{k}_x + \mathbf{k}_y$ is the wavevector in the transverse plane and $E_0 = hc/\lambda_0$ is the photon energy in free space. We can identify the effective mass of the photon by writing (1.9) with the usual form of the kinetic energy of a massive particle:

$$E_\gamma = E_0 + \frac{p_\parallel^2}{2m_\gamma} \quad (1.10)$$

where we identify $m_\gamma = \frac{\hbar n_{\text{cav}}^2}{\lambda_0 c}$ which is inversely proportional to the second derivative of the energy with respect to k_\parallel :

$$\frac{1}{m_\gamma} = \frac{1}{\hbar^2} \frac{\partial^2 E_\gamma}{\partial k_\parallel^2} \quad (1.11)$$

Momentum conservation: we mentioned the necessity to have a high quality factor to later achieve strong coupling. One could then ask why do we stick to planar designs, which are generally not the best solution to get a high Q factor since they are known to be unstable except for plane waves. The answer lies in the calculation just above. Indeed, the advantage of having a planar design is the translational invariance in the xy plane, which brings \mathbf{k}_{\parallel} conservation. As a consequence, if one shines a laser with a given \mathbf{k}_{\parallel} , light will behave in the cavity as a massive particle moving at velocity $v_{\gamma} = \hbar \mathbf{k}_{\parallel} / m_{\gamma}$. In the picture of creating a fluid whose flow is controlled, the planar design then appears as a wise choice.

A direct link between incidence angle and in plane momentum \mathbf{k}_{\parallel} : as shown in Figure 1.1 the incidence angle $\theta = (\theta_x, \theta_y)$ of the incoming field is related to the in-plane momentum k_{\parallel} as :

$$k_x = k_0 \sin(\theta_x) \quad (1.12)$$

$$k_y = k_0 \sin(\theta_y) \quad (1.13)$$

Controlling the in plane momentum of photons and latter of polaritons then boils down to control the local incidence angle of the field, in other words, the transverse phase of the incoming beam. This is a crucial point for the experiments as it allows to control the flow of the fluid by changing the laser phase.

Conclusion: This section revealed how trapping light in a planar microcavity grants it effective mass and lifetime. The next section will explore the semiconducting media that can be inserted into these cavities, especially the bound electron-hole pairs called excitons that can be addressed by the trapped light.

1.2 Excitons in Semiconductors

1.2.1 Band theory in brief

Applying the Schrodinger equation to an atom reveals that the electrons energies can only take discrete values. However, N atoms sufficiently close to each other interact which lift the degeneracy and turns each energy state in a set of N separated levels (see Figure 1.3). Within a solid material, the density is so high (typically 10^{22} atoms per cm^3) that the spacing between energy levels tends to zero forming a continuous band of energy. The electrons fill the band from the lowest energy level up to the Fermi energy. The Fermi energy is the energy of the highest occupied state at zero temperature. The band structure of a material is then defined by the energy of the valence band, the conduction band and the band gap between them. The valence band is the highest energy band that is fully occupied at zero temperature, while the conduction band is the lowest energy band that is empty at zero temperature. The band gap is the energy difference between the conduction band and the valence band. Determining if a material is a metal, a semiconductor or an insulator is then a matter of comparing the band gap to the Fermi energy. For metals the conduction band and the valence band overlap, any electric potential difference puts then the electron into motion and create a current. For insulators and semiconducting materials the Fermi energy is in the band gap. For insulators the band gap is typically ~ 3 eV making the promotion of

an electron to the conduction band highly energy demanding. Finally, the semiconductors gap energy is accessible with photons in the visible domain making these materials perfect candidates for controlled light-matter interactions.

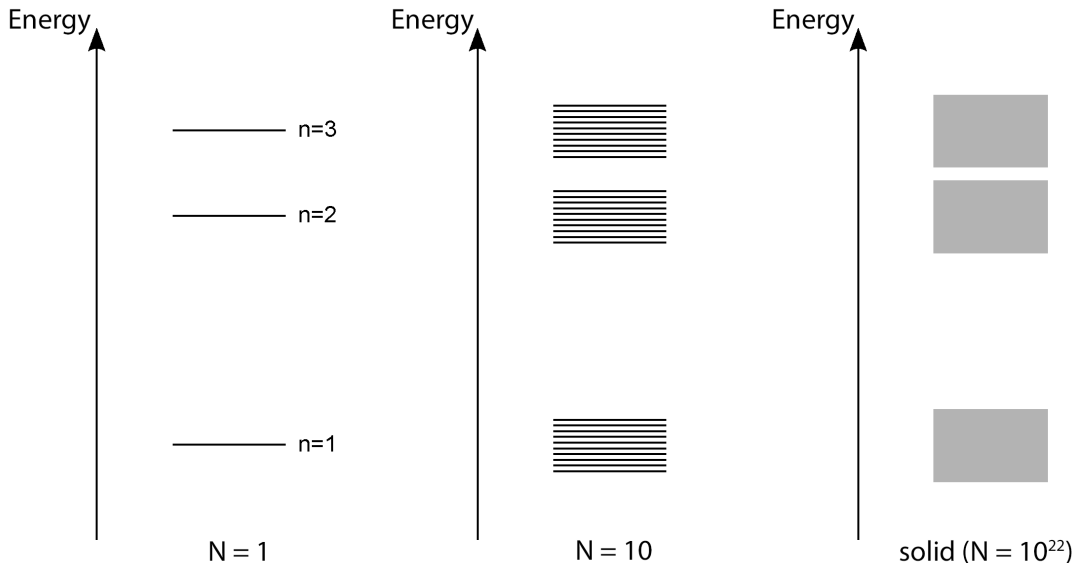


Fig. 1.3 **Energy levels of a set of N atoms.** As N increase the spacing between two successive levels tends to zero and eventually form a continuous band of energy.

1.2.2 Band structure of semiconductors

Finding the exact band structure of a material can be done by solving the Schrodinger equation for an electron in periodic potential. The Bloch theorem states that the wave function of such an electron can be written as a plane wave modulated by a periodic function. The periodic function is then expanded in a Fourier series and the Schrodinger equation is solved for each Fourier component. The exact band structure can be rather complicated but a simplified version can be obtained by considering the effective mass approximation [19]. In this picture, the dispersion relation of the electron in the material is typically represented in Figure 1.4. In this case the minimum of the conduction band and the maximum of the valence band are located at the same point in the Brillouin zone. The material is then said to have a direct band gap.

1.2.3 Exciton phenomenological approach

As shown in Figure 1.4 shining a photon whose energy exceed the gap energy can promote an electron from the valence band to the conduction band through the absorption of a photon. The disappearance of the electron in the valence band can be described equivalently as the creation of a virtual particle of opposite charge called hole [9]. If one scan shine a laser on a semiconductor and ramp up its frequency a narrow absorption peak is observed below the gap energy. The presence of this peak originate from the coulombic interaction between the

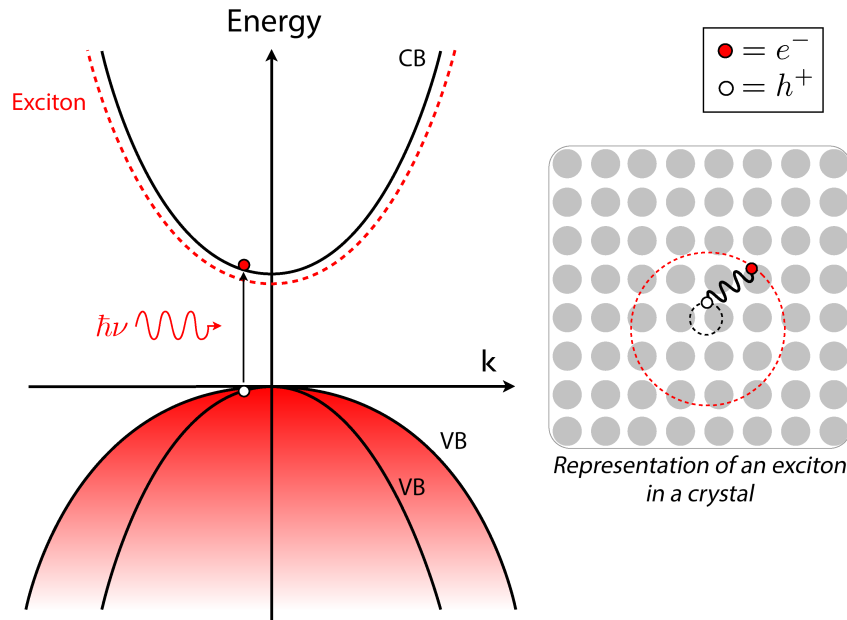


Fig. 1.4 **Band structure of a direct gap semiconductor.** The black solid line represent the conduction and valence band in a bulk semiconductor. The red dashed lines represent the dispersion relation of an exciton. The filling of the valence band by electrons is represented by the shaded red color.

created electron and the hole creating a bound state of the material. In terms of energy it's as if the gap energy is reduced by the binding energy of the exciton and the electron lies in a virtual band below the conduction band as represented by the red dashed lines in Figure 1.4. The exciton energy can then be written as :

$$E_X = E_g - E_b + \frac{\hbar^2 K^2}{2m_X} \quad (1.14)$$

where E_g is the gap energy, E_b the binding energy, $\hbar\vec{K}$ is the exciton momentum defined as the electron-hole pair center of mass momentum and m_X the exciton effective mass which is the sum of the electron and hole effective mass. Since E_b is the interaction energy between a electron and a hole it is, as we will see in the next section, very similar to the Rydberg energy series of the hydrogen atom, the hole playing the role of the proton. As a consequence, the same electronic structure exist for the exciton : 1s, 2s, 2p, etc state can be observed in the absorption spectrum of the material. However, the hole is quite different from the proton in the sense that it's actually a collective excitation of all the valence band electrons. Furthermore the exciton is a weakly bound state as the binding energy is typically a few meV. In GaAs or AlGaAs heterostructures which are the materials used in the present work E_b is around 4 meV due to their high dielectric constant $\epsilon_r \sim 12$. In these kind of samples, excitonic resonances can only be observed at cryogenic temperatures since the binding needs to exceeds the thermal energy $k_B T$ in order to survive the thermal fluctuations. For the

above mentionned structures we obtain the condition $T < 10$ K for excitons stability. Another important exciton characteristic is their huge Bohr Radius $a_X = \frac{\epsilon_r \hbar^2}{m_X e^2} = 11.6$ nm in GaAs which is much larger then the typical size of a unit crystalline cell $a_0 = 5.651$ Å. This means that the exciton wavefunction is delocalized over many unit cells. Such excitons, are called Wannier-Mott and contrast with Frenkel excitons which are localized on a single unit cell and are typically found in organic materials.

1.2.4 Electron-hole interactions and exciton formation

Excitons were said to be made of an electron and a hole bound by Coulombic interactions. However, all the interactions in the material are ultimately mediated by valence and conduction band electrons. The rising of a bound state in such a material is therefore not obvious. In other words moving from a conduction-valence band electrons to a electron-hole picture is not trivial and reveals interesting feature about the electron-hole interactions that will at the end enable exciton formation. In this section we will first describe all the possible interactions between the electrons of the semiconductor before showing how they can be recasted in terms of electron-hole interactions.

1.2.4.1 Electron scattering in semiconductors

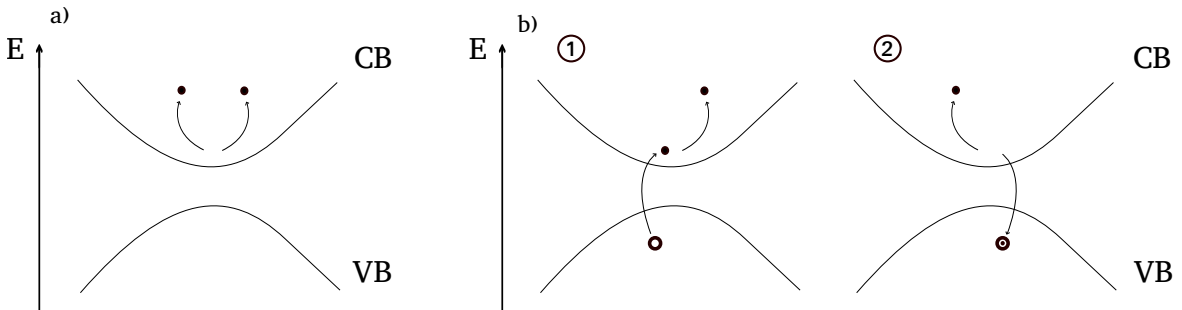


Fig. 1.5 **Drawing representing the scattering between two conduction band electrons.** a) Direct intraband scattering. Filled black dots represent conduction band electrons. b) Two steps scattering involving an electron-hole exchange or creation an annihilation of an exciton, referred as interband scattering. The empty black circle represent a valence band hole while the same circle with a small black dot inside stands for a valence band hole filled with an electron which is equivalent to a valence electron. a) and b) share the same final state which is a full valence band and two scattered conduction band electrons. Drawing inspired from [9].

Intraband scattering : to start with let's consider the direct scattering between two conduction band electrons as presented in Figure 1.5 a). This simple process is referred as intraband scattering since each electron stays in its own band. In the small momentum limit $\mathbf{q} \rightarrow 0$ it yields a potential of the form:

$$V_q \simeq \frac{4\pi e^2}{L^3 q^2} \quad (1.15)$$

in a sample of size L. This form of potential holds also for the scattering between two valence electrons or between a valence and a conduction band electron that stay in their respective bands.

Interband scattering : processes in which one or two electrons change band are also possible and are referred as interband scattering. In the case of a single interband jump the potential reads $(\frac{q}{\kappa})V_q = \frac{4\pi e^2}{L^3 q \kappa}$ where κ is a dimensionnal factor that depends on the material. It then behaves as $1/q$. When both electrons change band the potential is then $(\frac{q}{\kappa})^2 V_q$ proportionnal to q^0 and thus remaining finite when $q \rightarrow 0$. Remarkably, in both the single and two interband jump scenarios, the number of electrons in each band changes by one and two, respectively, making these transitions less likely to occur compared to number-conserving processes.

Indeed, in second order perturbation theory the transition amplitude between an initial state $|i\rangle$ and a final state $|f\rangle$ may be written as :

$$\Gamma_{i \rightarrow f}^{(2)} = \frac{2\pi}{\hbar} \left| \sum_m \frac{\langle f | V_q | m \rangle \langle m | V_q | i \rangle}{E_f - E_i} \right|^2 \delta(E_f - E_i) \quad (1.16)$$

Whenever an electron undergo a band jump the energy cost is of the order of the band gap $E_f - E_i \simeq E_g$. As a consequence the corresponding transition amplitude gets reduced by a factor $\frac{1}{E_g}$ and appears to be negligible. However a direct intraband scattering can happen in several interband jumps that will dress the direct Coulomb scattering as shown in [Figure 1.5 b\)](#) for the case of two jumps. When summing over all possible intermediate state as is [\(1.16\)](#) we end up with the same potential as the direct intraband scattering but reduced by dielectric constant factor ϵ_{sc} that depend on the material.

To clarify this idea let us now consider the scattering between a conduction and a valence band electron. The same scattering process can also occur in two steps. First, a conduction band electron is scattered in its band while a valence band electron is promoted to the conduction band. Since an electron changes band it brings a potential $V_q(q/\kappa)$. Secondly, the excited electron goes back to the valence band while a valence band electron is scattered in its band yielding again a potential $V_q(q/\kappa)$. This two steps interaction end up with the same initial and final states than direct intraband scattering and the number of electrons in each band is conserved. In terms of energy, the two scatterings behaving as $1/q$ potentials the overall potential behaves also as $1/q^2$ but with an additionnal $1/E_g$ factor coming from the intermediate interband jumps. More specifically the two steps contribution is : $(4\pi e^2/L^3 q^2) [(e^2/L^3 \kappa^2)/E_g]$.

It is also possible to make it a three steps scattering by adding an intermediate interband exchange after the first step : the previously excited conduction band electron returns to the valence band while a valence band electron is promoted to the conduction band. More explicitly the process is as follows :

- **Step 1 :** a valence band electron is promoted to the conduction band while a conduction band is scattered in its band. The potential reads $V_q(q/\kappa) \propto \frac{1}{q}$ and the energy cost is of the order of E_g .
- **Step 2 :** the previously excited conduction band electron returns to the valence band while another valence band electron is excited to the conduction band. The potential read $V_q(q/\kappa)^2 \propto q$ and the energy cost is of the order of $2E_g$.
- **Step 3 :** the excited electron goes back to the valence band while a valence band electron is scattered in its band. The potential read again $V_q(q/\kappa) \propto \frac{1}{q}$ and the energy cost is of the order of E_g .

The total energy budget is then : $(4\pi e^2/L^3 q^2) [(e^2/L^3 \kappa^2)/E_g]^2$. Remarkably, one might expect the overall potential to scale as $1/E_g^3$ since each step requires at least one electron to change band. However, the structure of perturbation theory ensures that the total energy denominator accounts for the number of coupled interband transitions, rather than treating each step independently. Step 2 effectively "couples" the transitions in such a way that two energy denominators are introduced, rather than three independent ones, which explains the $1/E_g^2$ dependence. This coupling reflects the fact that intermediate states are shared between adjacent steps in the perturbative sequence.

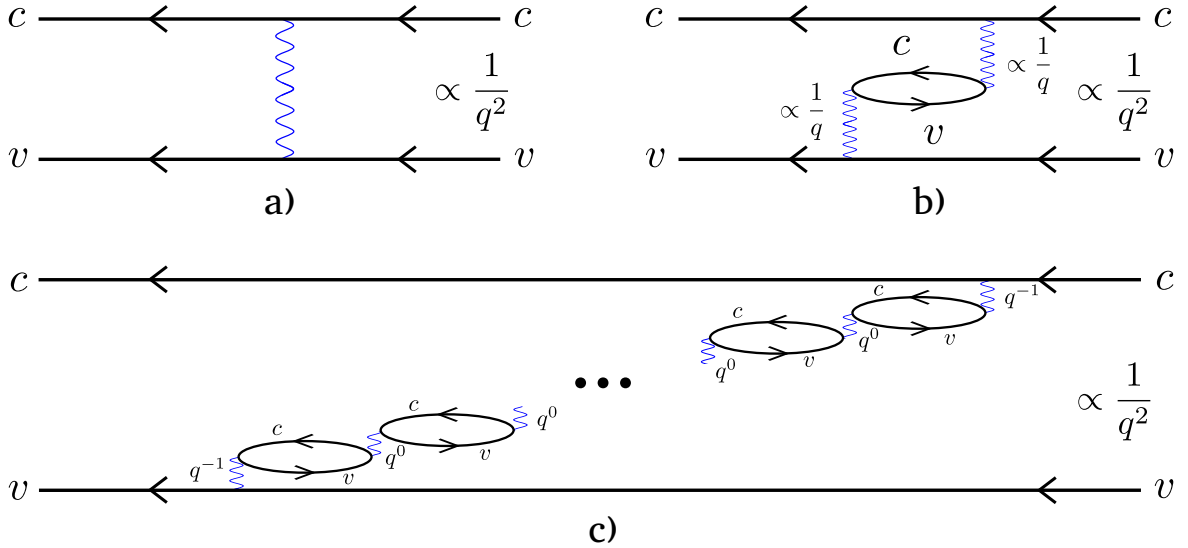


Fig. 1.6 **Feynman diagrams representing an intraband scattering between a conduction and a valence band electron.** a) Direct intraband scattering. The blue wavy lines represent the Coulomb interaction that make the electrons to change states. b) Two steps scattering involving an intermediate interband exchange that is represented by the bubble in the middle. c) Multiple steps scattering involving several interband exchanges represented by the numerous bubbles. Drawing inspired from [9].

Finally, the number of intermediate states can be arbitrarily increased by adding 'bubbles' of exchange interaction, as illustrated in the Feynman diagram in Figure 1.6 b). Each pair of

adjacent bubbles represents an interband interaction similar to the one described in Step 2 above. While it conserves the number of electrons in each band, it involves two interband jumps. The interaction between two bubbles is then $\propto q^0$ and is finite in the small momentum limit. By summing the contributions of processes with all possible numbers of bubbles, we obtain an effective Coulomb potential:

$$V_q = \frac{4\pi e^2}{L^3 q^2 \epsilon_{sc}} \quad (1.17)$$

where ϵ_{sc} is a dielectric constant stemming from the infinite sum over the number of bubbles. The discussion that we just made also holds for the intraband scattering between two conduction band electrons or two valence band electrons. Indeed, it graphically boils down to change the letter of the bands in the Feynman diagrams of [Figure 1.6](#) which doesn't change the overall energy budget of the process. Consequently, the potential (1.17) is valid for all intraband scattering processes. Based on the previous discussion we restrict the Coulomb potential that describe any scattering process to interactions that conserve the number of particle in each band, namely the intraband scattering potential between conduction and valence band electrons derived above. The general form of the potential is then in second quantization :

$$V_{coul} \simeq \frac{1}{2} \sum_{\mathbf{q} \neq 0} \frac{4\pi e^2}{L^3 q^2 \epsilon_{sc}} \sum_{\mathbf{k}_1, \mathbf{k}_2} \sum_{i_1, i_2} a_{i_1, \mathbf{k}_1 + \mathbf{q}}^\dagger a_{i_2, \mathbf{k}_2 - \mathbf{q}}^\dagger a_{i_2, \mathbf{k}_2} a_{i_1, \mathbf{k}_1} \quad (1.18)$$

where $i_1, i_2 \in (c, v)$. The creation operators $a_{c, \mathbf{k}}^\dagger$ and $a_{v, \mathbf{k}}^\dagger$ create respectively a conduction and a valence band electron with momentum \mathbf{k} . The $\mathbf{q} = 0$ contribution is not included and treated separately by the wise choice of an average electron-electron potential V_{e-e} that cancels it. More details can be found in the Appendix of [9]. It is worth noting that, in the conduction-valence electron framework, all intraband interactions are identical and repulsive. From this it is not obvious how a bound state like an exciton can arise in the material. However, as we will see in the next section, transitioning to the electron-hole description transforms one of these scattering interactions into an attractive interaction. This feature is central to the energy splitting between two types of excitons: bright excitons, which couple to light, and dark excitons, which do not.

1.2.4.2 From the conduction-valence electrons to electron-hole picture

So far we described the scattering process within the semiconductor using valence and conduction electrons. However, the exciton results from the binding between a conduction band electron and the absence of a valence band electron that we usually describe as a hole. While the conduction electron description stays the same, moving from one picture to the other require to define the hole creation operator that account for the removal of a valence band electron or equivalently the creation of a hole in the valence band.

$$a_{c, \mathbf{k}}^\dagger = a_{\mathbf{k}}, \quad (1.19a)$$

$$a_{v, \mathbf{k}}^\dagger = h_{-\mathbf{k}}^\dagger, \quad (1.19b)$$

where $h_{-\mathbf{k}}^\dagger$ creates a hole in the valence band with momentum $-\mathbf{k}$. The - sign is imposed by energy and momentum conservation laws. When we substitute the full valence band with a missing electron with momentum \mathbf{k}_v by a hole, the hole needs to have opposite charge $+|e|$, momentum $\mathbf{k}_h = -\mathbf{k}_v$ and energy $E_h(\mathbf{k}) = -E_v(\mathbf{k})$ to account for the "absence" of the valence electron. In the small momentum limit we have $E_v(\mathbf{k}) = E_{v0} + \frac{\hbar^2 k_v^2}{2m_v}$ with m_v the valence electron effective mass that is negative as visible in [Figure 1.4](#). The constraint on the energy $E_h = -E_v$ then imposes $\frac{\hbar^2 k_h^2}{2m_h} = -\frac{\hbar^2 k_v^2}{2m_v}$ making the effective mass of the hole positive. Its charge and mass being positive it can then undergo attractive interactions with a conduction band electron and eventually form an exciton. We already see how describing the valence band with hole instead of electrons can predict the formation of bound state. Let us now look how this feature arise from a microscopic point of view. The full crystal hamiltonian is :

$$\mathcal{H} = \mathcal{H}_0 + V_{coul} \quad (1.20)$$

with \mathcal{H}_0 the free electron hamiltonian and V_{coul} the Coulomb interaction between electrons. The free electron hamiltonian reads :

$$\mathcal{H}_0 = \sum_{\mathbf{k}} E_c(\mathbf{k}) a_{c,\mathbf{k}}^\dagger a_{c,\mathbf{k}} + \sum_{\mathbf{k}} E_v(\mathbf{k}) a_{v,\mathbf{k}}^\dagger a_{v,\mathbf{k}} \quad (1.21)$$

where $E_c(\mathbf{k})$ and $E_v(\mathbf{k})$ are the conduction and valence band energies respectively. The Coulomb interactions part can be decomposed in the following way :

$$V_{coul} = V_{cc} + V_{vv} + V_{cv} \quad (1.22)$$

Using the newly defined operators together with fermionic commutation relation $a_{i,\mathbf{k}}^\dagger a_{i,\mathbf{k}} = 1 - a_{i,\mathbf{k}} a_{i,\mathbf{k}}^\dagger$ the different scattering potentials are modified as we now show.

- The one body hamiltonian reads :

$$\mathcal{H}_0 = \sum_{\mathbf{k}} E_v(\mathbf{k}) + \sum_{\mathbf{k}} E_c(\mathbf{k}) a_{\mathbf{k}}^\dagger a_{\mathbf{k}} + \sum_{\mathbf{k}} -E_v(\mathbf{k}) h_{\mathbf{k}}^\dagger h_{\mathbf{k}}. \quad (1.23)$$

- The scattering between two conduction band electron is the same as before :

$$V_{cc} = \frac{1}{2} \sum_{\mathbf{q} \neq 0} V_{\mathbf{q}} \sum_{\mathbf{k}_1, \mathbf{k}_2} a_{\mathbf{k}_1 + \mathbf{q}}^\dagger a_{\mathbf{k}_2 - \mathbf{q}}^\dagger a_{\mathbf{k}_2} a_{\mathbf{k}_1} \equiv V_{ee} \quad (1.24)$$

- The scattering between two valence band electrons splits into three terms :

$$V_{vv} = -\frac{N_v}{2} \sum_{\mathbf{k} \neq 0} V_{\mathbf{k}} + \sum_{\mathbf{k}} h_{\mathbf{k}}^\dagger h_{\mathbf{k}} \sum_{\mathbf{k}' \neq \mathbf{k}} V_{\mathbf{k}' - \mathbf{k}} + V_{hh}. \quad (1.25)$$

The first term is constant and account for repulsive exchange interaction between all valence electrons. The second term comes from the scattering between a valence electron

with wavevector \mathbf{k} and all the other valence electrons. It adds a shift to the hole kinetic energy $E_h = -E_v$ that appears in the one body hamiltonian \mathcal{H}_0 . The last term is the hole-hole interaction that is repulsive and is the same as the valence electron-electron interaction with opposite wavevectors :

$$V_{hh} = \frac{1}{2} \sum_{\mathbf{q} \neq 0} V_{\mathbf{q}} \sum_{\mathbf{k}_1, \mathbf{k}_2} h_{\mathbf{k}_1 + \mathbf{q}}^\dagger h_{\mathbf{k}_2 - \mathbf{q}}^\dagger h_{\mathbf{k}_2} h_{\mathbf{k}_1} \quad (1.26)$$

- Finally, scattering between a conduction and a valence band electron is :

$$V_{cv} = \sum_{\mathbf{q} \neq 0} V_{\mathbf{q}} \sum_{\mathbf{k}_1, \mathbf{k}_2} a_{c, \mathbf{k}_1 + \mathbf{q}}^\dagger a_{v, \mathbf{k}_2 - \mathbf{q}}^\dagger a_{v, \mathbf{k}_2} a_{c, \mathbf{k}_1}. \quad (1.27)$$

Using that for non zero momentum transfer $[a_{v, \mathbf{k}_2 - \mathbf{q}}^\dagger, a_{v, \mathbf{k}_2}] = 0$ and introducing $\mathbf{k}'_2 = -(\mathbf{k}_2 - \mathbf{q})$ the potentials in terms of electron-hole reads :

$$V_{cv} = - \sum_{\mathbf{q} \neq 0} V_{\mathbf{q}} \sum_{\mathbf{k}_1, \mathbf{k}'_2} a_{\mathbf{k}_1 + \mathbf{q}}^\dagger h_{\mathbf{k}'_2 - \mathbf{q}}^\dagger h_{\mathbf{k}'_2} a_{\mathbf{k}_1} \equiv V_{eh}. \quad (1.28)$$

The latter require a special attention since it exhibits an attractive interaction and reveals the possibility of excitons formation which was not obvious in the conduction-valence electron picture.

Spin conservation in electron scattering

Scatterings processes mediated by the Coulomb interactions conserve the spin of the electron for both interband and intraband scatterings. As a consequence, the interactions between electrons and holes that we just exhibited are also spin preserving. The latter has important consequences to determine selection rules when looking at optical excitation of an electron-hole pair.

So far we demonstrated that replacing the full valence band by a hole looks quite convenient since it allow to forget about all the valence band electrons and exhibits the possibility of bound state formation. However, it must be done with caution since the remaining valence band electrons undergo the many intraband scattering processes described in the section and reduce the effective Coulombic intraband interaction by a factor $1/\epsilon_{sc}$. Remarkably, the intraband scatterings between valence and conduction band electrons V_{cv} are at the origin of the attractive electron-hole interactions while valence-valence interactions are responsible for the shift in the hole kinetic energy as expressed by [Equation 1.25](#). Let us now explain how the aforementioned electron-hole attractive interactions can lead to exciton formation.

1.2.4.3 The electron-hole hamiltonian

If we restrict the previous description to a one pair subspace namely to the interactions between a single electron and a single hole, electron-electron and hole-hole interactions can be safely dropped since they require two holes or electrons. The one pair hamiltonian then reads :

$$\mathcal{H}_{eh} = \mathcal{H}_e + \mathcal{H}_h + V_{eh}, \quad (1.29)$$

$$= \sum_{\mathbf{k}} E_c(\mathbf{k}) a_{\mathbf{k}}^\dagger a_{\mathbf{k}} + \sum_{\mathbf{k}} E_h(\mathbf{k}) h_{\mathbf{k}}^\dagger h_{\mathbf{k}} - \sum_{\mathbf{q} \neq 0} V_{\mathbf{q}} \sum_{\mathbf{k}_1, \mathbf{k}_2} a_{\mathbf{k}_1 + \mathbf{q}}^\dagger h_{\mathbf{k}_2 - \mathbf{q}}^\dagger h_{\mathbf{k}_2} a_{\mathbf{k}_1}. \quad (1.30)$$

Wannier exciton are the solutions $|x\rangle$ of the eigenproblem :

$$(\mathcal{H}_e + \mathcal{H}_h + V_{eh}) |i\rangle = E_i |i\rangle \quad (1.31)$$

with eigenvalue E_i . At this level the hamiltonian is very general and describe two coupled harmonic oscillators. Without going into details, this problem can be solved by following the same procedure as in classical mechanics. The core of the derivation consists in decoupling the two oscillators by introducing new coordinates that are the center of mass and relative coordinates. Since Coulombic interaction conserve momentum, the total momentum of the electron-hole pair $k_e + k_h$ stays constant and is equal to the exciton center of mass momentum \mathbf{Q} . Namely, we define :

$$\mathbf{Q} = \mathbf{k}_e + \mathbf{k}_h, \quad (1.32a)$$

$$\mathbf{q} = \gamma_h \mathbf{k}_e - \gamma_e \mathbf{k}_h, \quad (1.32b)$$

where $\gamma_e = 1 - \gamma_h = m_e/(m_e + m_h)$ is the reduced mass ratio and \mathbf{q} is the relative motion momentum. We then define the creation operator that creates an exciton $|x\rangle$ in state (\mathbf{Q}_i, ν_i) in terms of electron and hole operators :

$$b_{\mathbf{Q}_i, \nu_i}^\dagger = \sum_{\mathbf{p}} f_{\mathbf{p}}^{\nu_i} a_{\gamma_e \mathbf{Q}_i + \mathbf{p}}^\dagger h_{-\mathbf{p} + \gamma_h \mathbf{Q}_i}^\dagger \quad (1.33)$$

where $f_{\mathbf{p}}^{\nu_i} = \langle \mathbf{p} | \nu_i \rangle$ is the relative motion wave function. Let us show that the states $|\nu_i\rangle$ are the eigensolutions of a Hydrogen like problem ν_i being then related to the first quantum number of an electron orbitals. Injecting $|x\rangle = b_{\mathbf{Q}_i, \nu_i}^\dagger |0\rangle$, $|0\rangle$ being the vacuum state in Equation 1.31 we obtain \mathcal{H}_{eh} in a diagonal form :

$$\mathcal{H}_{eh} b_{\mathbf{Q}_i, \nu_i}^\dagger |0\rangle = \sum_{\mathbf{p}} \left\{ \left(E_g + \frac{\mathbf{Q}_i^2}{2m_X} + \frac{\mathbf{p}^2}{2\mu_X} \right) f_{\mathbf{p}}^{\nu_i} - \sum_{\mathbf{q} \neq 0} V_{\mathbf{q}} f_{\mathbf{p}-\mathbf{q}}^{\nu_i} \right\} a_{\mathbf{p} + \gamma_e \mathbf{Q}_i}^\dagger h_{-\mathbf{p} + \gamma_h \mathbf{Q}_i}^\dagger |0\rangle \quad (1.34)$$

whose eigenstates are $b_{\mathbf{Q}_i, \nu_i}^\dagger |0\rangle$ with energy $E_{X_i} = E_g + \frac{\mathbf{Q}_i^2}{2M_X} + E_b^i$ if and only if $f_{\mathbf{p}}^{\nu_i}$ are solution of the Hydrogen-like problem :

$$\frac{\mathbf{p}^2}{2\mu_X} f_{\mathbf{p}}^{\nu_i} - \sum_{\mathbf{q} \neq 0} V_{\mathbf{q}} f_{\mathbf{p}-\mathbf{q}}^{\nu_i} = E_b^i f_{\mathbf{p}}^{\nu_i} \quad (1.35)$$

where $\mu_X^{-1} = m_e^{-1} + m_h^{-1}$ is the relative motion mass and $m_X = m_e + m_h$ the total mass. The exciton then appears as a bound state of the electron-hole pair with a binding energy

E_b , whose center of mass is delocalized as a plane wave with momentum \mathbf{Q} . The binding energies E_b^i follows a Rydberg series $E_b^i = -\frac{R_X}{i^2}$ where R_X is the Rydberg constant of the exciton as defined in subsection 1.2.3. In the following section we will see how the excitons interact with light.

1.2.5 Exciton-photon interaction in bulk semiconductor:

The creation of an exciton can be mediated by the absorption of a photon by the material. On the other the annihilation of a exciton can lead to photon emission. As a start we describe this interaction with an usual electron-photon Hamiltonian in first quantization:

$$\mathcal{H}_{dip} = -e \frac{\mathbf{p}_e \cdot \mathbf{A}}{m_e}, \quad (1.36)$$

with \mathbf{p}_e the momentum operator of the electron and \mathbf{A} the potential vector of the electromagnetic field. Before going further let us have a look at what the symmetries of this Hamiltonian imply based on the Noether theorem.

- **Total momentum conservation :** translational invariance of the system implies that the total momentum of the system is conserved. The absorption of a photon with momentum $\hbar\vec{k}_c$ will create an exciton with the same momentum.
- **Total angular momentum conservation :** rotational invariance of the system implies that the total angular momentum of the system is conserved along the interaction.

The second point raises the question of the possible values that the exciton angular momentum can assume. To answer this question we need to get back to its microscopic constitutive particles : a conduction band electron and a hole in the valence band. In usual semiconductors a conduction band electron has an orbital angular momentum ($L = 0, L_z = 0$) while a valence band electron yields ($L = 1, L_z = (+1,0, -1)$) (see [19]). Since $J_z = J_z + S_z$ and the electron spin is $S_z = \pm 1/2$ we obtain for the valence band $J_z^v = (3/2, 1/2, -1/2, -3/2)$ and for the conduction band $J_z^c = \pm 1/2$. If we now move to the electron-hole picture the electron angular momentum remains unchanged $J_z^e = J_z^c = \pm 1/2$ while the hole angular momentum is the opposite of the valence band electron $J_z^h = -J_z^v = (3/2, 1/2, -1/2, -3/2)$. The exciton angular momentum is then $J_z = J_z^e + J_z^h = (-2, -1, 0, 1, 2)$. We can thus distinguish **bright** excitons with $J_z = (-1, 0, 1)$ that couple to light with polarization π, σ_+, σ_- and **dark** excitons with $J_z = (-2, 2)$ that do not couple to light. In the latter case the spin of the electron and the hole are aligned : $J_z = \pm 2$ excitons are made of $\pm 1/2$ electrons and $\pm 3/2$ holes. It means it corresponds to a situation in which the valence band electron flipped spin when it got promoted to the electron band. Yet, dark excitons can subsequently not undergo interband transitions that are spin preserving as mentionned in subsubsection 1.2.4.2. On the other hand, bright excitons result from interband transitions since both photon absorption and emission involve an electron changing band. In the framework of polariton which involve exciton creation through light one could think that since Coulomb inter and intraband scatterings are spin preserving, dark excitons are of no interest and won't play any role in the system. However, we will see that dark excitons can be created from bright excitons thanks to exchange carrier. that only bright excit

1.2.6 Exciton in 2D quantum well

Let us now get closer to the situation encountered in the sample used in the experiment. In such microcavities, excitons are confined in a planar quantum well which are made by stacking layers of semiconductor materials with different band gaps. The confinement in the plane is then ensured by the potential barrier between the layers. In our case a quantum well is made of InGaAs placed in between two layers of GaAs. InGaAs has a smaller band gap than the bulk GaAs because of the p-fraction of InAs doping as shown in Figure 1.7 (b). Both electrons and holes then remain confined in the region where the band gap is the smallest (see Figure 1.7 (a)). By repeating this "sandwiching" procedures it is possible to create many QW heterostructures as we shall see latter.

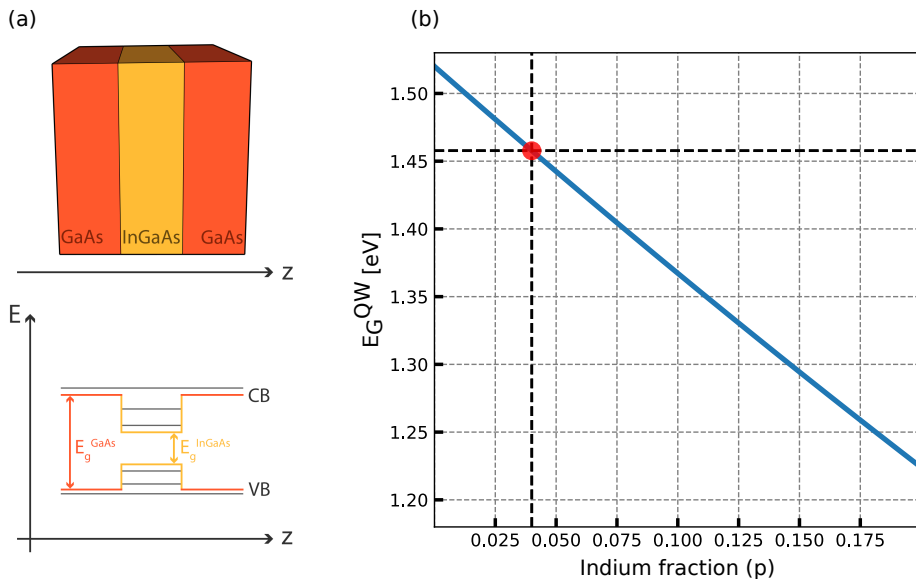


Fig. 1.7 **Schematic representation of a quantum well heterostructure.** a) Representation of a planar quantum well made of InGaAs placed in between two layers of GaAs. The confinement in the plane is ensured by the gap energy difference between the layers. b) Gap energy of the InGaAs quantum well as a function of the doping fraction of Indium. The red dot represent the doping in sample used in the experiment : $E_g^{InGaAs} = 1.46\text{eV} < E_g^{GaAs} = 1.52\text{eV}$.

Assuming the same geometry than the above figure the electron-hole hamiltonian taking into account the potential barrier is written in first quantization as :

$$\mathcal{H} = E_g^{QW} + \frac{\mathbf{p}_e^2}{2m_e} + \frac{\mathbf{p}_h^2}{2m_h} - \frac{e^2}{\epsilon_{sc}|r_e - r_h|} + V_e(z_e) + V_h(z_h) \quad (1.37)$$

where z is the growth axis of the quantum well and $V_e(z_e)$ and $V_h(z_h)$ are the potential barriers felt by the electron and the hole respectively, r_e and r_h are the electron and hole spatial coordinates. The system is invariant under translation in the xy -plane the excitons in plane wavevector k_{\parallel} can then take any value while the confinement in the z-direction quantize

the corresponding component of the wavevector k_z . This problem is treated by writting the exciton wavefunction $\Psi(x,y,z)$ as a two components product :

$$\Psi(x,y,z) = \psi(x,y,z)\phi(z). \quad (1.38)$$

The Schrodinger equation is then solved separately for $\psi(x,y)$ and $\phi(z)$. The confinement in z -direction is treated as a very basic quantum box problem. The electron and hole energies are then quantized as :

$$E_n^{e,h} = \frac{(\pi^2 n^2 \hbar^2)}{2m_{e,h} L_z^2} \quad (1.39)$$

where L_z is the width of the quantum well.

To determine the in-plane wavefunciton we follow the same procedure than for the exciton eigenproblem in the 3D case. The exciton is again a correlated pair whose center of mass is delocalized as a plane wave with momentum $\mathbf{Q} = \hbar\mathbf{k}_{||}$. The correspondig energy is then :

$$E_X^{xy} = E_g^{QW} + \frac{\hbar^2 k_{||}^2}{2m_X} - \frac{R_X^{QW}}{n^2} \quad (1.40)$$

provided that we defined a new Rydberg constant R_X^{QW} taking into account the confinement in the z -direction. Remarkably, due to confinement the Bohr radius a_X^{QW} of the QW exciton is twice smaller than the bulk exciton Bohr radius. This is a direct consequence of the confinement that increases the electron-hole wavefunctions overlap and thus the binding energy of the exciton. The exciton total energy is then :

$$E_X(\mathbf{k}_{||}) = E_g^{QW} + E_n^e + E_n^h + \frac{\hbar^2 k_{||}^2}{2m_X} - \frac{R_X^{QW}}{n^2} \quad (1.41)$$

The design of the sample used in the experimient is done such as the $n=1$ level is sufficiently far form the next level that we can restrict our description to the first 1s exciton state. In the following we will therefore drop the n index by setting it to one.

Bosonic nature of excitons. Since an exciton is made of two fermions its pseudo spin is an integer. However, when reaching regimes of high excitons densities the fermionic nature of their microscopic constitutives can no longer be neglected. The composite nature of excitons can then be safely dropped provided that the exciton density per unit area is such as $n_X(a_X^{QW})^2 \ll 1$. This condition state that the average distance between excitons is much larger than the exciton Bohr radius. In this regime the excitons can be treated as bosons, namely :

$$[b_{\mathbf{k}}, b_{\mathbf{k}}^\dagger] = 1 - O(n_X(a_X^{QW})^2) \simeq 1 \quad (1.42)$$

Optical selection rules in the planar quantum well. In bulk semiconductors, a single exciton mode couples exclusively to a single photon mode. In quasi-two-dimensional systems, due to

the breaking of translationnal invariance in the growth direction z the momentum conservation during a photon absorption or emission remains valid only for the in-plane component, the z -component being fixed by the quantum well width. Accordingly, an exciton with wavevector $\mathbf{k}_X = (\mathbf{k}_{\parallel}^X, k_z^X)$ will interact with a photon with the same in plane wavevector but with any value of k_z^{γ} . There is thus a density of states for radiative decay given by (see [39]):

$$\rho_{2D}(\mathbf{k}_{\parallel}, \hbar\omega) \equiv \sum_{k_z} \delta(\hbar\omega - \frac{\hbar c}{n_{QW}} \sqrt{\mathbf{k}_{\parallel}^2 + k_z^2}) \propto \frac{\hbar\omega}{\sqrt{(k_0^2 - \mathbf{k}_{\parallel}^2)}} \Theta(k_0 - |\mathbf{k}_{\parallel}|) \quad (1.43)$$

where where n_{QW} is the refractive index in the QW, $k_0 = n_{QW}\omega/c$ is the wavevector of the photon in the material and Θ is the Heaviside step function. Only states with $|\mathbf{k}_{\parallel}| < k_0$ can couple to light giving rise again to two class excitons.

- States with $|\mathbf{k}_{\parallel}^X| < k_0$ that couple to light. These states have a finite radiative lifetime $1/\gamma_X$ given by the Fermi Golden rule. They lie on the left of the light cone in the $\mathbf{k}_{\parallel} - \omega$ plane.
- States with $|\mathbf{k}_{\parallel}^X| > k_0$ that do not decay radiatively. They lie on the right of the photon line in the the $\mathbf{k}_{\parallel} - \omega$ plane. They are analog to surface modes as they have a vanishing electric field far from the QW. These states join the previously described excitons that could not couple to light because of their spin configuration to form a wider class of "dark" excitons.

This stands in contrast to bulk semiconductors, where a single exciton mode couples exclusively to a single photon mode. Nevertheless, if we also impose energy conservation between the exciton and the photon mode the maximum in-plane wavevector of radiative excitons gets modified and depend on the exciton energy. To see this let us consider an initial state made of an exciton of overall energy $E_X(\mathbf{k}_{\parallel}^X)$ and zero photon and a final state made of a single photon with energy $E_{\gamma}(\mathbf{k}_{\parallel}^{\gamma}) = \frac{\hbar c}{n_{QW}} \sqrt{(\mathbf{k}_{\parallel}^{\gamma})^2 + (k_z^{\gamma})^2}$ and no exciton. The energy conservation of this process reads :

$$E_X(\mathbf{k}_{\parallel}^X) = E_{\gamma}(\mathbf{k}_{\parallel}^{\gamma}) \quad (1.44a)$$

$$E_X^{QW} + \frac{(\hbar\mathbf{k}_{\parallel}^X)^2}{2m_X} = \frac{\hbar c}{n_{QW}} \sqrt{(\mathbf{k}_{\parallel}^{\gamma})^2 + (k_z^{\gamma})^2}, \quad (1.44b)$$

in which we set $E_X^{QW} = E_g^{QW} + E_X^{1s} = E_g^{QW} + E_1^e + E_1^h - R_X^{QW}$. Injecting the in-plane momentum conservation and imposing $k_z^{\gamma 2} \geq 0$ for the photon field to be propagative the above condition restricts the exciton that can couple to light through :

$$|\mathbf{k}_{\parallel}^X| \leq \frac{cm_X}{n_{QW}\hbar} \left(1 + \sqrt{1 - \frac{4n_{QW}E_X^{QW}}{m_Xc^2}} \right). \quad (1.45)$$

Since E_X^{QW} can be neglected with respect to the exciton mass energy m_Xc^2 the above condition taken at first order gives :

$$|\mathbf{k}_{\parallel}^X| \leq \frac{n_{QW} E_X^{QW}}{\hbar c}. \quad (1.46)$$

Excitons with higher wavevector are than forbidden to exchange energy with light. However, in our case we have $E_X^{QW} \simeq 1.485/\text{meV}$ and $n_{QW} \simeq 3.5$ leading to $|\mathbf{k}_{\parallel}^X| \leq 30/\mu\text{m}^{-1}$ which is way beyond the values addressed in the experiment. Now that the exciton formation is well established let us have a look at the mechanisms that can lead them to interact.

1.2.7 Exciton-exciton interaction

The scope of this section is to answer the question of what can lead two excitons in states (i,j) to end up in states (f,g) . Obviously, direct coulomb interactions between the excitons constitutive is an unambiguous valid answer. Nonetheless, an interaction giving the same result can also occur in the absence of any Coulomb interactions via pure carrier exchange. Namely, excitons i and j can exchange either their electron or hole. The latter is a direct consequences of the Pauli exclusion principle stating that two fermions cannot occupy the same quantum state.

1.2.7.1 Coulomb interaction

As explained in the previous section, holes and electrons undergo Coulomb interaction. As a consequence, the interaction between two excitons (e_1,h_1) and (e_2,h_2) consist of $V_{e_1e_2} + V_{h_1h_2} + V_{e_1h_2} + V_{h_1e_2}$. However, if the exciton were made of (e_1,h_2) and (e_2,h_1) the cross term in the interaction potential would be replaced by $V_{e_1h_1} + V_{e_2h_2}$. Because there are different possible ways to form excitons, the total interaction energy depends on the specific pairing choice. This makes it impossible to define a single, clean exciton-exciton interaction potential that works in all cases. Hence, treating them as pure bosons with a simple interaction potential fail because the effective exciton-exciton potential is not unique and depends on the microscopic way the excitons are formed. Nevertheless, it is clear that, through Coulomb interaction, excitons can change states and thus interact in the most general sense. This being said, we will as experimentalist, focus on the most important scattering process that is actually coming from exchange carrier among excitons and that is a unique feature of composite particle.

1.2.7.2 Fermionic exchange interaction

Let us consider two excitons $X_1 = |\mathbf{k}_e, \mathbf{k}_h\rangle$ and $X_2 = |\mathbf{k}'_e, \mathbf{k}'_h\rangle$. If their wavefunction start to overlap the two electrons for example might see their quantum state becoming almost equal which is forbidden by the Pauli exclusion principle. To regularize this situation the exciton can exchange their carrier to form $X'_1 = |\mathbf{k}'_e, \mathbf{k}_h\rangle$ and $X'_2 = |\mathbf{k}_e, \mathbf{k}'_h\rangle$. This is might look counterintuitive since exchanging two particles in the same quantum state doesn't seem to solve the problem. However, it's truly the exchange process itself put together with wavefunction symmetries that modify the quantum state configuration to avoid Pauli principle violation. Take two indistinguishable particles, in state ψ_a and ψ_b in a 1D system [6]. Normalization consideration aside, the wavefunction of the system can be written in two ways : $\psi_{ab} = \psi_a(x_1)\psi_b(x_2) \pm \psi_a(x_1)\psi_b(x_2)$. Depending on the plus or minus sign, the wavefunction

is symmetric or antisymmetric under position exchange. The two different configurations imply different physics. For instance the mean value of the particle interdistance is :

$$\langle(x_1 - x_2)^2\rangle = \langle x_1^2 \rangle + \langle x_2^2 \rangle \mp 2\langle x_1 x_2 \rangle, \quad (1.47)$$

provided the wavefunctions overlap $\langle x_1 x_2 \rangle \neq 0$, the expected value is decreased for bosons and increased for fermions. Although, it seems to act as a force repelling or attracting particles, it is rather a geometrical constraint arising from the Pauli principle and the quantum nature of the particle at stake. This is precisely what happened during carrier exchange and can, at the end, lead to scattering processes between excitons. Forgetting about this interaction and trying to fully bosonize excitons would then be a mistake [3]. As an example, some features experimentally measured like exciton stark effect, precisely needs to put exchange carrier on the table to be understood [17; 20; 27]. Furthermore, in a 2D quantum well system this scatterings are dominant at larger scale while direct Coulomb interactions are dominant at scales smaller than the Bohr radius of excitons. Therefore, by considering only radiative modes, i.e. dynamics occurring on scales much larger than the Bohr radius of excitons $ka_X \ll 1$, Coulomb interactions can be neglected. Despite all the differences with true bosons above mentioned and the hot debates still going on about polaritons interactions [8; 11] this enable us, as experimentalist, to escape from ambiguity and write the main exciton-exciton potential that will be relevant in the experiment reported in this work. Written in momentum space this exciton-exciton potential $V_{XX}(\mathbf{k})$ appear as four body contact interaction [33]. The corresponding hamiltonian follows as :

$$\mathcal{H}_{XX} = \frac{1}{2} \sum_{\mathbf{k}, \mathbf{k}', \vec{q}} V_{XX}(\vec{q}) \hat{b}_{\mathbf{k}+\vec{q}}^\dagger \hat{b}_{\mathbf{k}'-\vec{q}}^\dagger \hat{b}_{\mathbf{k}} \hat{b}_{\mathbf{k}'}. \quad (1.48)$$

The potential $V_{XX}(\vec{q})$ is a function of the exchanged momentum \vec{q} . However, it can be approximated by a constant in the limit of low wavevectors since, being four order of magnitude heavier than microcavities photons, their varies only slightly with \mathbf{k} in the range of the photon wavevector that excite them. Therefore V_{XX} can be assumed constant. The numerical calculation gives $A \times V_{XX} \simeq 3 \mu\text{eV}\cdot\mu\text{m}^2$ for our InGaAs system.

$$V_{XX} = \frac{e^2 a_X^{QW}}{\epsilon A}, \quad (1.49)$$

with A the quantization area equal to the quantum well surface. The numerical calculation gives $A \times V_{XX} \simeq 3 \mu\text{eV}\cdot\mu\text{m}^2$ in our GaAs-InGaAs system.

Dark excitons creation through carrier exchange.

As discussed in subsection 1.2.5 electron-hole pairs with a total spin of ± 1 are coupled to $\sigma \pm$ photons, meaning that photon absorption leads to the creation of only bright exciton states ± 1 . However, dark exciton states can also be present in the system, arising from fermion exchange processes. Namely, fermion exchange between two bright excitons $(+1, 1)$ made of $(\mp 1/2)$ electrons and $(\pm 3/2)$ holes leads to dark excitons $(+2, -2)$. Hence, even though photon absorption only create bright excitons, excitons not coupled to light are likely to be indirectly excited and participate to the overall interactions of the system. This being said,

we will in the following only tackle this problem from a phenomenological point of view and consider the exciton-exciton interaction as a unique potential V_{XX} whereas dark excitons will be accounted for through a reservoir.

1.3 Excitons-polaritons

So far we described separately microcavity photons and excitons both in bulk and 2D systems. Microcavity polaritons arise from the strong coupling between these two components. Remarkably, the half light half matter nature of polaritons allows them to inherit the best of both worlds namely the low photon effective mass and the strong excitons non linear interactions. In this section we will describe the formation of polaritons by describing how placing a 2D semiconducting quantum well in an optical microcavity to enhance the light-matter interactions. To start with let us have a look again at the Fermi Golden rule giving the spontaneous emission rate from a level $|i\rangle$ to a level $|f\rangle$ in a continuum of states per unit time in the presence of a weak coupling W :

$$\Gamma_{i \rightarrow f} = \frac{2\pi}{\hbar} \left| \langle f | W | i \rangle \right|^2 \rho(E_f) \delta(E_f - E_i) \quad (1.50)$$

where $\rho(E_f)$ is the density of states at energy E_f and $\delta(E_f - E_i)$ ensures energy conservation. Say, we want to "force" an exciton to recombine in a given photonic state $(\hbar\omega_\gamma, \mathbf{k}_\gamma)$. In a 2D quantum well, an exciton with in plane wavevector \mathbf{k}_\parallel^X is allowed to couple to a continuum of photon modes provided their wavevectors respect [Equation 1.46](#). Solving this problem boils down to changing the density of state ρ in order to suppress spontaneous emission in all unwanted modes. As usually done in cavity quantum electrodynamics, this problem is tackled by embedding the quantum well in a high finesse optical microcavity as shown in [Figure 1.8 \(a\)](#).

The role of the latter is to create a set of resonant modes that will act as a "filter" for the exciton recombination. The quantization axis of the optical microcavity is chosen to be the same as the quantum well and the light-matter interactions are optimized by placing the quantum well at the antinode of the electric field. The cavity length is chosen so that single photonic mode can be equal the excitonic energy. This matching can be seen by looking simultaneously at the exciton and photon dispersion relation as a function of the in plane wavevector and check that they cross each other at a finite wavevector. For instance in the case of [Figure 1.8 \(b\)](#) the cavity has been designed so that the exciton and photon energies are equal at $\mathbf{k}_\parallel = 0$. Several quantum well can then be stacked in the cavity to enhance the interactions provided that they are once again located at antinodes of the photonic field. In the experiment we use a $3\lambda/2$ made of two planar DBR in which are placed three $InGaAs/GaAs$ quantum wells. An extended description of the fabrication procedure to build such a sample can be found in [24]. However, the main features mentioned so far can be summarized in a few points :

- The cavity is made by embedding semiconducting quantum wells in between two distributed bragg reflectors forming a high finesse optical microcavity.
- The length of the cavity and of the wells are chosen so a single longitudinal mode of the electric field is resonant only with the 1s state of the exciton.

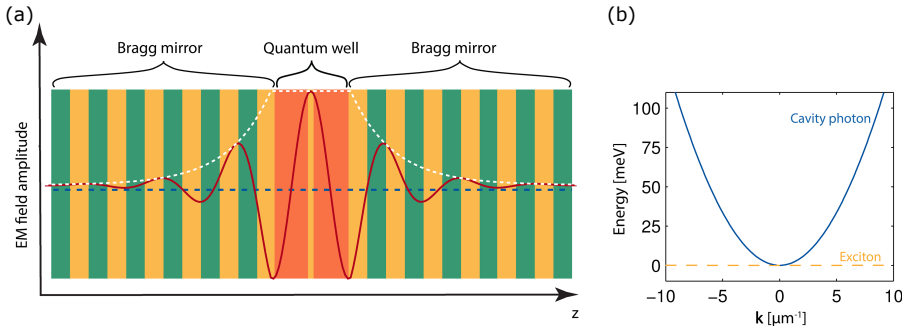


Fig. 1.8 **Schematic representation of a quantum well embedded in an optical microcavity.** The quantum wells are placed at the antinode of the electric field of the cavity. The cavity is designed to have a single mode that matches the exciton energy. (b) Dispersions relation of the exciton (yellow) and photon (blue) modes in a typical microcavity. Since the exciton effective mass m_X is 10^4 times larger than the photon mass the exciton dispersion looks flat with respect to the photon. The cavity has been designed so the $\mathbf{k}_{\parallel} = 0$ energies are matched.

- The exciton are confined in the xy -plane in each quantum well and the exciton density can be tuned by changing the number of quantum wells.
- Momentum conservation still holds in the plane of the cavity. Namely, an incoming photon with wavevector \mathbf{k}_{\parallel} will create an exciton with the same in-plane wavevector.

It appears then that the relevant motion of the interacting particles at stake lies in the xy -plane since the wavevectors in the z -direction are fixed by the cavity parameters. Consequently, for sake of clarity, we will only refer to the in-plane wavevector in the following by dropping the \parallel label and just write \mathbf{k} .

Now that some efforts were put in enhancing exciton-photon interactions let us see the different coupling regimes that we can be reached in such samples.

Coupling regimes. At first approximation the problem can be thought as two bath of particles exchanging quanta at a rate Ω_R . Depending on the efficiency of this exchange compared to the damping rate of each bath γ_X and γ_{γ} one has to revisit the way to describe the system. Indeed, when $\Omega_R \ll \gamma_X, \gamma_{\gamma}$ the system is said to be in the weak coupling regime. It can be understood in terms of lifetimes : both excitons and photons lifetimes are too short compared to the characteristic time of the exchange $1/\Omega_R$. The energy leaks out of the system before it can change from one state to the other. The exciton-photon interaction is in this case irreversible. If $\Omega_R \gg \gamma_X, \gamma_{\gamma}$ the system is said to be in the strong coupling regime. In a given photonic (or excitonic) lifetime $1/\gamma_{cav}$, the answer to the question "where is the energy ?" is no longer clear. Indeed the energy have had enough time to coherently go back and forth between exciton and photon states plenty of times. Translating this in quantum mechanics language simply means that the system is in a superposition of exciton and photon states. Polariton then rise in this regime as a superposition of microcavity photons and excitons exchanging energy at the so called Rabi frequency Ω_R .

Linear Hamiltonian. Let us write formally the coupling between excitons and photons described above. First we tackle the weak optical excitation scheme in which non linear interactions among excitons can be neglected. The corresponding linear Hamiltonian is given by :

$$\mathcal{H}_{lin} = \sum_{\mathbf{k}} \left[E_X(\mathbf{k}) b_{\mathbf{k}}^\dagger b_{\mathbf{k}} + E_\gamma(\mathbf{k}) a_{\mathbf{k}}^\dagger a_{\mathbf{k}} + \frac{\hbar\Omega_R}{2} a_{\mathbf{k}}^\dagger b_{\mathbf{k}} + a_{\mathbf{k}} b_{\mathbf{k}}^\dagger \right] \quad (1.51)$$

where $b_{\mathbf{k}}^\dagger$ and $a_{\mathbf{k}}^\dagger$ are the creation operators of the exciton and photon modes respectively. The first two terms account for the energies of the excitons and the photons while the terms $b_{\mathbf{k}}^\dagger a_{\mathbf{k}}$ and $a_{\mathbf{k}}^\dagger b_{\mathbf{k}}$ account for the linear exciton-photon coupling yielding an interaction energy $\hbar\Omega_R$. Obviously this hamiltonian is not diagonal in the excitons-photons operators basis. Excitons-polaritons then arise as the two eigenstates of \mathcal{H}_{lin} : the upper and the lower polaritons whose creation and annihilation operators are $(u_{\mathbf{k}}^\dagger, u_{\mathbf{k}})$ and $(p_{\mathbf{k}}^\dagger, p_{\mathbf{k}})$ respectively. These operators can be found by an unitary transformation on the exciton-photon basis that was extensively used by Hopfield [15] :

$$\begin{bmatrix} p_{\mathbf{k}} \\ u_{\mathbf{k}} \end{bmatrix} = \begin{bmatrix} C_{\mathbf{k}} & X_{\mathbf{k}} \\ X_{\mathbf{k}} & -C_{\mathbf{k}} \end{bmatrix} \begin{bmatrix} a_{\mathbf{k}} \\ b_{\mathbf{k}} \end{bmatrix}, \quad (1.52)$$

where $C_{\mathbf{k}}$ and $X_{\mathbf{k}}$ are the Hopfield coefficients for photons and excitons respectively. The unitarity of the transformation is reflected by the relation $C_{\mathbf{k}}^2 + X_{\mathbf{k}}^2 = 1$. As a consequence, they can be interpreted as the fractions of excitons and photons in both modes. More precisely they depend on the excitons/photons energies and the Rabi frequency as :

$$C_{\mathbf{k}}^2 = \frac{\sqrt{\Delta E_{X-\gamma}^2 + \hbar^2\Omega_R^2} - \Delta E_{X-\gamma}}{2\sqrt{\Delta E_{X-\gamma}^2 + \hbar^2\Omega_R^2}}, \quad (1.53a)$$

$$X_{\mathbf{k}}^2 = \frac{\sqrt{\Delta E_{X-\gamma}^2 + \hbar^2\Omega_R^2} + \Delta E_{X-\gamma}}{2\sqrt{\Delta E_{X-\gamma}^2 + \hbar^2\Omega_R^2}}. \quad (1.53b)$$

where $\Delta E_{X-\gamma}(\mathbf{k}) = E_\gamma(\mathbf{k}) - E_X(\mathbf{k})$ is the detuning between the exciton and the photon energies at \mathbf{k} . In this basis the linear hamiltonian can be written in its diagonal form.

$$\mathcal{H}_{lin} = \sum_{\mathbf{k}} \left[E_{LP}(\mathbf{k}) u_{\mathbf{k}}^\dagger u_{\mathbf{k}} + E_{UP}(\mathbf{k}) p_{\mathbf{k}}^\dagger p_{\mathbf{k}} \right] \quad (1.54)$$

where the eigenvalues $E_{LP}(\mathbf{k})$ and $E_{UP}(\mathbf{k})$ are the lower and upper polariton dispersion relation. Their analytical expressions are given by :

$$E_{LP}(\mathbf{k}) = \frac{E_X(\mathbf{k}) + E_\gamma(\mathbf{k})}{2} - \frac{\sqrt{\Delta E_{X-\gamma}^2 + \hbar^2 \Omega_R^2}}{2}, \quad (1.55)$$

$$E_{UP}(\mathbf{k}) = \frac{E_X(\mathbf{k}) + E_\gamma(\mathbf{k})}{2} + \frac{\sqrt{\Delta E_{X-\gamma}^2 + \hbar^2 \Omega_R^2}}{2}. \quad (1.56)$$

Tuning the exciton-photon fraction. As it can be seen the weight of photon and exciton in a given polaritonic state can be then tuned by changing the exciton-photon detuning $\Delta E_{X-\gamma}$. Particurlarly, when $\Delta E_{X-\gamma} = 0$ we have $C_{\mathbf{k}}^2 = X_{\mathbf{k}}^2 = \frac{1}{2}$ meaning that the exciton and the photon are equally mixed in the polariton states. In practice, there are two ways to change the exciton-photon detuning. The first tuning knob, which is the most obvious, is the wavevector \mathbf{k} . Since the exciton dispersion is flat with respect to the photon it boils down to move on the photon dispersion curve. Still, exciting a polariton state with a given set of Hopfield coefficients will fix the wavevector and, in some case might not be even possible. For instance if the photonic dispersion is above the exciton energy at all wavevector as in [Figure 1.9 b₁](#), it is impossible to reach the purely hybrid configuration $\Delta E_{X-\gamma} = 0$. Creating an arbitrary polaritonic state thus require a second knob to tune $\Delta E_{X-\gamma}$. It is generally done by introducing a small wedge between the two DBR that will change the photon resonance condition as shown in [Figure 1.9 a\)](#) : a change in the cavity length L will shift vertically the photon disperions. Luckily, this comes for free with the usual Molecular Beam Epitaxy method used to grow the sample. The principle is to heat the target material to its sublimation temperature to produce a molecular beam that is then deposited on a substrate to form thin atomic layers that stack on top of each other. In practice, the substrate is located on a spinning disk to avoid the molecule to clusterise. If the spinning disk is stopped, molecules will accumulate in the center of the beam and form a "hill". By taking advantages of this features it is possible to change progressively the thickness of the layer and thus the cavity resonance condition. A given sample has in fact a wide range of exciton-photon detuning that can be adressed in the lab by changing the working point on the cavity.

In general, when the exciton-photon detuning is too positive the UP branch recovers the excitons curve while the LP branch recovers the photons curve. Conversely, when the exciton-photon detuning is negative the UP branch recovers the photons curve while the LP branch recovers the excitons curve. This is not very suprising since a great detuning means that the exciton and the photon are far from each other making the coupling less efficient. At the zero detuning point $\Delta E_{X-\gamma} = 0$ the coupling is maximum and the splitting between the lower and upper polariton branch is equal to the Rabi energy frequency $\hbar \Omega_R$. Besides, the anticrossing between the two branches is a direct consequence of the strong coupling regime and can be find even in classical systems like coupled pendulums.

The suitable range of detuning for which the polariton concept is still relevant and that we can adress in the experiment is shown in [Figure 1.10](#)

Relaxation. The strong coupling condition $\Omega_R \gg \gamma_X, \gamma_{cav}$ can also be seen by directly taking into account the finite lifetime of excitons and photons, introducing imaginary energies $E_\gamma - i\gamma_{cav}$ and $E_X - i\gamma_X$ as in [7]. Doing so, the polariton dispersions relation become :

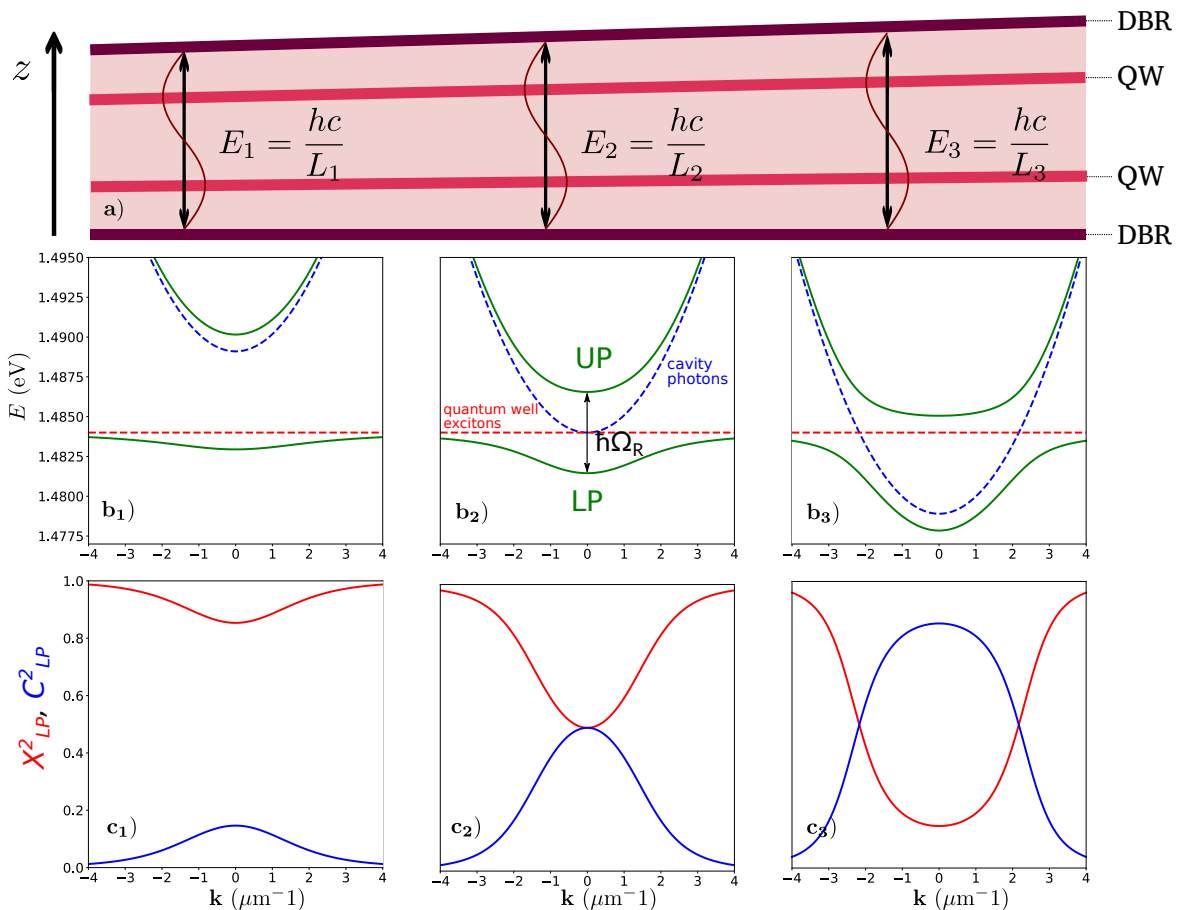


Fig. 1.9 **Scheme of an optical microcavity with a wedge, polaritons dispersion relations and Hopfield coefficients.** a) Side view of a double quantum well semiconducting microcavity. From left to right the photon resonant energy decreases as the length of the cavity increases. The exciton energy remains constant since it is fixed by the width of the quantum well. We take as example three point in the sample $i = 1,2,3$ with increasing cavity length. At each point the wavy lines represent the optical standing wave stemming from the resonance conditions $\lambda_i = L_i$. The corresponding energies E_i illustrate the three different regimes namely : $\Delta E_{X-\gamma}^{(1)}(\mathbf{k} = 0) > 0$, $\Delta E_{X-\gamma}^{(2)}(\mathbf{k} = 0) = 0$, $\Delta E_{X-\gamma}^{(3)}(\mathbf{k} = 0) < 0$. Each E_i corresponds to the subplots b_i) and c_i). b₁), b₂), b₃) Dispersion relations of the lower (LP) and upper polaritons (UP) in a typical microcavity for each value of $\Delta E_{X-\gamma}^{(i)}$. The exciton energy is the yellow dashed line while the photon energy is the blue dashed line. Depending on the location on the sample $i = 1,2,3$ the photon dispersion curve gets shifted vertically yielding different values of the Hopfield coefficient. c₁), c₂), c₃) Corresponding Hopfield coefficients as a function of the in-plane wavevector for the three different regimes. Adapted from [5].

$$\begin{aligned} E_{UP,LP}(\mathbf{k}) &= \frac{E_\gamma(\mathbf{k}) + E_X(\mathbf{k})}{2} - i\hbar \frac{\gamma_{cav} + \gamma_X}{2} \\ &\pm \frac{1}{2} \sqrt{[\hbar\Omega_R]^2 + [\Delta E_{X-\gamma} - i\hbar(\gamma_{cav} - \gamma_X)]^2}. \end{aligned} \quad (1.57)$$

At zero detuning we obtain :

$$E_{UP,LP}(\mathbf{k}) = E_X(\mathbf{k}) - i\hbar \frac{\gamma_{cav} + \gamma_X}{2} \pm \frac{1}{2} \sqrt{(\hbar\Omega_R)^2 + (\hbar\gamma_{cav} - \hbar\gamma_X)^2}. \quad (1.58)$$

The existence of two distinct energies for the two polaritons modes thus depends on the relative values of Ω_R and $|\gamma_{cav} - \gamma_X|$. If the coupling constant Ω_R is smaller than the difference between the relaxation constants, the two eigenenergies share the same real part, and the degeneracy between the exciton and the cavity mode remains unbroken. Being a supersposition of excitons and photons the polaritons also have a relaxation rate that can then be inferred from the imaginary part of their energy :

$$\gamma_{UP}(\mathbf{k}) = X_{\mathbf{k}}^2 \gamma_{cav} + C_{\mathbf{k}}^2 \gamma_X, \quad (1.59a)$$

$$\gamma_{LP}(\mathbf{k}) = X_{\mathbf{k}}^2 \gamma_X + C_{\mathbf{k}}^2 \gamma_{cav}. \quad (1.59b)$$

Once again, the hopfield coefficient have a strong impact on the polariton relaxation rate. In the range of detuning available in our sample we measure relaxation rates of the order of 70 μeV which correspond to a lifetime $\tau \sim 10 \text{ ps}$. This value is beyond the time response of a wide class of instruments and require generally both pulsed lasers and ultrafast detection devices to be resolved as in [38]. The present work is not dedicated to time resolved experiments as we rather use a continuous wave laser to constantly compensate for the losses and reach a steady state from which we extract observable quantities. This system is then highly out of equilibrium. Although this feature seems limiting at first sight it can actually turn into an asset whenever one wants to study dynamical instabilities. Indeed, in conservative systems, instabilities are difficult to study precisely because they tend to make the system unstable. In the case of polaritons, the losses can reduce their effect while keeping their signature visible in the steady state of the system [4].

Effective mass. By analogy with what was done for the photons in section 1.1 it is possible to affiliate an effective mass to the polaritons by taking the second derivative at the bottom of the polariton dispersion relation, namely :

$$\frac{1}{m_{UP}} = \frac{X_0^2}{m_X} + \frac{C_0^2}{m_\gamma}, \quad (1.60a)$$

$$\frac{1}{m_{LP}} = \frac{X_0^2}{m_\gamma} + \frac{C_0^2}{m_X}. \quad (1.60b)$$

Reminding that $C_0^2 + X_0^2 = 1$ and that $\frac{m_\gamma}{m_X} \ll 1$. It can be cast in the following form :

$$m_{UP} \approx \frac{m_\gamma}{X_0^2} \quad (1.61a)$$

$$m_{LP} \approx \frac{m_X}{C_0^2} \quad (1.61b)$$

It can be seen that polaritons inherit the low effective mass of the photons making their transport easier than for excitons. This is particularly interesting for the realisation of polaritonic circuits in the framework of quantum information processing [23]. The excitonic part of the polariton also bring its own features to the table. In particular, the strong exciton-exciton non linear interactions that will turn light into a fluid of interacting particles. This is the subject of the next section.

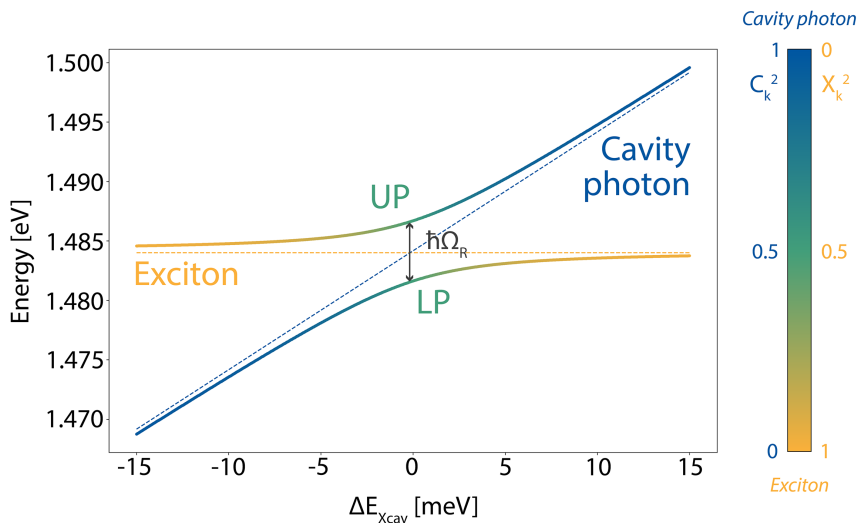


Fig. 1.10 **Anticrossing in the strong coupling regime.** Energies of the upper (UP) and lower (LP) polariton branches at $\mathbf{k} = 0\mu\text{m}^{-1}$, with respect to the exciton-photon detuning at zero wavevector $\Delta E_{X-\gamma}(\mathbf{k} = 0)$ and the color-coded squared modulus of the Hopfield coefficient X^2 (exciton) and C^2 (photon). The yellow and blue dashed lines are respectively the bare exciton and photon energies. At $\Delta E_{X-\gamma} = 0$ meV, the coupling is the better yielding an energy splitting equal to the Rabi energy $\hbar\Omega_R$. Adapted from [24]

1.3.1 Polariton interactions

It is now clear that shinning a strong laser with the right frequency on a semiconducting microcavity will create plenty of polaritons. Since they have an excitonic part, they may undergo many body effects that were not taken into account in the linear hamiltonian model derived earlier. More precisely, polaritons experience all the exciton-exciton interactions described in subsection 1.2.7 as well as additional features coming from their coupling with light. Remarkably, in high density regime the Pauli principle has to apply again on the electrons and the holes leading to carrier exchanges. In the absence of light these fermionic

exchanges are actually the dominant scatterings processes while the direct Coulomb scattering is negligible as was explained in subsection 1.2.7. We remind the expression of the resulting exchange hamiltonian :

$$\mathcal{H}_{XX} = \frac{1}{2} \sum_{\mathbf{k}, \mathbf{k}', \mathbf{q}} V_{XX} [p_{\mathbf{k}+\mathbf{q}}^\dagger p_{\mathbf{k}'-\mathbf{q}}^\dagger p_{\mathbf{k}} p_{\mathbf{k}'}] \quad (1.62)$$

When the excitons are strongly coupled to cavity photon these carrier exchanges give rise to an additional saturation potential describing what was called a "photon-assisted exchange scattering" in the proposal of [8].:

$$\mathcal{H}_{sat} = \frac{1}{2} \sum_{\mathbf{k}, \mathbf{k}', \mathbf{q}} V_{sat} [a_{\mathbf{k}+\mathbf{q}}^\dagger b_{\mathbf{k}'-\mathbf{q}}^\dagger b_{\mathbf{k}} b_{\mathbf{k}'} + h.c.] , \quad (1.63)$$

where V_{sat} is the saturation potential that can be computed by applying the Usui transformation on the quantum wells [37].

$$V_{sat} = \frac{\hbar \Omega_R}{A n_{sat}}, \quad (1.64)$$

in which n_{sat} is the saturation density computed from the 2D exciton bohr radius as $n_{sat} = 1/a_X^{QW}$ and A the macroscopic quantization area. This scattering can be understood from a microscopic point of view. Consider two excitons, i_1 and i_2 , in a first step they exchange their carrier without any Coulomb process giving two other excitons i'_1 and i'_2 . In a second step, one of the exciton, let us say i'_1 find itself in the same state than a neighbouring exciton. Because of the Pauli principle it can not stay in this state. Luckily it is coupled to cavity photon which enable it to get out of this irregular situation by emitting a photon. To end up with a description of interactions in the polariton basis we invert the unitary transformation in Equation 1.52 :

$$b_{\mathbf{k}} = X_k p_{\mathbf{k}} - C_k u_{\mathbf{k}}, \quad (1.65a)$$

$$a_{\mathbf{k}} = C_k p_{\mathbf{k}} + X_k u_{\mathbf{k}}, \quad (1.65b)$$

and inject these expressions into \mathcal{H}_{XX} and \mathcal{H}_{sat} . We end up with a single polariton-polariton potential that is a combination of hopfield coefficients, V_{sat} and V_{XX} . For the lower polaritons, which are the one we excite in the experiment and to which we will restrict in the following we obtain an effective polariton-polariton potential V_{pp} as :

$$V_{pp} = |X_{\mathbf{k}}|^4 V_{XX} + 2|X_{\mathbf{k}}|^2 X_{\mathbf{k}} C_{\mathbf{k}} V_{sat}. - \quad (1.66)$$

Once again it depends on the exciton-photon fraction through the Hopfield coefficients, and, in the purely hybrid situation $\Delta E_{X-\gamma}=0$, yields $A \times V_{pp} = 1 \text{ } \mu\text{eV } \mu\text{m}^{-2}$ in our sample.

Non linear LP hamiltonian. Finally, taking into account the polariton-polariton interactions abovementioned the linear hamiltonian for Lower Polaritons can be completed as follows :

$$\mathcal{H}_{LP} = \sum_{\mathbf{k}} \hbar \omega_{LP}(\mathbf{k}) p_{\mathbf{k}}^\dagger p_{\mathbf{k}} + \frac{1}{2} \sum_{\mathbf{k}, \mathbf{k}', \mathbf{q}} V_{pp} [p_{\mathbf{k}+\mathbf{q}}^\dagger p_{\mathbf{k}'-\mathbf{q}}^\dagger p_{\mathbf{k}} p_{\mathbf{k}'}]. \quad (1.67)$$

Energy renormalization. As it can already be seen in the LP non linear hamiltonian, the bare polartion energies are no longer eigenvalues of the system in the presence of interactions. To give a simple picture of this feature let us restrict the description to two polariton modes $p_{\mathbf{k}_1}$ and $p_{\mathbf{k}_2}$. If the system is prepapred in such a way as to populate one of the two modes, \mathbf{k}_2 , this macroscopic reservoir of polaritons acts as an external potential for the polaritons in the poorly populated mode \mathbf{k}_1 . Consequently, the energy of the polaritons in mode \mathbf{k}_1 increases by an amount corresponding to the potential created by the polaritons in mode \mathbf{k}_2 . This is a phenomenon of energy renormalization.

To be more quantitative, we can write the Hamiltonian of the system while restricting it to these two modes. In this case, \mathcal{H}_{int} is the sum of $p_{\mathbf{k}_1}^\dagger p_{\mathbf{k}_2}^\dagger p_{\mathbf{k}_1} p_{\mathbf{k}_2}$ and $p_{\mathbf{k}_2}^\dagger p_{\mathbf{k}_1}^\dagger p_{\mathbf{k}_2} p_{\mathbf{k}_1}$. Since $p_{\mathbf{k}_2}$ and $p_{\mathbf{k}_1}$ are eigenstates of the system, they commute, meaning that the two previous term account for the same scattering. The time evolution of $p_{\mathbf{k}_1}$ can then be described by the Heisenberg equation :

$$i\hbar \frac{d}{dt} p_{\mathbf{k}_1} = [p_{\mathbf{k}_1}, \mathcal{H}_{LP}] = [p_{\mathbf{k}_1}, \mathcal{H}_{lin}] + [p_{\mathbf{k}_1}, \mathcal{H}_{int}]. \quad (1.68)$$

the interacting term being :

$$[p_{\mathbf{k}_1}, \mathcal{H}_{int}] = \frac{V_{pp}}{2} p_{\mathbf{k}_2}^\dagger p_{\mathbf{k}_2} p_{\mathbf{k}_1} = \frac{\hbar g_{LP}}{A} \hat{N}_2 p_{\mathbf{k}_1}. \quad (1.69)$$

\hat{N}_2 is the number operator in mode \mathbf{k}_2 and $\hbar g_{LP} = V_{pp} A / 2$ is the polariton-polariton interaction constant. Since, the mode \mathbf{k}_2 is macroscopically populated, we can replace \hat{N}_2 by its expectation value $\langle \hat{N}_2 \rangle$, which exhibit the polariton density in mode \mathbf{k}_2 , $n_2 = \langle \hat{N}_2 \rangle / A$. As a result, the master equation for the \mathbf{k}_1 gets renormalized by interactions with the \mathbf{k}_2 mode as :

$$i\hbar \frac{d}{dt} p_{\mathbf{k}_1} = [\hbar \omega_{LP}(\mathbf{k}_1) + \hbar g_{LP} n_2] p_{\mathbf{k}_1}. \quad (1.70)$$

where $\omega_{LP}(\mathbf{k}_1) = E_{LP}(\mathbf{k}_1)$ is the bare energy of the polariton with wavevector \mathbf{k}_1 . Although this is a simplified model with only two modes, the equation demonstrates how interactions between polaritons can lead to the renormalization of their energies. More generally, this phenomenon takes place between all modes in the system, including self-interactions of individual modes. The latter closely resembles the optical Kerr effect, where a field modifies the refractive index of the medium through which it propagates.

1.4 Polariton dynamics

To summarize, microcavity exciton-polaritons are hybrid light-matter quasiparticles that combine characteristics of both components. Their photonic part endows them with an

exceptionally low effective mass and allows us to manipulate them using light. Conversely, their excitonic part provides them with the exotic properties associated with electrons in semiconductors. Although the resulting interactions are varied and stem from different origins, they can, to a first approximation, be described by a single four-body contact potential, V_{pp} .

In this framework, polaritons can be viewed as weakly interacting bosons, distinguished by their inherent losses, making their behavior an out-of-equilibrium problem. In the following, we will explore their dynamics when one or a few modes are macroscopically populated, revealing remarkable phenomena typically associated with true many-body bosonic systems, such as superfluidity and Bose-Einstein condensation (BEC). However, whenever necessary, we will return to their composite fermionic nature to account for unique features that may not be captured by the mean field approximation.

1.4.1 Mean field approximation

In order to describe the dynamics of the polariton fluid of light, it is convenient to use the mean field approximation as it is usually done for quantum fluids [30]. This assumption is valid when the number of particles is large $N \sim N + 1$ and when the major part of them occupy the same quantum state. Obviously, the latter can happen only in bosonic systems since fermions obey the Pauli exclusion principle. In atomic systems, the macroscopic occupation occurs in the ground state of the system, and, provided that the temperature is low enough, happens spontaneously due to bosonic stimulation. In the case of polaritons, the situation is dramatically different since the system is out of equilibrium and the particles have to be continuously pumped to compensate for the losses. The mean field of the system is then rather a steady state than a ground state at equilibrium. This being said, it is still possible to define a macroscopic occupation of a given mode in the system. Whenever this happens, the theoretical procedure boils down to replacing the field operator $\hat{\psi}(\mathbf{r},t) = \sum_k \varphi_k \hat{p}_k$ that annihilates a particle at (\mathbf{r},t) , by its expectation value $\langle \hat{\psi}(\mathbf{r},t) \rangle$. This idea is supported by the fact that, in such situations, adding or removing a particle from the system does not change its state. The system is then described by a single classical wavefunction whose square modulus gives the density of particles in the system $|\psi(\mathbf{r},t)|^2 = n(\mathbf{r},t)$ and with a well defined phase accounting for long range coherence. However, it doesn't mean that the system has became fully classical. Indeed, its quantum nature is hidden in the fluctuations around the mean field and often manifest itself through collective behavior. Accounting for these fluctuations is done by adding a small perturbation to the mean field :

$$\hat{\psi}(\mathbf{r},t) = \langle \psi(\mathbf{r},t) \rangle + \delta\psi(\mathbf{r},t). \quad (1.71)$$

For now let us focus on the description of the mean field dynamics and justify more quantitatively the relevance of describing a polariton fluid with a single wavefunction.

One wavefunction to rule them all. A pioneering result in the early stages of quantum mechanics is the so called wave-particle duality proposed by Louis de Broglie [10] in 1924. It states that particles can exhibit both wave and particle properties. More precisely, to any particle with momentum \mathbf{p} can be associated a wavelength $\lambda = h/|\mathbf{p}|$. This wavelength is the characteristic of the wave associated with the particle and is called the de Broglie wavelength. As a result if two particle are separated by a distance smaller than their de

Broglie wavelength their corresponding wavefunction will sum and possibly give rise to wave like effect as interferences. This idea was later confirmed by the famous double slit experiment in which electrons were sent through a double slit and displayed an interference pattern.

If one apply this idea to a great number of particle in the same quantum states whose inter-particle distance is smaller than λ it is no longer possible to distinguish them and they can be described by a single wavefunction. At thermal equilibrium the momentum of a particle follows a Maxwell Boltzmann distribution and the de Broglie wavelength is of the order of the thermal de Broglie wavelength :

$$\lambda_T = \frac{h}{\sqrt{2\pi m k_B T}}, \quad (1.72)$$

where T is the temperature m the particle mass and k_B the Boltzmann constant. From this simple formula, one can see why reaching long range coherence in a system often require trapping and cooling procedures. In the case of polaritons, a typical polariton-polariton inter-distance is about $0.1 \mu\text{m}$ while the small polaritons effective mass and the cryogenic temperature ($\sim 4K$) yields a thermal de Broglie wavelength of the order of $1 \mu\text{m}$ which validates the mean field approximation. Now that we have a single order parameter to describe the system, let us see how it evolves in time.

1.4.2 Driven dissipative Gross-Pitaevskii Equation.

In the context of Bose gas this problem was first tackled by Gross [12] and Pitaevskii [29] to describe the structure of quantized vortices in liquid Helium. The resulting equation is known as the *Gross-Pitaevskii equation* or non-linear Schrödinger equation :

$$i\hbar \frac{\partial}{\partial t} \psi(\mathbf{r}, t) = \left(-\frac{\hbar^2}{2m} \nabla_{\mathbf{r}}^2 + V_{ext}(\mathbf{r}) + \hbar g |\psi(\mathbf{r}, t)|^2 \right) \psi(\mathbf{r}, t), \quad (1.73)$$

where g is the interaction constant, $\nabla_{\mathbf{r}}$ the kinetic energy and $V_{ext}(\mathbf{r})$ is the external potential experienced by the particles. To extend this equation to the out of equilibrium polariton case, a first formulation in terms of exciton and photon reveals to be enlightening to identify the various corrections that must be considered. Losses are incorporated through the relaxation rates γ_X and γ_{cav} while the continuous injection of photons in the system is accounted for by a pumping term $F_p(\mathbf{r}, t)$ in the photon field master equation. Considering these terms we end up with a set of coupled equation for the exciton and photon fields $\psi_X(\mathbf{r}, t)$, $\psi_{\gamma}(\mathbf{r}, t)$:

$$i\hbar \frac{d}{dt} \begin{bmatrix} \psi_{\gamma}(\mathbf{r}, t) \\ \psi_X(\mathbf{r}, t) \end{bmatrix} = \begin{bmatrix} \hbar F_p(\mathbf{r}, t) \\ 0 \end{bmatrix} + \left(\mathcal{H}_{lin}(\mathbf{r}) + \begin{bmatrix} V_{\gamma}(\mathbf{r}) - i\hbar \frac{\gamma_{cav}}{2} & 0 \\ 0 & V_X(\mathbf{r}) - i\hbar \frac{\gamma_X}{2} + \hbar g_{XX} n_X(\mathbf{r}, t) \end{bmatrix} \right) \begin{bmatrix} \psi_{\gamma}(\mathbf{r}, t) \\ \psi_X(\mathbf{r}, t) \end{bmatrix}, \quad (1.74)$$

where $V_{\gamma}(\mathbf{r})$ and $V_X(\mathbf{r})$ are the mean external potentials felt by photons and excitons respectively, $g_{XX} = A V_{XX} / 2\hbar$ is the exciton interaction strength and $n_X = |\psi_X|^2$ is the exciton

density. Additionally, $\mathcal{H}_{lin}(\mathbf{r})$ corresponds to the linear Hamiltonian from [Equation 1.54](#), expressed in real space by substituting \mathbf{k} with $i\nabla_{\mathbf{r}}$.

$$\mathcal{H}_{lin}(\mathbf{r}) = \begin{bmatrix} \hbar\omega_X & \hbar\Omega_R/2 \\ \hbar\Omega_R/2 & \hbar\omega_{\gamma}(-i\nabla_{\mathbf{r}}) \end{bmatrix}. \text{https://doi.org/10.1103/PhysRevLett.61.117} \quad (1.75)$$

as explained earlier, the exciton dispersion relation can be safely considered constant with respect to the photon one, $\hbar\omega_X(\mathbf{k}) = \hbar\omega_X(0)$. We can then transition to the polariton basis, obtaining two decoupled equations for the lower and upper polariton fields, $\psi_{LP}(\mathbf{r},t)$ and $\psi_{UP}(\mathbf{r},t)$. Focusing on the lower polariton branch, this leads to the so-called *driven-dissipative Gross-Pitaevskii equation*:

$$i\hbar \frac{\partial}{\partial t} \psi_{LP}(\mathbf{r},t) = \left[\hbar\omega_{LP}^0 - \frac{\hbar^2}{2m_{LP}} \nabla_{\mathbf{r}}^2 + V_{LP}(\mathbf{r}) + \hbar g n(\mathbf{r},t) - i\hbar \frac{\gamma_{LP}}{2} \right] \psi_{LP}(\mathbf{r},t) + \hbar \eta_{LP} F_p(\mathbf{r},t). \quad (1.76)$$

where V_{LP} is the external potential experienced by the polaritons which depend on those felt by photons and excitons through the Hopfield coefficients $V_{LP}(\mathbf{r}) = C_{\mathbf{k}}^2 V_{\gamma} + X_{\mathbf{k}}^2 V_X$, \mathbf{k} being here the pump wavevector. The term $\hbar\omega_{LP}^0$ is the polaritons energy at zero wavevector while the $\hbar^2 \nabla_{\mathbf{r}}^2 / 2m_{LP}$ is again the kinetic energy. Finally, the prefactor η_{LP} account for the coupling efficiency of the pump photons whithin the system. Since the presence of a fluid in the sample change the optical resonance through non linear interaction this term is generally not constant. However, in first approximation it is linked the reflectivity of the sample front mirror and can be considered as a constant. A full derivation of this equation as well as a complete discussion on its validity can be found in [\[2\]](#).

Dark reservoir. Along our description of excitons we mentionned the presence of dark excitons that are not directly coupled to light because of spin selection rules. As a consequence, one could think that they are not involved in the polariton dynamics. It is actually not the case. Indeed, eventhough they do not interact with photons they can still interact with bright excitons through the many complex electron-hole interactions described in [subsection 1.2.7](#). Forgetting them in the description of the polariton dynamics would then be a mistake [\[25; 36\]](#). To derive a single master equation starting from the many microscopic interactions between photons, dark and bright excitons would require a full spin resolved description and is beyond the scope of this manuscript. Nevertheless, we will account for their presence phenomenologically by considering them as a reservoir of density n_r coupled to polaritons through a relaxation term γ_r . In terms of equations it reads as :

$$i\hbar \frac{\partial}{\partial t} \psi_{LP}(\mathbf{r},t) = \left[\hbar\omega_{LP}^0 - \frac{\hbar^2}{2m_{LP}} \nabla_{\mathbf{r}}^2 + V_{LP}(\mathbf{r}) + \hbar g n(\mathbf{r},t) + \hbar g_r n_r(\mathbf{r},t) - i\hbar \frac{\gamma_{LP} + \gamma_{in}}{2} \right] \psi_{LP}(\mathbf{r},t) + \hbar \eta_{LP} F_p(\mathbf{r},t), \quad (1.77)$$

$$\frac{\partial}{\partial t} n_r = -\gamma_r n_r + \gamma_{in} n. \quad (1.78)$$

As it will be shown in the following the presence of a dark reservoir is of great importance when it comes to describing the quantum fluctuations of the polariton fluid.

1.4.3 Excitation scheme

So far, the derivation of the master equation was initiated by stating that a polaritonic state could be macroscopically populated through optical pumping. However, the pump term was not yet defined in the sense that we did not specify the frequency of the pump photons with respect to the polariton dispersion relation. The latter is crucial to determine what are the mechanism leading to long range coherence.

1.4.3.1 Off resonance excitation

In the case off resonant case the pump laser is highly blue detuned with respect to the polariton energy, close to a reflectivity minimum above the stop band of the DBRs (see [Figure 1.2](#)). The rise of a macroscopic population then occurs in the bottom of the LP branch through polaritons relaxation. More precisely, the injected photons create highly excited electron-hole pairs that relax through the emission of phonons. Lowering their energy they can emit photons and, at some point, eventually strongly couple to them to form polaritons. At this stage the polaritons are incoherent since the coherence of the pump laser got lost in the many relaxation processes. Then, the incoherent polariton undergo scatterings and relax toward the minimum energy states available. If the pump intensity is increased, the population in the minimum of the LP branch will "accelerate" the relaxation of the other polaritons through bosonic stimulations. If the stimulation is efficient enough with respect to the losses, the bottom of the LP branch gets macroscopically populated and obtain a long range order which can be seen on [Figure 1.11](#). Just like in atomic systems, the phase of the condensate wave function is chosen randomly through $U(1)$ symmetry breaking and is not inherited from the pump laser. Such a phase transition in polariton planar microcavity was first observed in 2006 by Kasprzak et al. [18].

Some major differences with atomic BECs are worth mentioning. First, the temporal phase of an atomic BEC is defined by the chemical potential and is related to the number of atoms in the system while the polaritonic system can never reach equilibrium. Its temporal phase result from a complex interplay between the pump laser and the losses of the system : the phase transition is driven by the pump intensity rather than the temperature. transverse

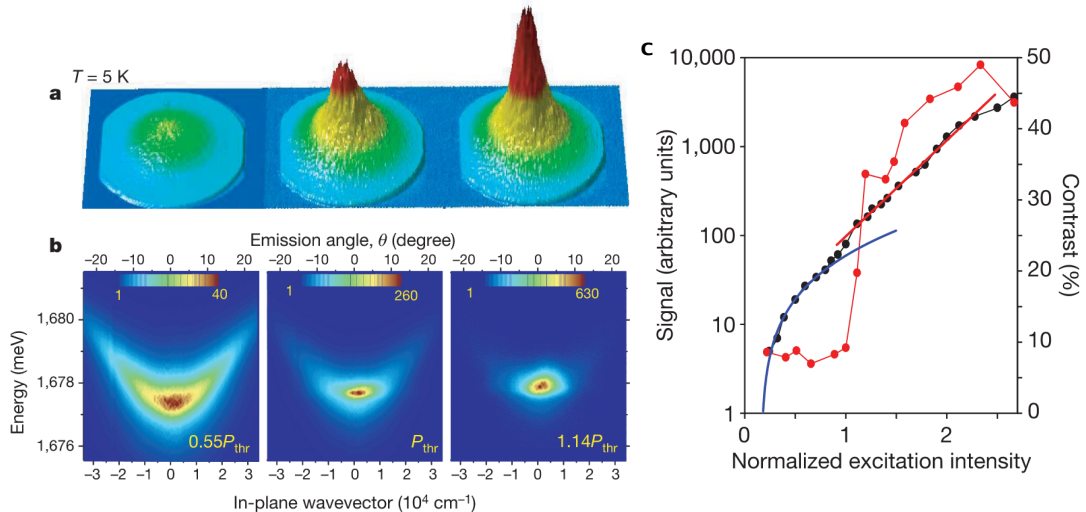


Fig. 1.11 Bose-Einstein condensation of polaritons. **a)** Far field emission of the fluid for increasing pump intensity. Above threshold, a strong emission in the zero wavevector mode is observed. **b)** Polariton dispersion for increasing pump intensities. Above threshold the bottom of the LP branch is macroscopically populated. **c)** Spatial correlation measurements using a Michelson interferometer. Solid red circles indicate correlations between two spots separated by 6mm (2.5 times the thermal de Broglie wavelength) within the condensate as a function of the excitation power. The correlation exhibits a threshold-like behaviour. The variation of the ground-state emission intensity, normalized to the excitation power, is shown for comparison (solid black circles). The solid blue line is a quadratic fit of the data demonstrating the occurrence of particle-particle interaction below threshold. Above threshold, the solid red line is an exponential fit demonstrating the strong stimulation of the relaxation by the high occupancy factor of the ground state. Adapted from [18].

1.4.3.2 Resonant excitation.

In the resonant case, the pump laser is tuned near the polariton energy. The population of the polaritons is then directly driven by the pump laser. In particular due to momentum and energy conservation, the spatial and temporal coherence of the pump laser are transferred to the polaritons fluid. In that case the phase of the fluid is fixed by the pump and therefore is not randomly chosen. In this excitation scheme the fluid should then not be called a condensate. However, it can still exhibit superfluidity and other quantum fluid properties because it possesses the required properties, namely : a macroscopic occupation of a single quantum state, long range coherence and weak interactions. In this work we will only use the resonant scheme to take advantage of the tunability of the pump to create fluid with arbitrary densities and velocity profiles. Before detailing the great versatility of this system, let us first discuss a consequence of the resonant excitation scheme which will be of great interest in the following.

Optical bistability. Consider a Fabry-Perot cavity filled with a non-linear Kerr medium,

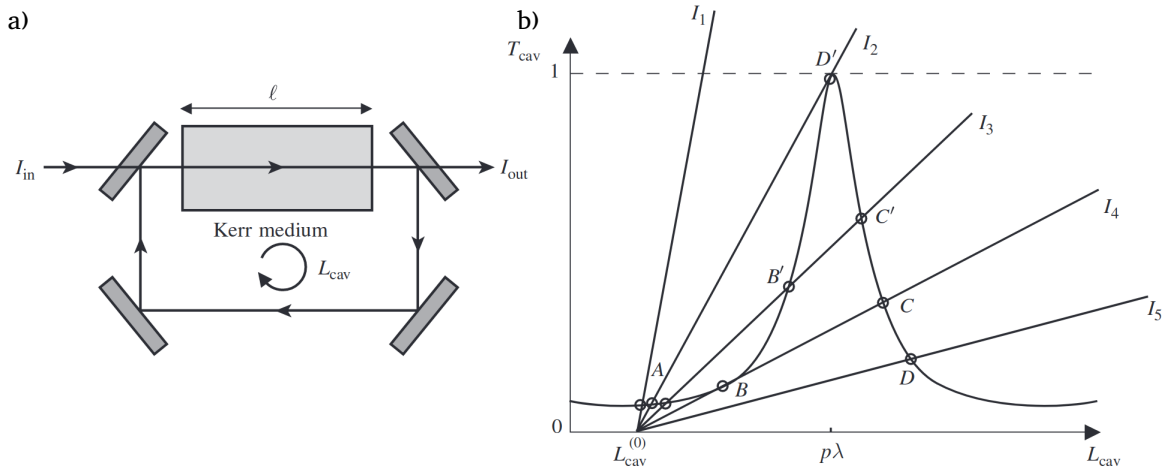


Fig. 1.12 **Optical bistability.** a) Schematic of a ring cavity filled with a Kerr medium. The cavity has a length $L_{cav}^{(0)}$ and the Kerr medium a length ℓ . b) Transmission of the cavity as a function of the optical length of the cavity L_{cav} . The straight lines represent the values T_{cav} as a function of L_{cav} for different values of I_{in} . The operating points lie at the intersections of the cavity resonance curve and the straight lines. Depending on I_{in} one or three operating point can be found. Adapted from [13].

through which a weak resonant laser beam is shone. As the laser intensity is low, the refractive index within the cavity is the same as the bare medium. It means that the optical length of the cavity is an integer multiple of half the laser wavelength. If the laser intensity is increased, the non-linear Kerr effect turns on and the refractive index of the medium increases. The laser is then no longer resonant with the cavity which reduce the intensity of the intracavity field and counteract on the refractive index. This interplay between non-linearities and resonance conditions is at the heart of what is called optical bistability. Since this phenomenon is not proper to polaritonic system, we will, to understand it more in details, follow the very general derivation done in [13].

To avoid first complications due to cross Kerr effect we consider a ring cavity of geometrical length L filled with Kerr medium of length ℓ as shown in Figure 1.12 a). The optical length of such a cavity is :

$$L_{cav} = L + (n_0 - 1)\ell + n_2 I_{cav} \ell, \quad (1.79)$$

where n_0 is the refractive index of the medium, n_2 the non linear refractive index and I_{cav} the intracavity intensity. As explained for a planar cavity in section 1.1, the cavity has transmission peaks whenever the optical path of a round trip in the cavity (a photon going back and forth) is an integer multiple of the laser wavelength λ . In the case of a ring cavity this condition reads :

$$T_{cav} = \frac{1}{1 + \frac{4F^2}{\pi^2} \sin^2 \left(\frac{kL_{cav}}{2} \right)}, \quad (1.80)$$

where F is the cavity finesse and $k = 2\pi/\lambda$ the wavevector of the laser. The transmission of the cavity as a function of L_{cav} is plotted in [Figure 1.12 b](#)). On the other hand the transmission of the cavity is defined as :

$$T_{cav} = \frac{I_{out}}{I_{in}} = T \frac{I_{cav}}{I_{in}} = \frac{T}{n_2 l} \frac{L_{cav} - L_{cav}^{(0)}}{I_{in}}, \quad (1.81)$$

where T is the transmission of the outport mirror and $L_{cav}^{(0)}$ the optical length of the cavity at low intensity $I_{cav} \approx 0$. An operating point is then defined as the intersection of the transmission curve [Equation 1.80](#) and the straight line of [Equation 1.81](#). Graphically the slope of the linear relation between T_{cav} and L_{cav} depend on the value of I_{in} . As a consequence several regime are possible depending on the value of the input intensity as shown in [Figure 1.12 b](#)). For low intensity as I_1 , the operating point is unique and the system is in a stable regime but yields a low transmission. For higher input intensity like I_3 , the system exhibits three operating points. However, it can be shown that the intersection points with a negative derivative between B and D are unstable. At even higher intensity the system has again a single operating point and a poor transmission. When the input intensity lies between I_2 and I_4 the system is said to be in a bistable regime.

In the case of microcavity-polariton the same behavior can be observed as the exciton-exciton non-linear interactions are of the same nature as the Kerr effect. Analytically, polariton bistability can be found by looking at the steady state of the driven-dissipative Gross-Pitaevskii equation in the presence of a driving pump term nearly resonant with the LP branch. In first approximation, it can be written as a plane wave $F_p(\mathbf{r}, t) = F_p e^{i\mathbf{k}_p \cdot \mathbf{r} - i\omega_p t}$. As it is usually done for equations including a resonant forcing term, we look for solution of the same form namely, plane wave with the same phase, $\psi(\mathbf{r}, t) = \psi^0 e^{i\mathbf{k}_p \cdot \mathbf{r} - i\omega_p t}$. Inserting this ansatz into [Equation 1.76](#) in the absence of external potential $V_{LP} = 0$ and setting the time derivative to zero one obtain the steady state equation :

$$\left[\omega_p - \omega_{LP} - \frac{\hbar k_p^2}{2m_{LP}} - g |\psi_{LP}^0|^2 + i \frac{\gamma_{LP}}{2} \right] \psi_{LP}^0 = \eta_{LP} F_p^0. \quad (1.82)$$

It is the equivalent of the equation of state of a conservative system with the difference that, in this case, it results of a complex equilibrium between interactions, pumping and losses. Notice that the contribution of the dark reservoir was neglected as the goal of this section is to understand in a general way bistability in polariton microcavity. Nonetheless, it actually has remarkable consequences on the hysteresis cycle and the later can be used to probe polariton-dark excitons interactions with optical means, notably through two photon excitation to overcome spin forbidden transitions [\[34\]](#)

To end up with an equation linking the pump intensity to the polariton density one can multiply this equation by its complex conjugate which gives :

$$n \left[\frac{\gamma_{LP}^2}{4} + (\delta(k_p) - gn)^2 \right] = \eta_{LP}^2 I, \quad (1.83)$$

where $\delta(k_p)$ is the effective detuning between the pump laser and the LP branch at the pump wavevector in a parabolic approximation, $\delta(k_p) = \omega_p - \omega_{LP} - \hbar k_p^2 / 2m_{LP}$ and I the pump intensity. Being a polynomial of degree 3 in the polariton density, this equation have up to three solutions. Three distinct real solutions can be found only if $\delta > \sqrt{3/2}\gamma_{LP}$, as explained in the previous paragraph, one of this solution is known to be unstable. However, in some peculiar cases, namely when the fluid dimension is ramped down from 2D to 1D this solution can be explored and is responsible for the emergence of first order phase transition as investigated in [21]. This being said, we don't take into account this solution in the present work since the dimension of the fluid will always be 2D. The evolution of n as a function of I in this regime is plotted in [Figure 1.13](#). The system is in a bistable regime when the curve exhibits two stable solutions for a given intensity : one at low density and one at high density. It's worth noticing that the actual state in which the system is depend on its past history. More precisely, if the incident intensity is initially low, since the laser is blue detuned with the polariton energy, the photon injection whithin the sample is poor and a few polariton are created. However, their presence in the cavity tends to blueshift their own resonance energy as explained in [subsection 1.3.1](#). As the intensity is ramped up, the system will follow the low density branch until the energy renormalisation is sufficient to reach the point B. At this point the system is compelled to jump to the high density branch and will suddenly move from point B to point C. If the pump intensity is then decreased, the situation is rather different since many polaritons are already present in the sample and support the laser injection and thus polariton creation. The system will follow the high density branch untill it reaches the point D' where interactions can no longer compensate for the losses making it fall again on the low density branch. A particular attention must be given to this so called turning point D'. Indeed, as it can be seen on [Figure 1.12](#) it's the only point at which the laser is exactly resonant with the cavity filled with non linearities. This point can only be reached by travelling on the whole hysteresis loop. The corresponding density can be determined by solving $\frac{dI}{dn} = 0$ which gives the discriminants :

$$\Delta = g^2 \left(\delta^2 - \frac{3\gamma_{LP}^2}{2} \right). \quad (1.84)$$

The bistable regime require two distinct solution for $\frac{dI}{dn} = 0$ which require $\Delta > 0$ and provide the afromentionned condition $\delta > \sqrt{3/2}\gamma_{LP}$. From this one can find that the density corresponding to the turning point fullfill $\delta(k_p) = gn$.

Conversely, when the detunig is two small with respect to the system losses the system is monostable and said to be in the optical limiter regime. In the bistable regime, the system exhibits

All optical control. In the context of analog gravity, the ability to easily control and monitor the fluid of light is a great asset. Indeed, the study of Hawking radiation in a quantum fluid require the creation of an acoustic horizon as well as the possibility to measure what is emitted by the latter. In particular, it is crucial to achieve two goals.

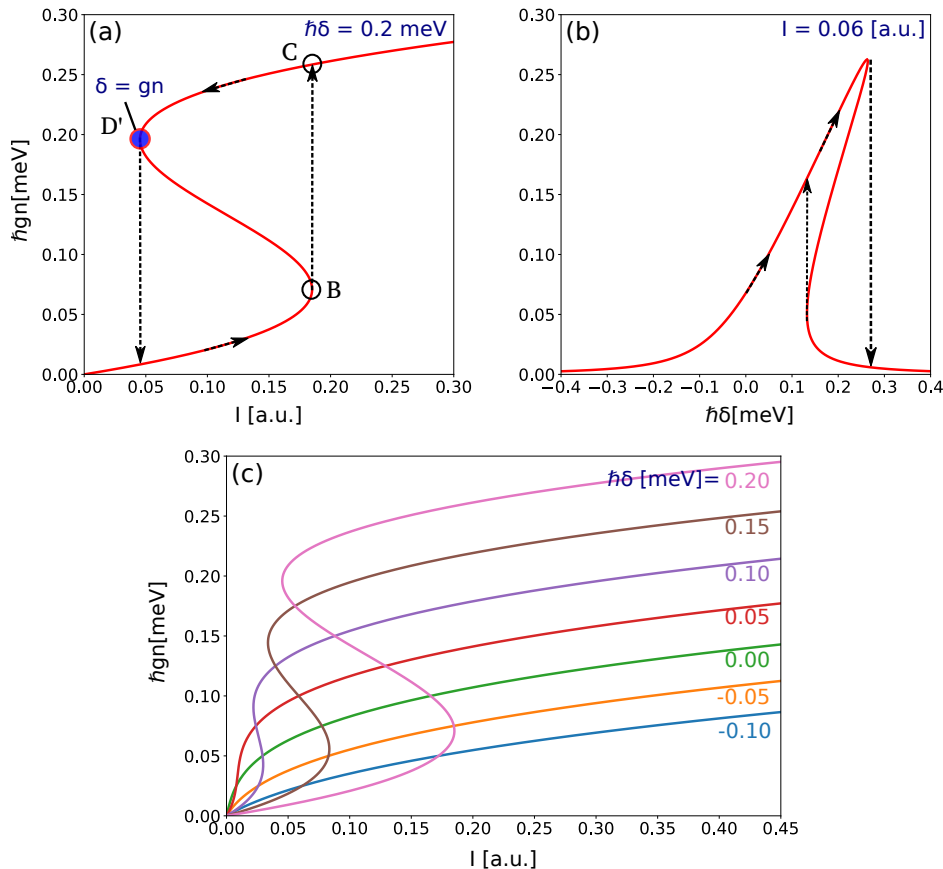


Fig. 1.13 **Optical bistability in a polariton fluid.** a) The polariton density as a function of the pump intensity when $\delta > \frac{\sqrt{3}\gamma_{LP}}{2}$. The blue point represent the so called turning point at which the detuning is exactly equal to the interaction energy. b) Polariton density as a function of δ for a fixed pump intensity. c) Polariton density as a function of the pump intensity for different values of δ , bistability is observed when $\delta > \frac{\sqrt{3}\gamma_{LP}}{2}$.

- 1. Create and monitor a stable fluid with an arbitrary flow profile and density since the mean field and especially its velocity profile are the analog of the curved spacetime we want to study.
- 2. Probe the fluid collective excitations. These small perturbations on top of the mean field are the fluid counterpart of the quantum fields fluctuations considered in the Hawking radiation theory.

With planar microcavity polaritons this is done fully optically since the fluid is created by the pump laser and is monitored by collecting the photons leaving the sample. The first point is allowed by the resonant excitation scheme. The velocity of a polariton being $\mathbf{v}_{LP} = \frac{\hbar\mathbf{k}_{LP}}{m_{LP}}$ momentum conservation enable to create a fluid with a given velocity by just changing the pump incidence angle (see [section 1.1](#)). This correspondance also holds for the light outgoing the sample : the recombination of a polariton with wavevector \mathbf{k} produce a photon with the same wavevector. Although the relation between the pump intensity and the polariton density is not trivial as we shall see in the next section, it is also a practical control knob that can be used to tune the fluid speed of sound. The second point can again be tackled with optics means since the struture of collective excitations is ultimately hidden in the fluctuations of the photonic field outgoing the sample. As a consequence, the large variety of tools and methods developped in the field of optics can be used to probe the fluid. Microcavity polaritons, are lying at the crossroad of optics and quantum fluids, definitely justifying the designation "quantum fluid of light".

Chapter 2

Optical generation and spectroscopy of arbitrary acoustic horizons

The study of particle creation in the presence of highly curved spacetime has been a subject of interest for many years. The most famous example is the Hawking radiation [14], which predicts the creation of particles from the vacuum in the vicinity of a black hole event horizon enabling the black hole to evaporate. The obvious difficulty to test this prediction experimentally is double. First, the blackness of such an object makes it hard to spot with a telescope meaning one have to rely rather on the peculiar behavior of visible object moving in the gravitational field of such a supermassive object. The optical observation of a black hole took almost one century since the first prediction of gravitational collapse by Subrahmanyan Chandrasekhar in 1920. It required the synchronization of nine telescope across the world to obtain an optical system whose optical aperture is the size the diameter of earth. the black body temperature of

As mentionned in the previous chapter, the creation of a sonic horizon in a polariton fluid can lead to spontaneous emission of bogoliubov modes provided the downstream region collective excitation spectrum exhibits negative energy modes. Furthermore, it was shown that the strength of the emitted signal depends strongly on the curvature of the horizon, or in other words, its steepness. To ensure that such effect is in principle observable in the lab, one need to fully characterize the mean field of the fluid as well as locally probe its excitation spectrum. This chapter is dedicated to the description of the fully optical generation of arbitrary transonic fluids as well as the characterization of the excitation spectrum on both side of the horizon. The latter revealed the first measurement of negative energy modes in a supersonic quantum fluid, validating the possibility to observe particle creation in a polariton fluid.

The first part will focus on the generation of mean fields with arbitrary velocity profile through the shaping of the pump laser phase. In a second part, we will present the pump probe spectroscopy method used to locally measure the collective excitation spectrum as well as the results obtained on several transonic fluids. The results obtained are reported in Ref ??

2.1 Optical generation of arbitrary fluid velocity field

Let us set the coordinates x and y to describe the microcavity plane. As explained in Chapter 2, translationnal invariance in the xy -plane ensure in plane momentum conservation along photon absorption, while the wavevectors along the z direction are fixed by the cavity and quantum well lengths. Furthermore, in this experiment the laser beam is set to be quasi resonant with the lower polariton branch. As a consequence, the transverse phase of the laser is directly imprinted on the polariton field. Indeed, in the low wavevector limit, the lower polariton branch can be safely approximated by a parabola, namely :

$$\omega_{LP}(\mathbf{k}) = \omega_{LP}^0 + \frac{\hbar k^2}{2m_{LP}}. \quad (2.1)$$

The group velocity of a polariton is then $\mathbf{v} = \frac{\partial \omega_{LP}}{\partial \mathbf{k}} = \frac{\hbar \mathbf{k}}{m_{LP}} = \frac{\hbar \mathbf{k}_p}{m_{LP}}$ where k_p is the in-plane wavevector of the pump laser. In the case of a plane wave $k_p = \vec{\nabla}\theta(\mathbf{r})$ where $\theta(r)$ is the spatial phase. This can safely be generalized to more complex spatial phase profile, which provide a direct link between the driving laser phase and the velocity of the fluid :

$$\mathbf{v} = \frac{\hbar \vec{\nabla}\theta(\mathbf{r})}{m_{LP}}. \quad (2.2)$$

2.1.1 Waterfall configuration

A first realisation of a 1D acoustic black hole in a polaritonic system was done in [28] with the so called waterfall configuration. The setup was composed of a microcavity etched to be truly one dimensionnal and a defect was added in the middle of the wire to act as an external attractive potential and force the polariton flow to accelerate. The pump was only shone in the region before the defect. The downstream region of the flow was then made of polariton that propagate ballistically and whose speed is fixed by the interaction energy in the upstream region. Eventhough this configuration provide a natural fluid acceleration, the horizon geometry depends greatly on the defect shape and can not be tuned easily. Furthermore, the collective excitation spectrum and the presence of negative energy modes was not investigated which prevent to conclude on the nature of the signal observed in the experiment. In the present work, we present a different approach to generate such flows with an effective 1D fluid fully optically created as well as a full characterization of the Bogoliubov spectrum.

2.1.2 Target velocity profile

Before analyzing whether the fluid surpasses a critical velocity, the primary objective is to generate a flow exhibiting two homogeneous regions separated by a sharp transition, each characterized by a well-defined velocity. For clarity, the region preceding the transition will be referred to as the upstream region, with velocity v_{up} while the region following the transition will be designated as the downstream region, with velocity v_d . To model this configuration, a

target velocity profile is arbitrarily defined as follows:⁶

$$v(x) = \frac{v_d - v_{up}}{2} \tanh\left(\frac{x - x_h}{w_h}\right) + \frac{v_{up} + v_d}{2} \quad (2.3)$$

where x_h and w_h are the position and width of the transition respectively. This profile is represented in Figure 2.1 a). One can then verify that :

$$\lim_{x-x_h \ll -w_h} v(x) = v_{up}, \quad (2.4a)$$

$$\lim_{x-x_h \gg +w_h} v(x) = v_d. \quad (2.4b)$$

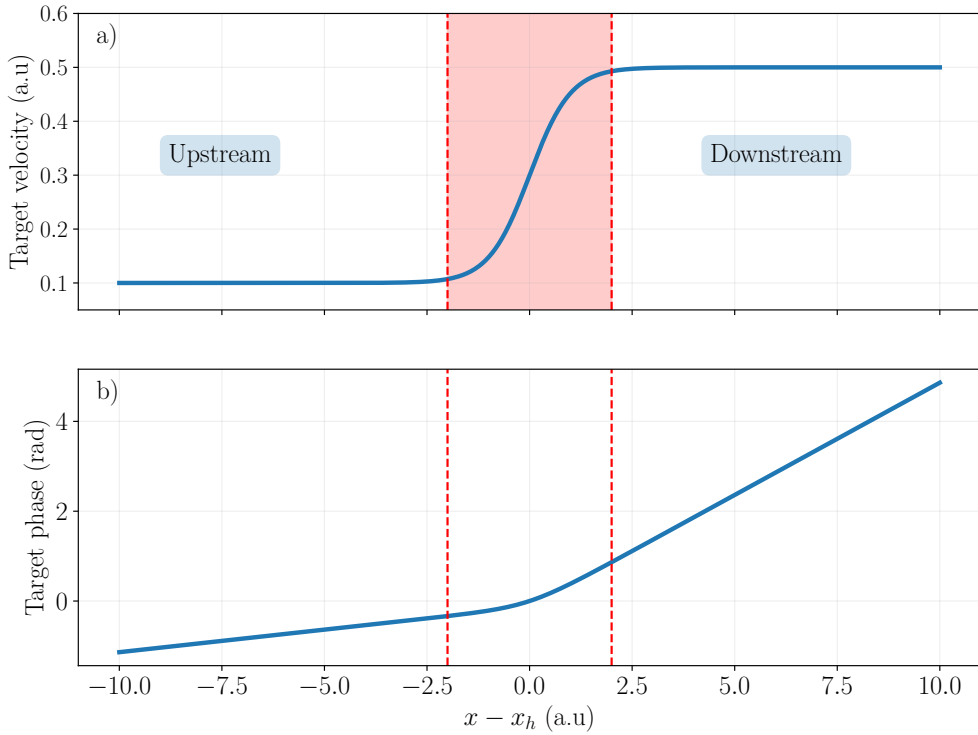


Fig. 2.1 a) Target velocity profile for input parameters $v_{up} = 0.1$, $v_d = 0.5$, $x_h = 0$ and $w_h = 1$ in arbitrary units. The red shaded area represent the transition region.
b) Corresponding phase profile to be imprinted on the pump laser.

Such a velocity profile show a great flexibility in the choice of the upstream and downstream velocities as well as the steepness and the position of the transition. From this, one can determine the phase that must be imprinted on the pump laser to generate such a flow profile by simple integration of Equation 2.3, which gives :

$$\phi(x) = \frac{m_{LP}}{\hbar} \int v(x) dx = \frac{m_{LP}}{\hbar} \left(\frac{v_d - v_{up}}{2} w_h \ln(\cosh\left(\frac{x - x_h}{w_h}\right)) + \frac{v_{up} + v_d}{2} x \right). \quad (2.5)$$

The latter is plotted in [Figure 2.1 b\)](#). The derivative of this curve at position x corresponds to the local wavevector of the pump laser, or equivalently, this curve provides a direct side view of the wavefront of the driving laser. Indeed, the wavefront is defined as the surface of constant phase of the beam. Notably, considering that the driving laser also possesses a wavevector along the z direction, determined by the resonance conditions, the isophase surfaces of the total laser phase θ_{laser} are given by:

$$\theta_{laser}(r) = k_z z + \phi(x) = cst \quad (2.6)$$

$$= \frac{2\pi n_{cav}}{\lambda_0} z + \theta(x) = cst, \quad (2.7)$$

which is inverted as $z \propto \phi(x)$. Making a fluid with the wanted velocity field then boils down to be able to imprint the phase [Equation 2.5](#) on the laser that resonantly excite the fluid. As we will see in the next section, this can be done with a Spatial Light Modulator (SLM).

A simplified scheme showing how printing the target wavefront in the sample plane create the desired flow. To verify that the fluid has the expected phase we use an usual off axis interferometry method whose principle is explained in [subsection A.1.2](#). As an example, the measured phase corresponding to the mean field displayed in [Figure 2.2 b\)](#) is shown in [Figure 2.3](#).

Controlling the local intensity. Being able to modify on demand the intensity of the pump laser along with the phase is also crucial since the polariton fluid density, and thus the regime of collective excitation, depends on the input intensity as explained in [??](#). Notably, if the system operates at the turning point of the bistability loop, it exhibits a linear collective excitation spectrum, and the speed of sound is directly linked to the detuning of the laser with respect to the lower polariton branch as $gn + g_r n_r = \delta(k_p)$. More generally, the possibility to move onto the higher branch of the bistability enables control over the gap opening in the Bogoliubov spectrum, transitioning from a linear spectrum to a masslike one. Once again, this can be achieved using the SLM by locally adjusting the height of the phase grating under the target phase profile, as explained in [subsection A.1.4](#). This adjustment reduces the number of photons directed into the first diffracted order. This method is widely employed to create top-hat intensity profiles and is of significant interest in metrology and cold-atom experiments to minimize systematic effects [\[26\]](#).

To summarize, it is possible to generate and monitor fluid with arbitrary density and velocity flow by shaping the pump laser both in phase and intensity. We hence have a full optical way to create effective space time on which we can study the propagation of collective excitation near the transition region.

2.1.3 Effective 1D fluid

So far, the description of the fluid both in velocity and density was one dimensionnal despite the fluid is actually a 2D system. This assumption rely on the fact that the fluid wavefunction is invariant under translation in the y direction in a given region of interest represented by the white dashed rectangle of [Figure 2.3](#). This area is approximatively $130\mu m$ long and

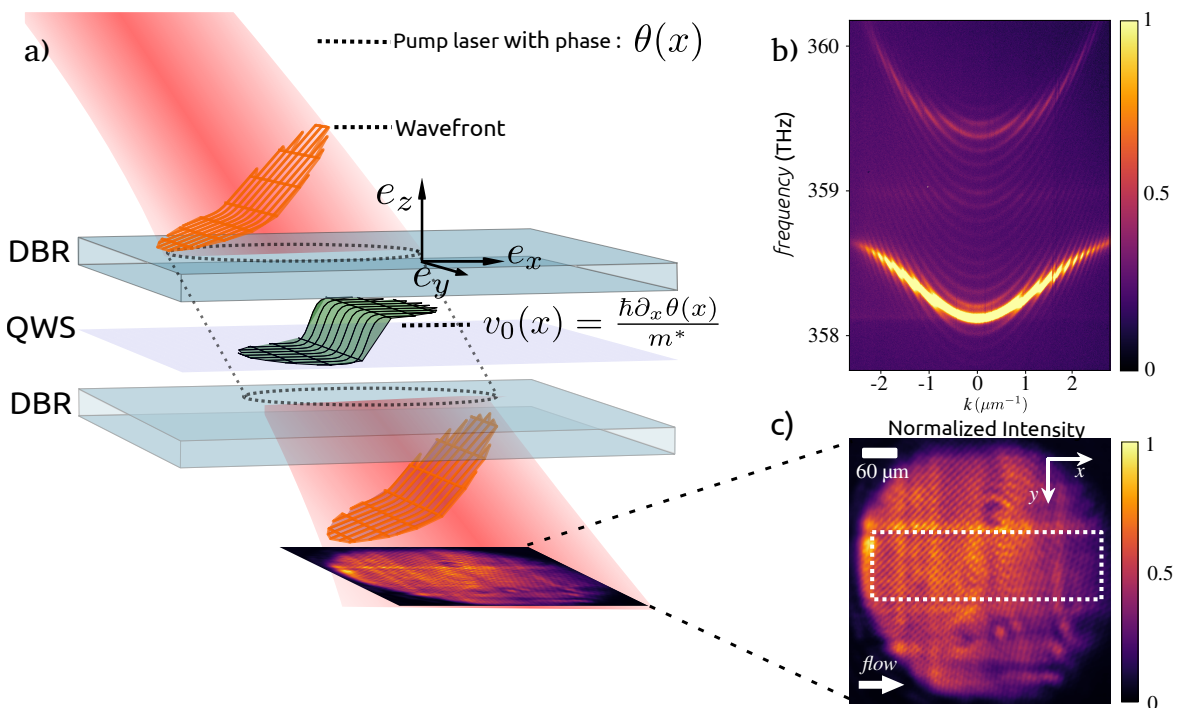


Fig. 2.2 Simplified scheme of the generation of a transonic fluid. a) The pump laser is shaped with the target phase profile and sent on the microcavity. The corresponding fluid velocity field is represented by the black surface lying on the Quantum Wells (QWs). c) The outgoing photons are collected and the sample plane is imaged on a CCD camera to obtain the fluid density map. b) Measured Lower and Upper polariton dispersion at the working point C6 – D6 at which the experiment was run. By fitting this dispersions, the effective LP mass can be extracted $m_{LP} = 7.0 \times 10^{-35} \text{ kg}$

$30 - 40\mu m$ large. A cut of both the phase and density in the direction orthogonal to the propagation are shown in Figure 2.3 b) and c). Periodic modulations are present because of back reflection on the protection screen of the camera sensor and are present even without passing through the sample. These modulation can be removed upon fourier filtering which allow to compute the variation of the phase with respect to 2π , $\sigma_y^{ph}/2\pi = 0.3\%$ as well as the relative intensity variation $\sigma_y^I/\langle I \rangle = 3\%$. As a consequence, we can safely assume that the fluid is effectively 1D in the region of interest. This contrasts with the work [28] previously mentionned. In the present configuration, the shape of the horizon is fixed by the phase of the exciting laser and can be tuned as will which is crucial to study the effect of the horizon steepness on the emitted signals. Moreover, the presence of the pump laser in the downstream region brings a double advantage. First, the velocity of the fluid can be changed and doesn't depend on the interaction energy of the upstream region, allowing to study many fluid configurations. Secondly, this experiment doesn't suffer from the exponential density decay that come with ballistic propagation [35]. As a consequence, it is possible to probe the collective excitation spectrum in any region of the fluid with a high resolution pump probe spectroscopy method that we will describe in the next section. This method depends on the response of the system to a weak perturbation. It is hence somehow proportionnal to the interaction energy of the fluid gn and better suited to pumped fluid [4].

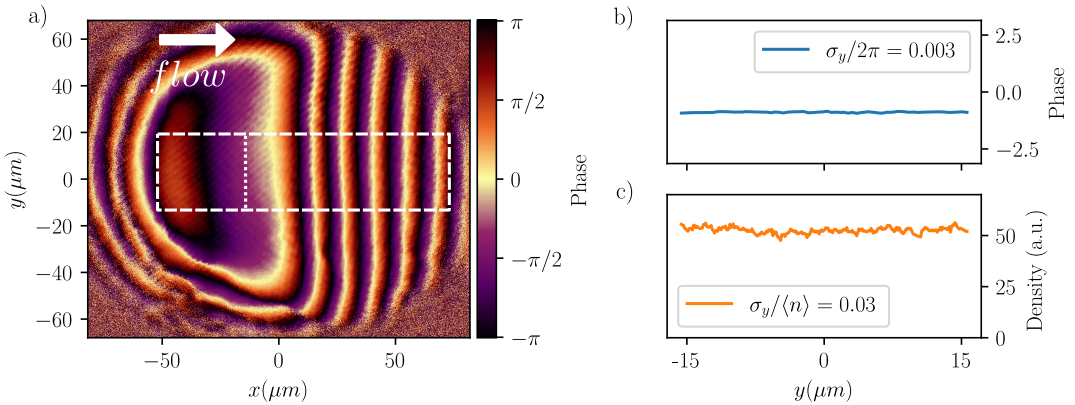


Fig. 2.3 a) Measured phase of the mean field shown in Figure 2.2. The curvature present in the upstream region is due to the non linear self focusing. The region on interest in which we assume translationnal invariance is represented by the white dashed rectangle. b) Cut of the phase in the y direction represented by the dotted white line in the rectangle. The variation to the phase with respect to 2π are equal to 0.3% . c) Cut of the intensity of the mean field in the y direction at the same location than b). The corresponding relative intensity variation is equal to 0.3% .

2.2 Experimental spectroscopy of the collective excitation spectrum

The analog of the Hawking radiation in a polariton fluid is the spontaneous emission of Bogoliubov modes from the horizon. When the system is operating at the turning point

of the bistability the Bogoliubov spectrum is gapless and linear which enable to define a speed of sound $c_s = \sqrt{\hbar g n / m_{LP}}$ and speak without ambiguity of sonic excitation in the low wavevector limit. In this regime, the condition to observe negative energy modes coincide with the fluid being supersonic as explained in the previous chapter. However, creating a stable fluid at the turning point is quite challenging and the measurement of the spectrum linearity require experimental techniques that are hard to implement on a moving fluid [5]. Nevertheless, linearity is not mandatory to observe Hawking radiation since it only requires the mixing between positive and negative energy modes which can be achieved without operating at the turning point. Besides, a gap opening in the Bogoliubov brings new physics on the table since it widen the study of quasi-particles creation to the case of massive particles. In this section we discard the necessity to have sonic excitations and measure the presence of negative energy modes in a wide range of fluid configuration exploring different asymptotic velocities and horizon steepness.

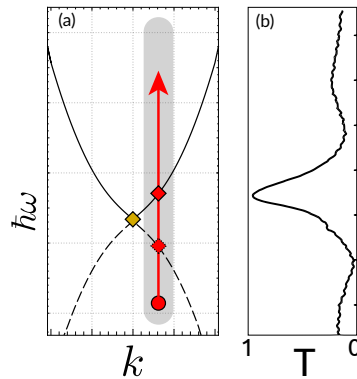


Fig. 2.4 Simplified scheme of the pump probe spectroscopy method. a) At a given in plane wavevector represented by the red arrow, the probe frequency is scanned around the mean field frequency and is transmitted when it resonate with the bogoliubov branch. b) Typical transmission spectrum of the probe at the wevevector of a).

2.2.1 High resolution pump-probe spectroscopy method

The measurement of the collective excitation spectrum consists in scanning the mean field resonance by looking at the transmission of a weak probe laser at the different incidence angles. First, polariton fluid is created with a driving laser as described in the previous section. A probe laser is then sent on the sample with a well defined incidence corresponding to an in plane wavevector as explained in [section 1.1](#). The frequency of the probe is then scanned around the mean field frequency. When the perturbation frequency matchs these of the collective excitation, the probe create perturbations in the fluid with same energy and wavevector that ultimately escape the sample as photons. Frequency scans are then repeated for different incidence angles providing each time a transmission spectrum of the probe as shown in [Figure 2.4](#). To make sure that we stay in the weak perturbation regime the intensity of the probe is set two order of magnitude below the pump. To collect only the signal emitted in the perturbation mode, a tunable pinhole is placed in the Fourier plane of the collection path and track the probe in-plane wavevector position to filter out the

unwanted photons. Finally, the probe intensity is modulated at f_{mod} in order to isolate its transmission from the very strong signal of the pump. The remaining light is then sent on a photodiode connected to a Spectrum analyzer that demodulates the signal at f_{mod} to obtain the transmission spectrum. At the end, all the scans are put together to reconstruct the full collective excitation spectrum as typically shown in Figure 2.6.

2.3 Experimental setup

The setup used in this experiment is shown in ???. The sample is a microcavity consisting of three InGaAs quantum wells sandwiched between two highly reflecting planar GaAs-AlGaAs Bragg mirrors. The quantum wells, separated by GaAs barriers, are located at the three antinodes of the cavity, which has a finesse on the order of 3000. A complete map of this sample can be found at the end of this manuscript in ?? along with exciton-photon detuning measurements. This map enable to perform an experiment over several days at the same working point and overcome the problem due to daily cooling and warming procedures imposed by the open cycle cryostat. Furthermore, despite rigorous and exhaustive characterization of the sample, the quality of certain measurement can be substantially enhanced by looking phenomenologically the right working point fitted to the experiment. This being said, the experiment described in this chapter was run on the working point $C5 - D6$. The set up is divided in three main paths, the pump path, the probe path and the collection path.

- **The pump path** represented by the blue box is used to create the stationary states of the experiment. The polariton fluid is generated by a circularly polarized CW Ti:sapphire laser with a sub-MHz linewidth. This laser can be precisely frequency tuned around the LP resonance energy centered around 836 nm in our sample. An AOM together with a Proportional-integral-derivative feedback on the AOM driving RF are used to stabilize the laser intensity and make sure the experiment is constantly runned at a single fluid density. The stabilized Gaussian beam is reflected on the spatial light modulator (SLM) which imprints the target phase $\theta_p(x) = \int v_0(x)dx$ that determines the fluid velocity $v_0(x)$ at each point. The SLM plane is imaged in the plane of the cavity with two focal-length matched telescopes ($2f - 2f$ configuration).
- **The probe path** represented by the red box is used to measure the collective excitation spectrum. The probe is another tunable CW Ti:sapphire laser with the same polarization than the pump beam. The probe is sent on the sample with a well defined incidence angle controlled by another SLM on which a tunable step blazed grating is imprinted. The frequency of the laser is scanned over 220 GHz around the mean field frequency and monitored by a high resolution wavemeter. An AOM and a Proportional-integral-derivative feedback are also used to both stabilize the intensity along the scan and apply a $f_{mod} = 5$ MHz intensity modulation.
- **The collection path** located after the sample is used to collect the signals emitted by the fluid. A microscope objective send the outgoing field on a 50:50 BS. One part is directed to an optical system to make the image both in real and momentum space of the field. For both lasers, a pick-up is made after their respective AOM to have a phase reference and perform off axis interferometry measurement. Another part is sent to the apparatus described in subsection 2.2.1 to measure the transmission spectrum of the probe. The

tunable pinhole is made with a DMD placed in the fourier plan of a lense that send only photons arriving at the position of the pinhole to the collection photodiode. Taken the relative size of the probe mode and the size of a pixel of the DMD, the resolution of the pinhole can go down to $\delta k = 0.0005 \mu\text{m}^{-1}$. The collection photodiode is then connected to a spectrum analyzer set in zero span at f_{mod} to demodulated the signal and obtain the transmission spectrum of the probe. On both path as set of $\lambda/4$, $\lambda/2$ and PBS to make polarization filtering of the signal.

Scan resonances analysis. The shapes of the probe transmission and reflection peaks are directly related to the real and imaginary parts of the energy $\hbar\omega_b$ of the Bogoliubov dispersion relation. If we consider plane wave like excitations

$$\psi_{LP}(t) \propto \exp(-i\omega_b t) = \exp(-i\Re(\omega_b)t) \cdot \exp(i\Im(\omega_b)t), \quad (2.8)$$

one easily verifies by taking its temporal Fourier transform that its spectral density has the following Lorentz-distribution law

$$I(\omega) = |\psi_{LP}(\omega)|^2 \propto \frac{1}{(\omega - \Re(\omega_b))^2 + \left(\frac{\Im(\omega_b)}{2}\right)^2}. \quad (2.9)$$

At each probe wavevector k_{pr} the tranmssion spectrum $I_{k_{pr}}(\omega)$ is fitted with a Lorentzian function to extract the real and imaginary parts of the bogoliubov energy $\omega_b(k_{pr})$

2.4 Experimental results

2.4.1 Homogeneous fluid

To begin with, we first study homogeneous fluids with non zero velocities to see the effect of the doppler shift on the collective excitation spectrum. In this section, the pump is a basic gaussian beam which creates fluid having a spatial extension of approximatively 150 μm . The input angle of the pump is controlled in the same way as the probe by printing a tunable step blazed grating on the SLM. In each measurement, the effective detuning $\delta(k_p) = \omega_p - \omega_{LP}^0 - \hbar k_p^2 / 2m_{LP}$ is high enough to be in the bistable regime and the input pump intensity is chosen so the system operate on the higher branch of the hysteresis curve quite far from the turning point. The probe is set to be two order of magnitude weaker than the pump whith the same spatial extension and polarization.

Direct normal branch measurement. We create a set of homogeneous fluid with increasing in plane wavevectors k_p while keeping the pump frequency constant. For each fluid, we use the pump probe spectroscopy method to measure the probe transmission spectrum as shown on [Figure 2.6](#). The DMD is programmed to display pinholes that track the wavevector of the probe laser along the scans. In this case the system measure the direct transmission of the probe. The first measurement a) is made with the pump laser turned off which means in the absence of interactions within the sample. The probe transmission then scan the bear cavity resonances and recover the parabolic shape at low wavevector of LP branch. From this

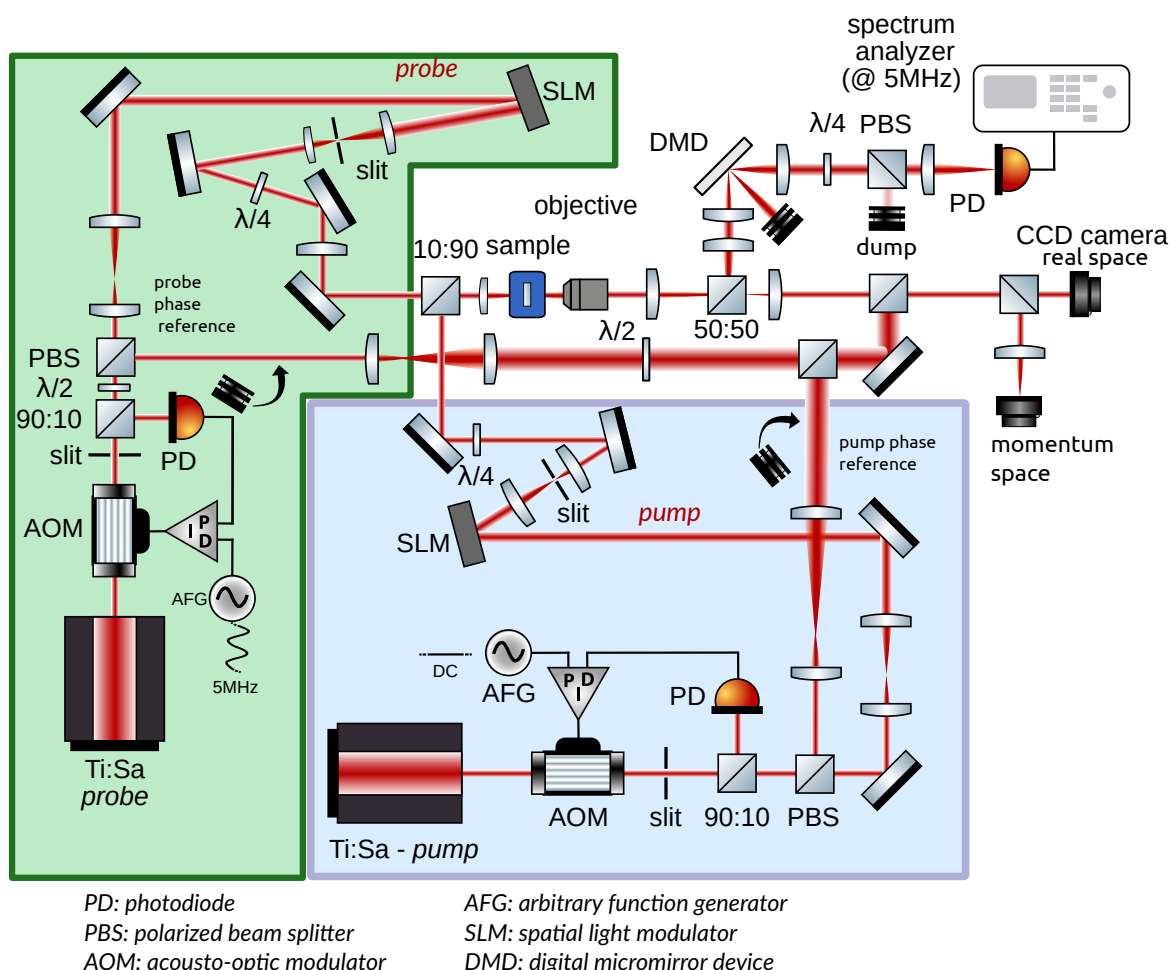


Fig. 2.5 Experimental setup

measurement we extract the detuning between the pump laser and the LP branch at zero wavevector $\delta(0) = 33\text{ GHz}$. The blueshift due to interaction lift the dispersion a) to higher energies whereas the doppler shift modifies the resonances according to $\omega' = \omega + \mathbf{v}_p \delta \mathbf{k}$ where \mathbf{v}_p is the fluid velocity $\mathbf{v}_p = \hbar \mathbf{k}_p / m_{LP}$. As the fluid velocity increases, the branch is bended and moved toward the pump wavevector. For $k_p \geq 0.3$ we already see some resonances lying under the pump energy. As explained in the previous chapter, the energy sign of a collective mode is given by :

$$\text{sign}(E) = \text{sign}(\omega_B) \times \text{sign}(Q_\phi), \quad (2.10)$$

where Q_ϕ is the norm of the mode defined in ?? and $\text{sign}(\omega_B)$ is taken with respect to the pump energy. Since the normal branch has a positive norm, the resonances located below the pump frequency are negative energy modes. As it can be seen, the ghost branch is not visible through direct excitation. This feature has a double origin : first the ghost branch is not optically resonant with the cavity which makes photon injection difficult at its energy. Secondly, the bogoliubov coefficient v_k of the negative norm branch is very small compared to u_k . In the presence of a coherent state like the probe, the populations then scale as $v_k^2 |\alpha|^2 \ll u_k^2 |\alpha|^2$ where α is the intracavity amplitude of the probe.

Ghost branch indirect measurement. To overcome the difficulty to directly excite the ghost branch, we take advantage of the strong linearities of the system to induce population through four wave mixing process. Indeed, because of the bosonic nature of bogoliubov excitations, occupation of the normal branch in the probe wavevector mode should stimulate the parametric conversion of two pump polaritons into a bogoliubov pair with opposite wavevectors and energies with respect to the pump, namely :

$$(k_p, k_p) \rightarrow (k_p + \Delta k, k_p - \Delta k), \quad (2.11a)$$

$$(\omega_p, \omega_p) \rightarrow (\omega_p + \Delta\omega, \omega_p - \Delta\omega). \quad (2.11b)$$

The emission in the ghost branch is then boosted by a factor $(u_k v_k)^2 |\alpha|^2$ [11]. In practice, this measurement can be done by changing the positions of the tunable pinhole so it track wavevector opposite to the probe with respect to the pump. More precisely, when a scan at $k_{pr} = k_p + \Delta k$ is made, the pinhole is set at $k_{pr} = k_p - \Delta k$ to collect the signal emitted in the conjugated mode.

Here we create again a homogeneous fluid with wavevector $k_p = 0.6\mu\text{m}^{-1}$. We then perform direct measurement of the normal branch and indirect measurement of the ghost branch. The results are shown in Figure 2.7 a) and b) respectively. The modulations on the right side of the direct measurement come from interferences in the substrat of the sample that act as a low factor Fabry Perot [5]. Each scan is normalized to its own maximum for the sake of clarity but the strength of the indirect signals is approximately 1 – 10% of the direct one. The noise present on several scan of b) corresponds to parasitic signals coming from other scatterings process that may send photons at the position of the pinhole and that, in the case of direct measurement, are negligible with respect to the resonance. The reason why the ghost branch doesn't appear as the symmetric of the normal branch is because the

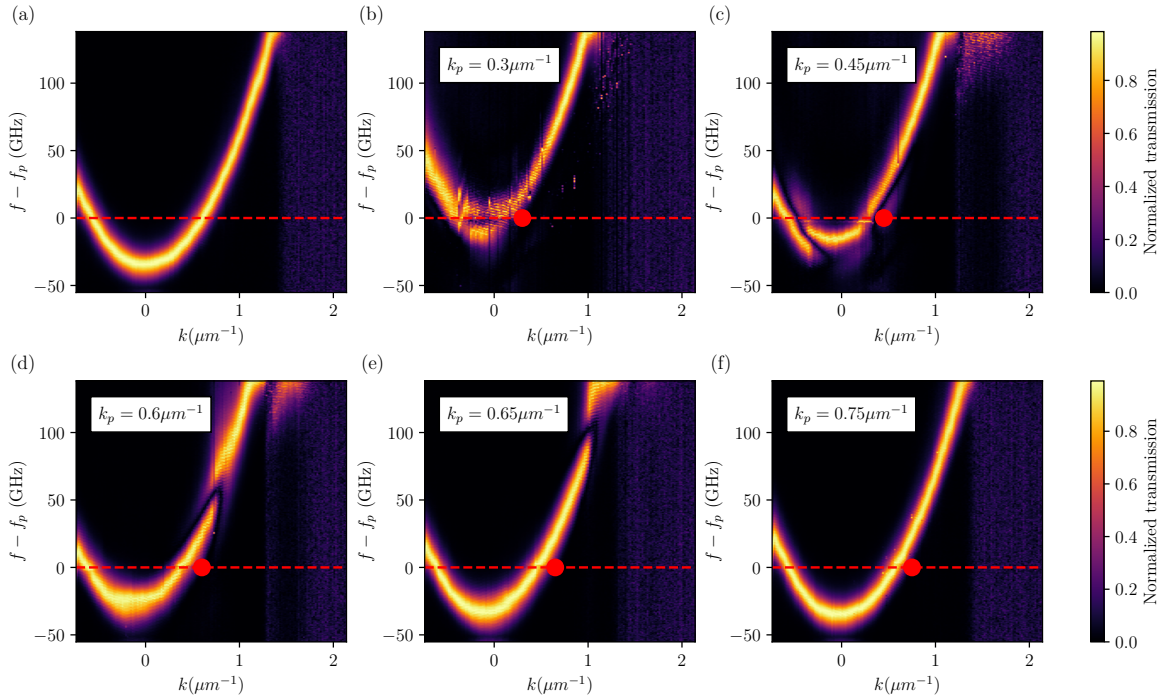


Fig. 2.6 a) Bear cavity dispersion measurement with the pump probe spectroscopy method in the absence of fluid. The parabolic shape of the Lower Polariton branch is recovered. The red dashed line represent the mean field frequency that was kept constant for all the measurements. From this we can measure the detuning between the pump laser and the LP branch at $k = 0$, $\delta(0) = 33$ GHz. b),c),d),e) and f) measured Bogoliubov normal branches for homogeneous fluid with velocities 0.75 , 0.98 , 1.23 , 1.29 and $1.43 \mu\text{m ps}^{-1}$ respectively, corresponding to the pump wavevector values in the inset of each figure.

axis k and $f - f_p$ represent the wavevector and frequency of the injected probe and not the emitted signal. However, the pinhole positions first ensure us that the signal is emitted in the opposite wavevector mode. To verify that it is also symmetric in frequency, we send the photons collected by the pinhole into a spectrometer to measure their energy. This two test enable to confirm that the signals taken through indirect measurement in b) indeed come from the ghost branch. As a consequence, it is possible to symmetrize the indirect data around the pump wavevector and energy to plot the full collective excitation spectrum shown in Figure 2.7 c). First, one can check that the two branches are indeed symmetric with respect to the pump represented by the red dot.

Once again this measurement is an additional proof that when the fluid velocity is high enough, negative energy modes can be excited on both positive and negative norm branches. It's worth noticing that no effort were put in this experiment to reach the turning point of the bistability loop which didn't prevent the observation of negative energy modes. This ease the experimental constraints to observe Hawking radiation in a polariton fluid and in fact widen the initial analogy that was made for sonic excitation in a supersonic fluid. More precisely it can be reformulated as follows : a fluid exhibiting a sharp transition between a region with

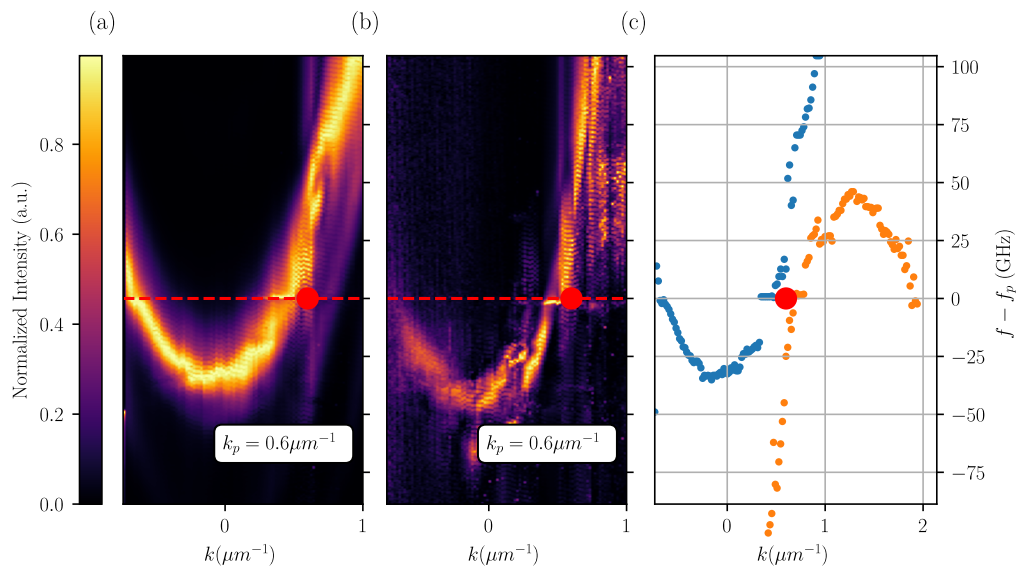


Fig. 2.7 **a)** Direct measurement of the normal branch of the Bogoliubov spectrum for a homogeneous fluid with in plane wavevector $k_p = 0.6 \mu m^{-1}$. **b)** Indirect measurement of the ghost branch of the Bogoliubov spectrum for the same fluid. **c)** Extracted resonance energy for each probe wavevector. The blue point are extracted from the direct measurement and correspond directly to the resonances of **a)**. The orange points are extracted from the indirect measurement. Each couple (k_{pr}, ω) extracted from b) is symmetrized around the pump position in phase space (k_p, ω_p) to account for 4wm process.

positive energy modes, and another with negative energy modes available, should experience correlated emission of Bogoliubov modes at the transition. These modes are not necessarily phonons and the velocity one has to exceed to observe them is not necessarily the speed of sound, but rather a critical velocity that depends more generally on the fluid parameters. Although this statement seems unclear with respect to the sonic version, it is actually more general and broaden the range of experimental configurations at which particle creation can be observed. In the following we will rather speak of trans critical flow and critical velocity instead of "sonic".

2.4.2 Smooth transition geometry

We first study a smooth transition between the sub- and supercritical flow regions. We implement the target velocity profile [Equation 2.3](#) with a transition width $w_H = 20 \mu\text{m}$. We study three profiles, with three values for the up- and downstream flow velocities v_u and v_d . All the measurements are made with $\delta(0) = 56 \text{ GHz} \rightarrow \hbar\delta(0) = 0.2 \text{ meV}$. At this detuning the system is in the bistable regime in both the upstream and downstream regions with a spatial extension of $120 \mu\text{m}$. For each configuration, the phase of the created fluid is measured by off-axis interferometry as described in [subsection A.1.2](#). By unwrapping the phase profile, as the one typically shown in [Figure 2.8 a\)](#), and taking the gradient in the x direction, we obtain the fluid velocity profile $v(x)$. The measured velocity profiles are represented by the solid lines in [Figure 2.8 b\)](#) showing three different asymptotic downstream velocities v_d with a single upstream velocity v_u . To selectively measure the upstream or downstream region the diameter of the probe beam is reduced to half the spatial extension of the fluid and the probe focused on the region of interest. The corresponding excitation spectra are shown in [Figure 2.8 c\)-f\)](#). The upstream region is shown in [Figure 2.8 c\)](#) and the downstream regions in [Figure 2.8 d\)-f\)](#).

2.4.2.1 Speed of sound measurement

Eventhough the system doesn't operate in a regime of sonic collective excitation we call $c_s = \sqrt{\hbar g n / m_{LP}}$ the speed of sound. The value of gn is extracted from the simultaneous fit of the normal and ghost branch of each spectrum with the bogoliubov dispersion relation :

$$\omega_b^\pm(\delta k) = -\frac{i\gamma}{2} + v_0(x)\delta k(x) \pm \sqrt{\left(\frac{\hbar\delta k(x)^2}{2m^*} - \delta(k_p) + 2gn(x) + g_r n_r\right)^2 - (gn(x))^2}, \quad (2.12)$$

with $\delta k(x) = k - k_p(x)$. The only unkown parameters in this equation are gn and $g_r n_r$. However by taking the steady states solution of the Gross Pitaevskii equation coupled to a reservoir [Equation 1.76](#) we obtain $n_r \propto n$. Based on the work [4; 5] made on the same sample and the assumption that the reservoir contribution depends on the exciton-photon detuning. We use the value $g_r n_r \approx 1.8gn$ of work [5] and end with a single free parameter gn to fit the spectra. The fit are represented by the colored dashed line in [Figure 2.8](#). The output of the fit gives in fact a value of $gn(r_{pr})$ where r_{pr} is the position of the probe. However, this value can

serve as calibration to reconstruct the full $gn(r)$ profile. Indeed we can safely assume that the output measured intensity is proportionnal to the fluid density as $I_{out}(r) = an(r)$ and that a is a constant that depend on the exciton photon detuning through the hopfield coefficients and complex cavity parameters. Nonetheless, given the spatial extension of the fluid with respect to the wedge of the sample $0.04 \text{ peV } \mu\text{m}^{-1}$, these paramateres can be considered as constant in the region of interest. We can then calibrate the speed of sound measurement through :

$$c_s(r) = \sqrt{\frac{I_{out}(r)}{I_{out}(r_{pr})}} c_s(r_{pr}). \quad (2.13)$$

The $c_s(x)$ map obtained for the different configurations are represented by the dashed lines in Figure 2.8 b). The speed of sound is found to be quite constant which yields a smooth transition between the upstream and downstream regions.

2.4.2.2 Critical velocity

In conservative fluids, sub- and supercritical flows are discriminated by the Mach number $M := v_0/c_s = 1$. Instead, in our driven-dissipative fluid, the minimum velocity to have a supercritical dispersion is larger than c_s . As a result, the condition $M = 1$, which defines the acoustic horizon in the hydrodynamic limit does not necessarily coincide with the condition to excite negative energy waves in the system. In other words the position at which the velocities exceed c_s in Figure 2.8 b) doesn't define the horizon of the fluid. Indeed, when the system doesn't operate at the turning point of the bistability we have $gn > \delta(k_p) - g_r n_r$, which opens a gap in the dispersion. We rewrite the dispersion in the laboratory frame in a form that allows to easily identify the effect of the gap on the spectrum,

$$\begin{aligned} \omega_B^\pm(\delta k) &= v_0(x)\delta k(x) - i\frac{\gamma}{2} \pm \left[\left(\frac{\hbar\delta k(x)^2}{2m_{LP}} \right)^2 + \frac{\hbar\delta k(x)^2}{m_{LP}}(2gn_0 - \delta(k_p) + g_r n_r) \right. \\ &\quad \left. + (gn_0 - \delta(k_p) + g_r n_r)(3gn_0 - \delta(k_p) + g_r n_r) \right]^{-1/2} \\ &= v_0(x)\delta k(x) - i\frac{\gamma}{2} \pm \sqrt{\left(\frac{\hbar\delta k(x)^2}{2m_{LP}} \right)^2 + c_B^2 \delta k(x)^2 + m_{\det}^2 c_B^4} \end{aligned} \quad (2.14)$$

where we defined :

$$c_B = \sqrt{\frac{\hbar(2gn_0 - \delta(k_p) + g_r n_r)}{m_{LP}}}, \quad (2.15a)$$

$$m_{\det} = m_{LP} \frac{\sqrt{(gn_0 - \delta(k_p) + g_r n_r)(3gn_0 - \delta(k_p) + g_r n_r)}}{(2gn_0 - \delta(k_p) + g_r n_r)}. \quad (2.15b)$$

These two quantities have a well defined physical meaning as follows. On the one hand, $m_{\det} c_B^2$ is the energy of $k = 0$ modes of ϕ , introducing a mass gap which vanish when the

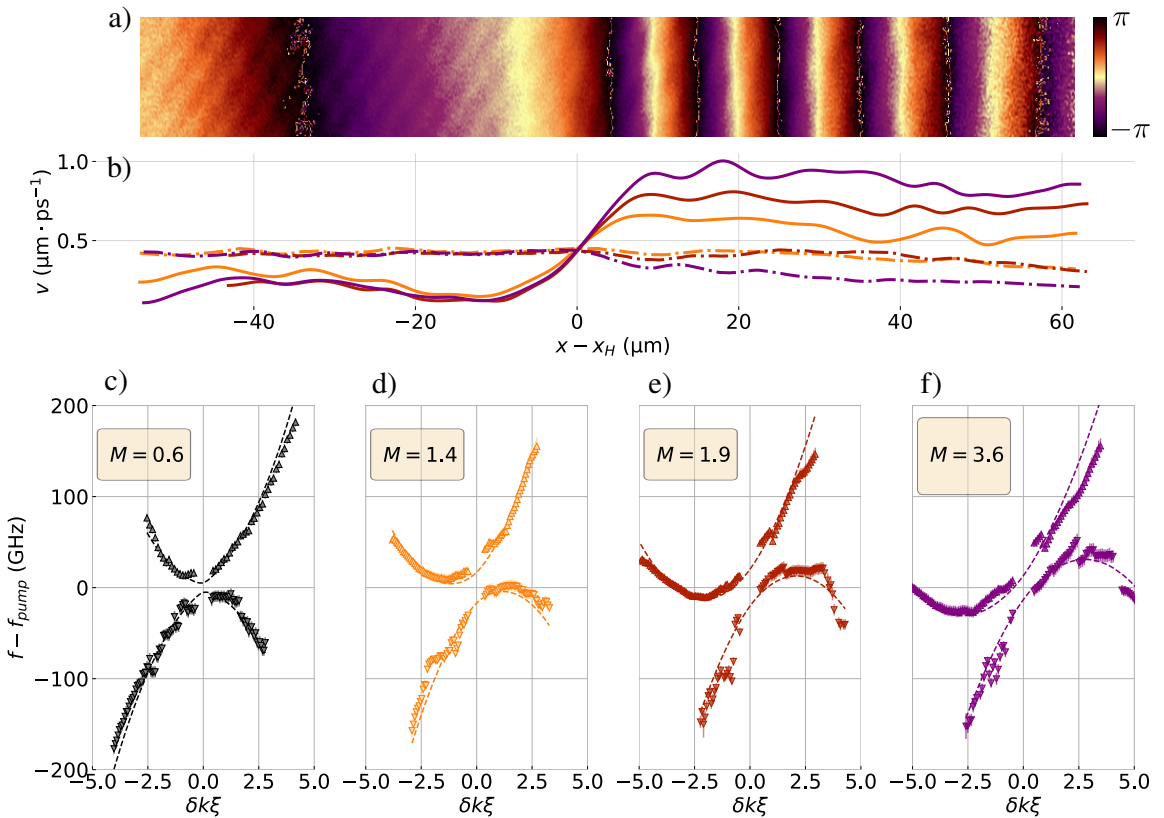


Fig. 2.8 **Smooth horizon.** a) Typical measured phase of the fluid $\theta(x)$ inside the region of interest as defined in Figure 2.3. b) Fluid velocity profiles. Solid lines, $v_0(x)$; dot-dashed lines, $c_s(x)$. Orange, $M_u = 0.6$ and $M_d = 1.4$; red, $M_u = 0.4$ and $M_d = 1.9$; purple $M_u = 0.5$ and $M_d = 3.6$. **Excitation spectra** Eq. (2.12): c) typical upstream region; d)-f) downstream region. Up-triangles, positive-norm branch ω_B^+ ; down-triangles, negative-norm branch ω_B^- ; dashed lines, fit with free parameter gn . Error bars mostly come from the uncertainty in the determination of the center of the lorentzian function used to fit each scan.

system operates at the turning point of the bistability. On the other hand, ?? is a hyperbolic PDE whose characteristic curves in a fluid at rest are given by $|\mathbf{x}| = c_B t$. These characteristics limit the speed at excitations ϕ can propagate information, defining the soundcones in full analogy to light cones. However, due to the mass gap, the speed of propagation of excitations of ϕ is $v_g = d\omega/dk \leq c_B$. The latter can be seen as the limiting speed of propagation of $k \rightarrow \infty$ perturbations. This is also in full analogy to propagation of modes of a massive relativistic scalar field, which travel at subluminal speeds, reaching only the speed of light in the limit of infinite momentum. From [Equation 2.14](#) we see that the field mass m_{det} increases $|\text{Re}(\omega'_B^{\pm})|$ at all k , meaning that the critical velocity to have a Doppler effect large enough to excite negative energy waves is larger than c_s . The value of the critical velocity $v_c = \hbar k_c/m_{LP}$ at which negative energy waves become available at positive frequency can be computed as follows.

For $k_p > k_c$, there will be negative norm modes available at positive frequencies, and there will be two values $\delta k_{1,2}$ at which each dispersion branch intersects the horizontal axes. These $\delta k_{1,2}$ depend on the value of k_p, gn and $g_r n_r$. The critical wavenumber k_c , and correspondingly the critical velocity $v_c = \hbar k_c/m_{LP}$, is obtained when the two intersection points merge, so that $\delta k_1 = \delta k_2 = \delta k_0$. In practice, we compute numerically the normal branch $\omega_B^+(\delta k)$ spectrum for different values of k_p and gn while keeping the zero momentum detuning constant and equal to $\delta(0) = 56$ GHz as in the experiment. On each computed spectrum, we verify if it exhibits negative frequency values. We obtain the map [Figure 2.9](#), if a fluid with given velocity and interaction energy is super-critical. The points c), d), e) and f) correspond to the measured spectrum of [Figure 2.8](#). As it can be seen, the upstream region and downstream region with the smaller velocity don't lie in the super-critical regime whereas e) and f) do. This is in agreement with the fact that the critical velocity is larger than the speed of sound since all the regime yielding super-critical flows are located on the right side of the black dashed line corresponding to the acoustic case $c_s = \hbar k_p/m_{LP} = \sqrt{\hbar gn/m_{LP}}$. Besides, the map predicts well that configuration d) is subcritical despite a Mach number $M_d = 1.34$ greater than one.

Cutoff spatial frequency. The absence of experimental data points at wavevectors $\delta k < 0.10 \mu\text{m}^{-1}$ is a consequence of the finite size of the probe beam $\delta_x = 60 \mu\text{m}$ which fixes the spatial extension of the probe in momentum space scaling as $2\pi/\delta_x = 0.10 \mu\text{m}^{-1}$. At very small wavevector, the probe and its conjugated counterpart start to overlap and photons coming from both branches are collected by the pinhole. This prevent the effective discrimination between the two modes in the output signal of the photodiode. In practice the cutoff frequency is computed by a simple optical Rayleigh criterion stating that two points are resolved if the distance between them is larger than the FWHM of the point spread function. In our case this directly gives $\delta k_{cut} = 2\pi/\delta_x = 0.10 \mu\text{m}^{-1}$.

2.4.2.3 Paired emission frequency range

The paired emission of correlated mode at the horizon require the mixing of positive and negative energy modes. Consequently the finite velocity in the downstream sets a maximum frequency at which the effect can occur [?]. This frequency is given by the maximum energy of the negative energy modes that can be excited in the downstream region and is ultimately set by the asymptotic downstream velocity v_d and the interaction energy gn . Increasing this

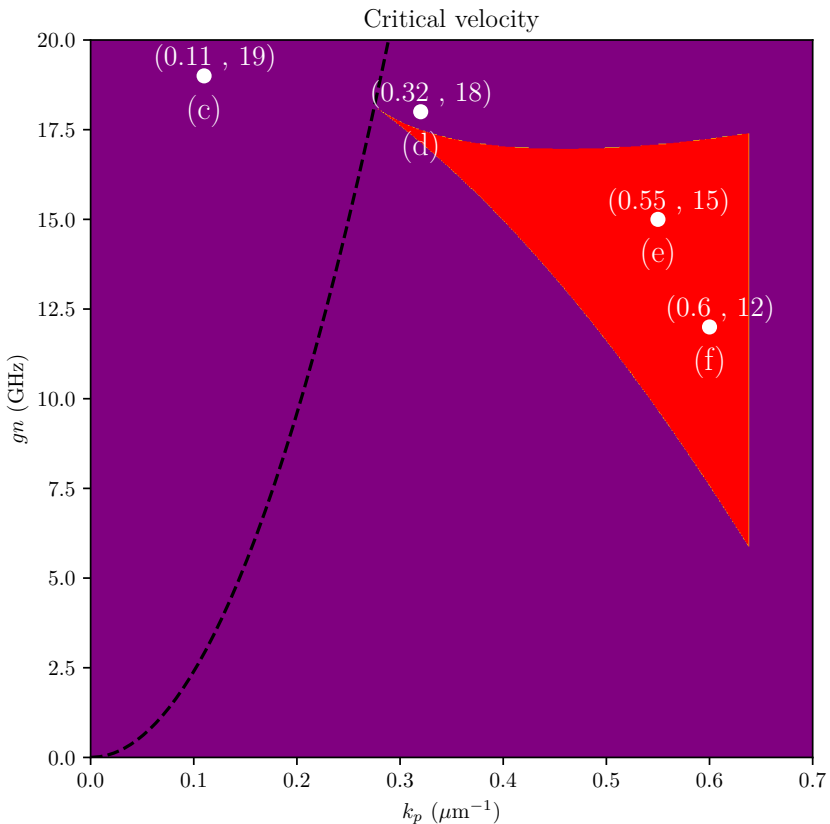


Fig. 2.9 Critical velocity map as a function of k_p and gn while the reservoir contribution was fixed as $g_r n_r \approx 1.8 = gn$. For each couple (k_p, gn) the bogoliubov spectrum [Equation 2.12](#) is computed : red points correspond to super critical flows and purple point to sub-critical flows. The points c), d), e) and f) correspond to the measured spectrum of [Figure 2.8](#). The black dashed line represent the acoustic case where the critical velocity coincide with the speed of sound $c_s = \hbar k_s / m_{LP} = \sqrt{\hbar gn / m_{LP}}$

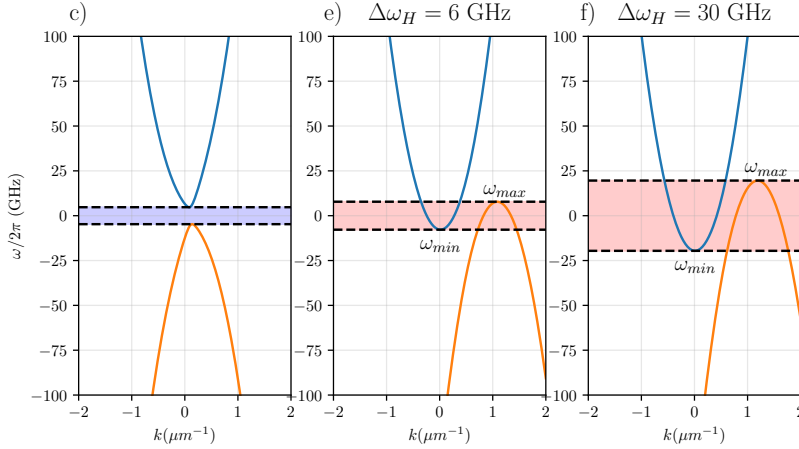


Fig. 2.10 c) , e) , f) analytical bogoliubov dispersion corresponding to the fit of Figure 2.8 c), e) and f). The red range in e) and f) represent the frequency range at which negative energy modes are available that can mix with the positive energy modes outside the gap represented in blue whose value $\Delta\omega_H$ are displayed above each plot.

range result in a larger number of correlated pairs emitted and is expected to enhance the overall correlation signal [?]. In Figure 2.10 we plot the analytical bogoliubov dispersion corresponding to the measurement of Figure 2.8 c), e) and f). Paired emission is then possible in the red range of Figure 2.10 where negative energy modes can mix with the positive energy mode of the upstream spectrum, located outside the gap represented in blue.

The overall frequency range at which hawking emission is possible is given by :

$$\Delta\omega_H := 2\omega_{max} - \Delta\omega_{gap} \quad (2.16)$$

where ω_{max} is the maximum energy of the negative energy modes that can be excited in the downstream region and $\Delta\omega_{gap}$ the width of the gap in the upstream spectrum. We measure $\Delta\omega_H=6$ GHz for the e) configuration and 30 GHz for the fastest flow. Hence by changing the asymptotic downstream speed our system enable to tune the number of states available for paired emission. Let us now see that we can control another crucial parameter of the hawking radiation, the steepness of the horizon.

2.4.3 Steep horizon geometry

The sharpness of the transition is a crucial parameter to study the strength of correlation of the emitted modes. It can be inferred by the quantity :

$$\kappa := \frac{1}{2c_s(x)} \frac{d}{dx} [v_0^2(x) - c_s^2(x)]|_{x_H}, \quad (2.17)$$

the hydrodynamic equivalent to surface gravity [1]. However the discussion in the previous section pointed out that the position x_H at which the fluid velocity exceed the speed of sound doesn't define the horizon of the fluid, the derivative in the definition of κ should then rather

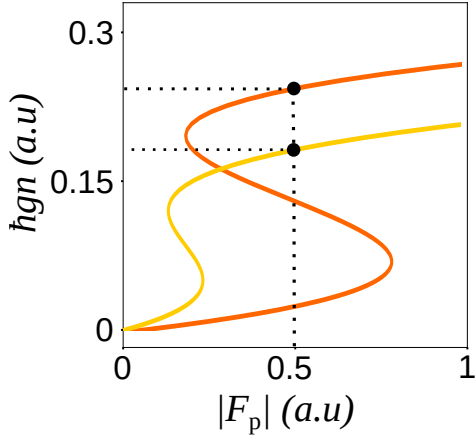


Fig. 2.11 *Bistability cycle for two different values of the effective detuning $\delta(k_p^{(1)})$ (yellow) $\leq \delta(k_p^{(2)})$ (orange) when $k_p^{(2)} \leq k_p^{(1)}$. The vertical dashed line represent the input intensity of the pump laser whereas the black dots represent the operating points of the system for each detuning. The region with the higher wavevector yields a lower gn value.*

be taken at the position where the critical velocity is reached and involve the critical velocity instead of c_s . In practice this brings only a negligible correction to the value of κ .

Increasing the surface gravity. The steepness of the horizon can be tuned in two ways. First, by reducing the width of the transition w_H in the target velocity profile. Second, by taking advantage of the dependence of the bistability cycle on the effective detuning $\delta(k_p)$. As shown in Figure 1.12 b) the value of gn with a fixed input intensity scales increases linearly with the effective detuning until the turning point is reached. More precisely, when the pump wavevector is increased, $\delta(k_p) = \omega_p - \omega_{LP}^{(0)} - \hbar k_p^2 / 2m_{LP}$ decreases and so does gn as shown in Figure 2.11. In some sense the microcavity naturally reduces the density of the fluid when the pump wavevector is increased, moving the laser away from resonance. In practice, we tune wisely the energy of the pump laser and the asymptotic upstream and downstream target wavevectors. The different values of $\delta(k_{up})$ and $\delta(k_d)$ can lead to regions with different gn values as shown on Figure 2.11. Here we create a trans critical flow with a sharper transition in order to increase the value

Here we exploit the phenomenology and implement the target profile Equation 2.3 with a large difference between v_d and v_u , a transition width $w_H = 20 \mu\text{m}$ and a detuning $\delta(0) = 71 \text{ GHz} \rightarrow \hbar\delta(0) = 0.3 \text{ meV}$ Figure 2.12 (b) shows $v_0(x)$ (solid lines) as well as $c_s(x)$ (dot-dashed lines). The two supercritical fluids created in the smooth configuration have an horizon steepness κ of 0.07 ps^{-1} (red) and 0.08 ps^{-1} (purple) whereas in the steep geometry implemented here we compute $\kappa = 0.11 \text{ ps}^{-1}$. The excitation spectra are shown in Figure 2.12 c) and d). The frequency range at which paired emission is possible is roughly the same than in the smooth case f) $\Delta\omega_H = 28 \text{ GHz}$ whereas the horizon steepness gets increased by 25%. This independent tuning of κ and the paired emission spectrum is not possible in conservative quantum fluids such as atomic BECs, for example. The fine control over the waterfall horizon geometry we demonstrate here is interesting to test recent tunneling models for the Hawking effect [32].

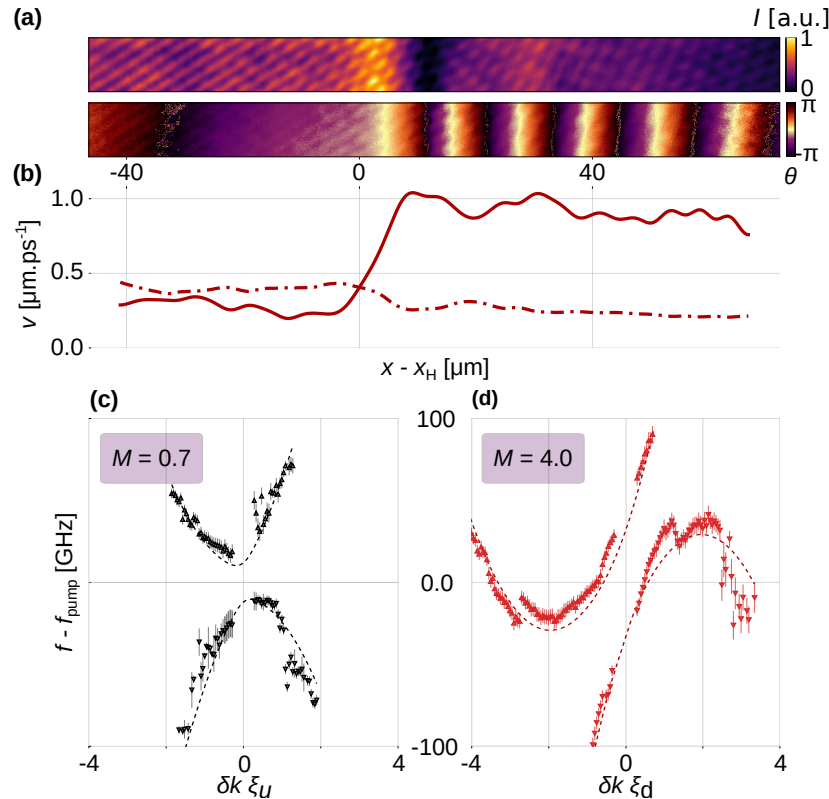


Fig. 2.12 **Steep horizon.** (a) Measured fluid density (top) and phase (bottom). (b) Measured fluid velocity profile. Solid line, $v_0(x)$; dashed line, $c_s(x)$. **Excitation spectra** Eq. (2.12): (c) upstream region. (d) downstream region; dashed lines, fit with free parameter gn . Error bars represent the uncertainty in the determination of the center of the lorentzian when each scan is fitted by a lorentzian function to find the resonance energy. The M values in the inset of each spectrum is the computed Mach number in the corresponding region.

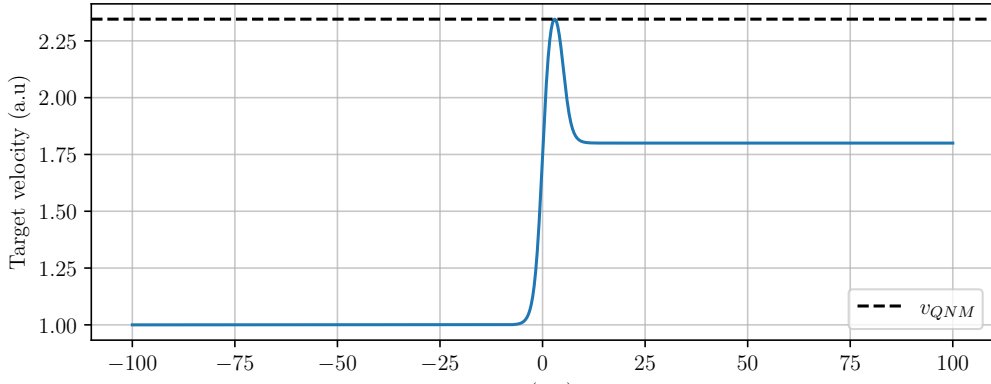
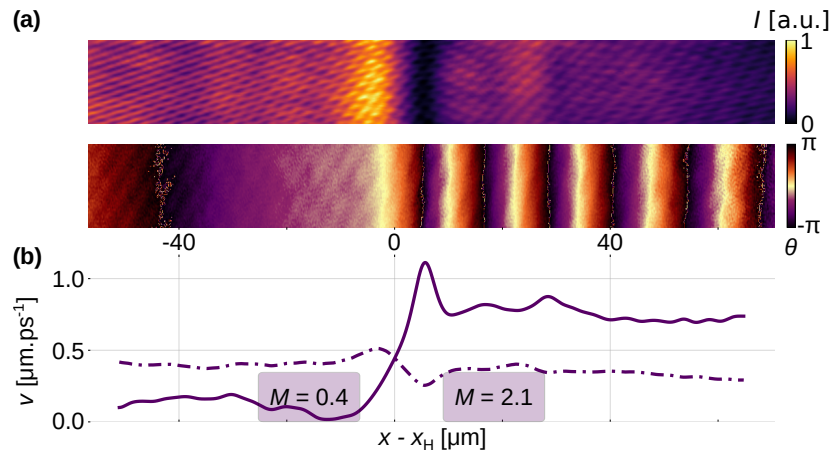


Fig. 2.13 Typical QNM target velocity profile.

Fig. 2.14 Quasi-normal mode horizon. (a) Measured fluid density (top) and phase (bottom). (b) Measured fluid velocity profile. Solid line, $v_0(x)$; dashed line, $c_s(x)$.

2.4.4 Quasi-normal mode configuration

The target velocity profile Equation 2.3 can be complexified to create complex horizon geometry by imprinting a velocity peak in the transition region. More precisely, we define the *Quasi-Normal Mode* (QNM) target velocity profile as :

$$v(x) = \frac{v_{QNM} - v_{up}}{2} \tanh\left(\frac{x - x_1}{w_1}\right) + \frac{v_d - v_{QNM}}{2} \tanh\left(\frac{x - x_2}{w_2}\right) + \frac{v_{up} + v_d}{2} \quad (2.18)$$

where v_{QNM} is the velocity of the peak, v_{up} and v_d are the upstream and downstream velocities, x_1 and x_2 are the position of the first and second transition and w_1 and w_2 are their width. The typical corresponding shape is shown in Figure 2.13. With the same asymptotic parameters as in the smooth horizon configuration of Figure 2.8 e) we create a fluid with the QNM target velocity profile.

First, the asymptotic velocities are as expected, not modified by the presence of the peak, while the surface gravity is greatly enhanced as $\kappa = 0.19 \text{ ps}^{-1}$, almost twice the value

obtained in the steep configuration. But the most peculiar feature of the QNM configuration is the density dip that comes with the velocity peak. For the reason explained in the previous section, the velocity peak imprinted here is associated with a density dip. As the dip is surrounded by two regions of higher density, it forms an effective resonator for bogoliubov excitation. This leads to the appearance of a metastable excitation mode of ϕ called a quasi-normal mode: here specifically, a negative-energy standing wave can establish itself inside the resonator (at $\omega_{\text{QNM}} > \max(\omega_B^-|_{x>x_H})$) and tunnel-couple with positive-energy propagating waves on either side [16]. This quasi-normal mode is spontaneously excited by quantum vacuum fluctuations of ϕ . As a result, the Hawking spectrum is predicted to peak at the frequency of the quasi-normal mode, bearing signatures of the near-horizon geometry. In some sense, the QNM configuration is a quantum analogue of the black hole ringdown phase, where the black hole emits gravitational waves with a characteristic frequency and damping time [?] that depend on its parameters.

2.5 Conclusion

We demonstrated full optical generation and characterization of mean field with arbitrary velocity profiles in a polariton fluid which act as effectively curved spacetime for bogoliubov excitation. In each configuration, we were able to measure the collective excitation spectrum of the fluid and state or not if Hawking radiation could be observed. We showed that the critical velocity to observe negative energy modes is not necessarily the speed of sound but rather a critical velocity that depends on the fluid parameters. This widens the range of experimental configurations at which particle creation can be observed. The great versatility of our experimental methods also showed that the steepness of the horizon can be controlled independently of the paired emission spectrum. Finally, we demonstrated the possibility to create complex horizon geometry that could yield peculiar behaviors like Quasi Normal Modes. The great advantage of the system presented here is the great range of field theory scenario that can be tested in a single setup. Eventhough trans-critical polariton fluids are far from encapsulating what truly happen at a black hole horizon, its a great platform to study effect predicted by field theory in curved spacetime, regardless they were originally thought for black holes or not.

2.5.1 Outlook

Appendices

Appendix A

Mean field shaping and monitoring

A.1 Phase printing

Controlling precisely the phase of a laser beam is a common but challenging task in optics. The most basic way to do it is by applying spatial filtering in the fourier plane of a lens. The phase of the beam after a second collimating lens is then given by the convolution product of the beam phase and the mask inverse fourier transform. This method then show its limits when one wants to generate complex phase profile since its depend on the mask form. A way to overcome this problem is the use of Digital Micromirror Device (DMD) which is an array of micro-mirrors that can be individually controlled to reflect the light or not. By putting this array in the fourier plan of a lens it is possible to create spatial filtering with arbitrary shapes. However, this method suffers from high losses and diffraction of the light on the individual mirrors that tend to add unwanted noise. This being said, DMD are very powerfull devices and allow to do a great amount of things at low cost. A wide range of possible methods are referenced in the great work [31].

A.1.1 Spatial light modulator.

In this work, we use a Spatial Light Modulator (SLM) which is a liquid crystal display that can be used to modulate the phase of a laser beam. The principle is to apply a voltage on each pixel of the SLM to change the orientation of the liquid crystal molecules. The phase shift is then given by the difference of the optical path of light going through the different pixels as shown in [Figure A.1](#).

By shinning a flat phase collimated beam on the SLM which displays the target phase profile the beam gets reflected carrying the desired wavefront. However the efficiency of the SLM is not perfect and whenever light is shone on it, some photons might not see it and not be phase modulated. To overcome this difficulty, we first write a blazed phase grating on the SLM screen on top of which the wanted profile is set. All the photons that did interact with the liquid crystals are then mostly diffracted on the first order of the grating. Doing so, an efficiency of 60-70% can be reached. This contrast with the usual 80% usually claimed on manufacturer datasheets that actually correspond to the efficiency in all orders. A typical phase profile encoded on the SLM is shown in [Figure A.2](#). A gray value of zero correspond to no shift while 255 corresponds to 2π . The gray map corresponding to the target phase

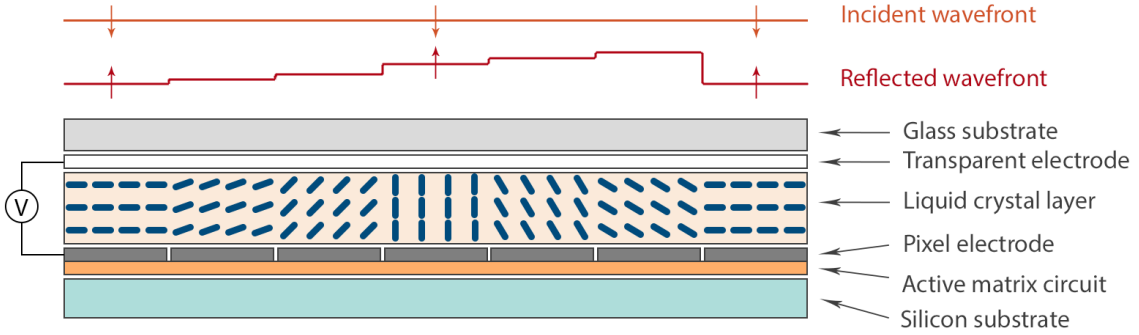


Fig. A.1 *Principle of a Spatial Light Modulator.*

profile has been unwrapped for the sake of clarity and is shown in [Figure A.2 c](#)). The final gray map displayed on the SLM screen is represented in [Figure A.2 e](#)).

To imprint precisely the resulting wavefront in the cavity plane two $2f - 2f$ optical telescopes are used in series to image the SLM screen with an overall demagnification of 1/130 while avoiding short focal length that would introduce optical aberrations. An adjustable slit is placed in the fourier plane of the first telescope to filter out the unwanted diffracted orders.

A.1.2 Phase measurement

A.1.3 Off axis interferometry

The principle is the following : the beam whose phase is to be measured is recombined on a CCD camera with a flat phase reference beam. An angle is voluntary introduced between the two beam to create an interference pattern on the camera plane. The phase difference between the two beams is then encoded in the size of the fringes and can be recovered by performing a fourier transform on the interferogram and demodulate the signal around the satellite peak created by the angle between the two beams [22].

A.1.4 Controlling the local intensity

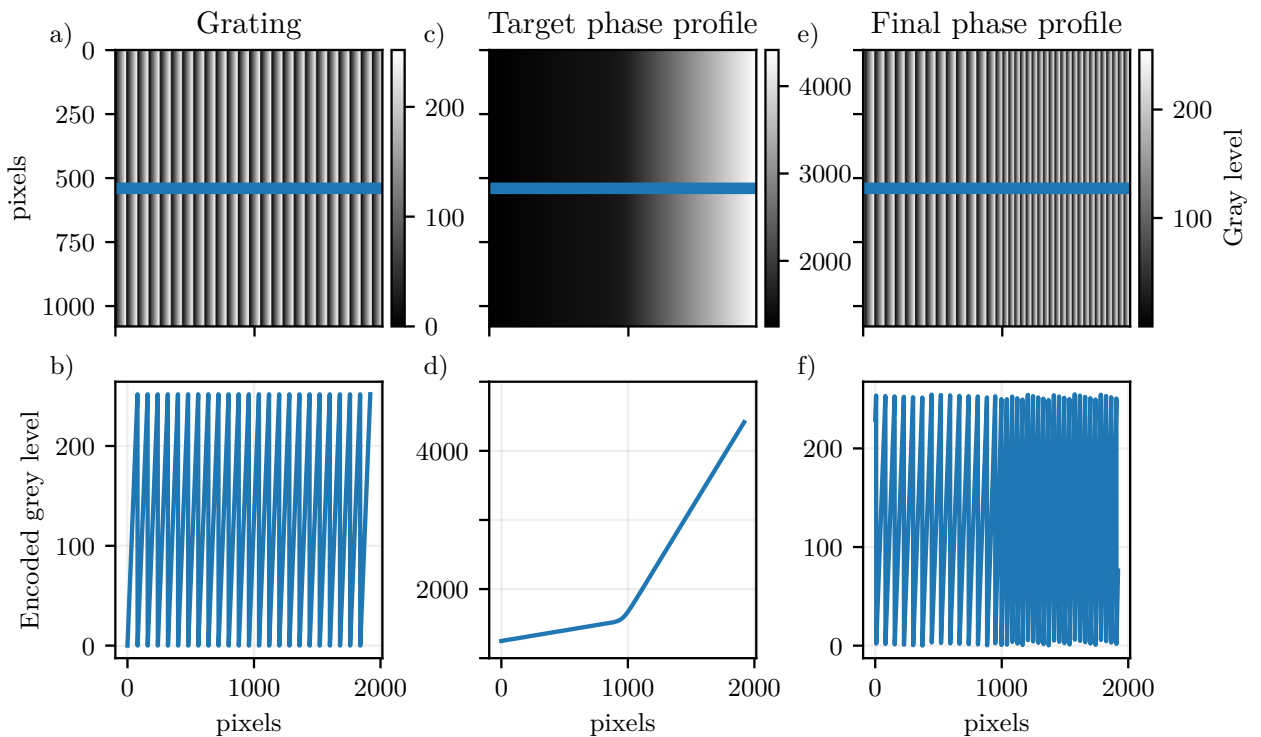


Fig. A.2 *Typical profile encoded on the SLM to generate the target velocity profile. a) Gray map of a phase blazed grating encoded on the SLM screen and b) corresponding cut in the x direction. c) Unwrapped grey map of the target phase profile and d) corresponding cut in the x direction. e) Final gray map encoded on the SLM screen and f) corresponding cut in the x direction. This map is the sum of the blazed grating and the target phase profile modulus 255.*

Bibliography

- [1] Carlos BARCELÓ, Stefano LIBERATI, Sebastiano SONEGO & Matt VISSER. “Hawking-like radiation does not require a trapped region”. *Physical Review Letters* **97**(17). Cited page 61
- [2] Iacopo CARUSOTTO & Cristiano CIUTI 2013. “Quantum fluids of light”. *Rev. Mod. Phys.* **85**(1), p. 299–366. Cited page 34
- [3] C. CIUTI, V. SAVONA, C. PIERMAROCCHI, A. QUATTROPANI & P. SCHWENDIMANN 1998. “Role of the exchange of carriers in elastic exciton-exciton scattering in quantum wells”. *Phys. Rev. B* **58**, p. 7926–7933. Cited page 22
- [4] F. CLAUDE, M. J. JACQUET, R. USCIATI, I. CARUSOTTO, E. GIACOBINO, A. BRAMATI & Q. GLORIEUX 2022. “High-Resolution Coherent Probe Spectroscopy of a Polariton Quantum Fluid”. *Physical Review Letters* **129**(10), p. 103 601. Publisher: American Physical Society. Cited pages 28, 48, and 56
- [5] Ferdinand CLAUDE 2022. *High resolution coherent spectroscopy of a polariton fluid : Bogoliubov modes, non equilibrium phase transitions and turbulence*. Theses Sorbonne Université. URL <https://theses.hal.science/tel-04009505>. Cited pages 27, 49, 53, and 56
- [6] C. COHEN-TANNOUDJI, B. DIU & F. LALOE 2018. *Mécanique Quantique - Tome 2: Nouvelle édition* (EDP sciences). ISBN 978-2-7598-2285-0. URL <https://books.google.fr/books?id=9KxxDwAAQBAJ>. Cited page 21
- [7] Claude COHEN-TANNOUDJI, Jacques DUPONT-ROC & Gilbert GRYNBERG. *Photons and atoms: introduction to quantum electrodynamics*. Physics textbook. Nachdr. édition. ISBN 978-0-471-18433-1. Cited page 26
- [8] M. COMBESCOT, M. A. DUPERTUIS & O. BETBEDER-MATIBET 2007. “Polariton-polariton scattering: Exact results through a novel approach”. *Europhysics Letters* **79**(1), p. 17 001. Cited pages 22 and 30
- [9] Monique COMBESCOT & Shiau SHIUE-YUAN. *Excitons and Cooper Pairs Two Composite Bosons in Many-Body Physics*. 1st ed édition. ISBN 9780191815287. Cited pages 8, 10, 12, and 13
- [10] DE BROGLIE, LOUIS 1925. “Recherches sur la théorie des quanta”. *Ann. Phys.* **10**(3), p. 22–128. Cited page 32
- [11] Irénée FRÉROT, Amit VASHISHT, Martina MORASSI, Aristide LEMAÎTRE, Sylvain RAVETS, Jacqueline BLOCH, Anna MINGUZZI & Maxime RICHARD 2023. “Bogoliubov excitations driven by thermal lattice phonons in a quantum fluid of light”. *Phys. Rev. X* **13**, p. 041 058. Cited pages 22 and 53

- [12] E P GROSS 1961. “Structure of a quantized vortex in boson systems”. *Nuovo Cimento (Italy) Divided into Nuovo Cimento A and Nuovo Cimento B* **10**(10). Cited page 33
- [13] Gilbert GRYNBERG, Alain ASPECT & Claude FABRE. *Introduction to Quantum Optics*. Cited page 37
- [14] S. W. HAWKING. “Black holes in general relativity”. *Communications in Mathematical Physics* **25**(2), p. 152–166. Cited page 43
- [15] J. J. HOPFIELD. “Theory of the contribution of excitons to the complex dielectric constant of crystals”. *Physical Review* **112**(5), p. 1555–1567. Cited page 25
- [16] M.J. JACQUET, L. GIACOMELLI, Q. VALNAIS, M. JOLY, F. CLAUDE, E. GIACOBINO, Q. GLORIEUX, I. CARUSOTTO & A. BRAMATI 2023. “Quantum Vacuum Excitation of a Quasinormal Mode in an Analog Model of Black Hole Spacetime”. *Physical Review Letters* **130**, p. 111 501. Cited page 65
- [17] JOFFRE, M., HULIN, D., MIGUS, A., MYSYROWICZ, A. & ANTONETTI, A. 1987. “Subpicosecond excitonic optical nonlinearities in quantum wells”. *Rev. Phys. Appl. (Paris)* **22**(12), p. 1705–1709. Cited page 22
- [18] J. KASPRZAK, M. RICHARD, S. KUNDERMANN, A. BAAS, P. JEAMBRUN, J. M. J. KEELING, F. M. MARCHELLI, M. H. SZYMAŃSKA, R. ANDRÉ, J. L. STAELHIL *et al.* “Bose–einstein condensation of exciton polaritons”. *Nature* **443**(7110), p. 409–414. Cited pages 35 and 36
- [19] Charles KITTEL. *Introduction to solid state physics*. 8th ed édition. ISBN 978-0-471-41526-8. Cited pages 8 and 17
- [20] A. Von LEHMEN, D. S. CHEMLA, J. E. ZUCKER & J. P. HERITAGE 1986. “Optical stark effect on excitons in gaas quantum wells”. *Opt. Lett.* **11**(10), p. 609–611. Cited page 22
- [21] Zejian LI, Ferdinand CLAUDE, Thomas BOUILIER, Elisabeth GIACOBINO, Quentin GLORIEUX, Alberto BRAMATI & Cristiano CIUTI 2022. “Dissipative phase transition with driving-controlled spatial dimension and diffusive boundary conditions”. *Phys. Rev. Lett.* **128**, p. 093 601. Cited page 39
- [22] Michael LIEBLING, Thierry BLU & Michael UNSER. “Complex-wave retrieval from a single off-axis hologram”. *J. Opt. Soc. Am. A* **21**(3), p. 367. Cited page 70
- [23] T. C. H. LIEW, A. V. KAVOKIN & I. A. SHELYKH 2008. “Optical circuits based on polariton neurons in semiconductor microcavities”. *Phys. Rev. Lett.* **101**, p. 016 402. Cited page 29
- [24] Anne MAITRE. *Generation, propagation and control of quantized vortices and dark solitons in polariton superfluids*. Thèse de doctorat. URL <https://theses.hal.science/tel-03147158>. Cited pages 23 and 29
- [25] Jean-Michel MÉNARD, C. POELLMANN, Michael PORER, U. LEIERSEDER, Élisabeth GALOPIN, Aristide LEMAÎTRE, Alberto AMO, Jacqueline BLOCH & Rupert HUBER 2014. “Revealing the dark side of a bright exciton–polariton condensate”. *Nature Communications* **5**. Cited page 34
- [26] N. MIELEC, M. ALTORIO, R. SAPAM, D. HORVILLE, D. HOLLEVILLE, L. A. SIDORENKOV, A. LANDRAGIN & R. GEIGER 2018. “Atom interferometry with top-hat laser beams”. *Applied Physics Letters* **113**(16), p. 161 108. Cited page 46

- [27] A. MYSYROWICZ, D. HULIN, A. ANTONETTI, A. MIGUS, W. T. MASSELINK & H. MORKOÇ 1986. “"dressed excitons" in a multiple-quantum-well structure: Evidence for an optical stark effect with femtosecond response time”. *Phys. Rev. Lett.* **56**, p. 2748–2751. Cited page 22
- [28] H.S. NGUYEN, D. GERACE, I. CARUSOTTO, D. SANVITTO, E. GALOPIN, A. LEMAÎTRE, I. SAGNES, J. BLOCH & A. AMO. “Acoustic black hole in a stationary hydrodynamic flow of microcavity polaritons”. *Phys. Rev. Lett.* **114**(3), p. 036402. Cited pages 44 and 48
- [29] Lev P PITAEVSKII 1961. “Vortex lines in an imperfect bose gas”. *Sov. Phys. JETP* **13**(2), p. 451–454. Cited page 33
- [30] Lev P. PITAEVSKIJ & Sandro STRINGARI 2016. *Bose-Einstein condensation and superfluidity*. Numéro 164 dans International series of monographs on physics. Reprinted (with corrections) édition. ISBN 978-0-19-875888-4. Cited page 32
- [31] S. POPOFF. “Wavefront shaping”. <https://www.wavefrontshaping.net/>. Cited page 69
- [32] Francesco Del PORRO, Stefano LIBERATI & Marc SCHNEIDER 2024. “Tunneling method for hawking quanta in analogue gravity”. *arXiv:2406.14603*. Cited page 62
- [33] G. ROCHAT, C. CIUTI, V. SAVONA, C. PIERMAROCCHI, A. QUATTROPANI & P. SCHWENDIMANN 2000. “Excitonic bloch equations for a two-dimensional system of interacting excitons”. *Phys. Rev. B* **61**, p. 13856–13862. Cited page 22
- [34] Elena ROZAS, Evgeny SEDOV, Yannik BRUNE, Sven HÖFLING, Alexey KAVOKIN & Marc ASSMANN 2023. “Polariton–dark exciton interactions in bistable semiconductor microcavities”. *Phys. Rev. B* **108**, p. 165411. Cited page 38
- [35] Mark STEGER, Gangqiang LIU, Bryan NELSEN, Chitra GAUTHAM, David W. SNOKE, Ryan BALILI, Loren PFEIFFER & Ken WEST 2013. “Long-range ballistic motion and coherent flow of long-lifetime polaritons”. *Phys. Rev. B* **88**, p. 235314. Cited page 48
- [36] Petr STEPANOV, Ivan AMELIO, Jean-Guy ROUSSET, Jacqueline BLOCH, Aristide LEMAÎTRE, Alberto AMO, Anna MINGUZZI, Iacopo CARUSOTTO & Maxime RICHARD. “Dispersion relation of the collective excitations in a resonantly driven polariton fluid”. *Nat Commun* **10**(1), p. 1–8. Cited page 34
- [37] Tunemaru USUI 1960. “Excitations in a high density electron gas. i:”. *Progress of Theoretical Physics* **23**(5), p. 787–798. Cited page 30
- [38] S. UTSUNOMIYA, L. TIAN, G. ROUMPOS, C. W. LAI, N. KUMADA, T. FUJISAWA, M. KUWATA-GONOKAMI, A. LÖFFLER, S. HÖFLING, A. FORCHEL *et al.* “Observation of bogoliubov excitations in exciton-polariton condensates”. *Nature Physics* **4**(9), p. 700–705. Cited page 28
- [39] C. WEISBUCH & J. RARITY 1996. *Microcavities and Photonic Bandgaps: Physics and Applications*. ISBN 978-94-009-0313-5. URL <https://link.springer.com/book/10.1007/978-94-009-0313-5>. Cited page 20

Sujet : Contrôle tout optique de fluides quantiques de lumière en vapeur atomique chaude

Résumé : To do

Mots clés : Optique quantique, fluides quantiques de lumière, superfluidité, Falque, contrôle tout optique, Gravité Analogue, Rayonnement de Hawking, Création de particules, Theorie des champs, Espace-temps courbe, Trous noirs

Subject : Full optical control of quantum fluids of light in hot atomic vapors

Abstract: To do

Keywords : Quantum optics, quantum fluids of light, quantum fluids, superfluidity, Falque full optical control, Analogue Gravity, Hawking Radiation , Particles Creation, Quantum field theory, Curved spacetime, Black Holes
